Kinematic Structure and Ionization of Optical Jets Associated with Young Stellar Objects

Takayuki Nishikawa

Doctor of Science

Department of Astronomical Science
School of Physical Science
The Graduate University for Advanced Studies

2006

Acknowlegements

I would like to thank my supervisor Prof. Hayashi who gave me invaluable opportunity to study at the Subaru Telescope and encourage me to follow my research. I am very grateful to Dr Takami for the boundless enthusiasm as well as patiently taking the much time to guide me. He kindly gave me a hand whenever I had some problems. Without his help, I would never have been complete this work. I am grateful to Dr. Pyo for teaching me the data reduction, and also Dr. Tajitsu for useful comments about instrument. I had unforgettable time in Hawaii during the three years. I would like to thank the staff and graduate students at the Subaru Telescope.

I would like to thank late Prof. Uchida who led me to frabjous field of astronomy. The data presented in this thesis was obtained by his observational time. So I am glad to be able to compile this dissertation.

Finally, I would like to express my deepest gratitude for my parents who support me and encourage through my life.

Abstract

Optical jets and molecular bipolar outflows are two major manifestations of outflowing activities associated with young stellar objects (YSOs). It is not clear how these two outflow activities are related with each other. One of the major scenarios is that a collimated jet seen in the optical-IR wavelength entrains its ambient molecular material, allowing the molecular outflow to occur. In order for us to tackle this issue, it is crucial to understand how jets interact with ambient material.

In addition to the kinematics, the mass loss rate and mass momentum transfer rate of a jet are key parameters to investigate how the jet interacts with the ambient material. However, the mass momentum is poorly known because the hydrogen density is not easily derived, as is different from the electron density that is measured from forbidden line emissions. If we assume that a jet is fully ionized, i.e. the electron density is nearly equal to the hydrogen density, the mass momentum of the jet derived from its optical emission lines is not sufficient to drive the molecular outflow associated with it. In contrast, recent studies have suggested that jets are almost neutral, indicating that a jet may have momentum sufficient to drive a molecular outflow.

In order to study the issues described above, we made slit-scan observations of Hα and [NII] 6583 Å emission lines toward two bright jets, HH 46/47 and the HL Tau jet, with Subaru Telescope. The large diameter of the telescope, together with the high spectral resolution of the spectrograph (High Dispersion Spectrograph, R = 3.6×10^4 or Δv = 8 km s^{-1}) allowed us to study the kinematics of these jets in unprecedented detail. Furthermore, the slit-scan technique with a long slit provided us with kinematic information of the entire jets.

We found that, in both jets, the Hα emission traces both the main jet component ($V_{\rm LSR} = -160 \sim -180$ km s^{-1}) and distinct lower velocity component ($|V_{\rm LSR}| \leq 120$ km s^{-1}). The [NII] emission, on the other hand, is primarily associated with the main jet component and is much faint or absent in the lower velocity component. In the HH 46/47 jet, the velocities of Hα and [NII] emission lines match well in their main jet components. The lower velocity components are associated with one-sided bow shocks and with one of the Hα filaments that was previously identified with the *Hubble Space Telescope*. In the HL Tau jet, the lower velocity component is associated with individual knots, which is explained by the lower velocity emission arising in the laterals of bow shocks. While the main jet component

is associated with the ejecta, the lower velocity component is produced as a result of the interaction between the ejecta and the surrounding gas.

Observed Hα line profiles suggest that the shock velocities at the bow shocks and the Hα filament with respect to the ambient gas are 60–80 km s^{-1} and 120–130 km s^{-1} for HH 46/47 and HL Tau, respectively. These are markedly smaller than the three dimensional (3-D) velocities of the jets ($\sim$300 km s^{-1}). The discrepancy between the shock velocity and 3-D velocity is explained if the ambient gas moves outward by $\sim$200 km s^{-1}. The velocity of the ambient gas measured in the HH 46/47 jet is similar to those of HH 47A and 47D, giant bow shocks ahead of the observed region.

Through detailed analysis, we concluded that the outward motion of the ambient gas is a result of prompt entrainment, i.e. a jet sweeps up ambient material at its head by a large bow shock, but not of turbulent entrainment, the other entrainment mechanism proposed to date. Indeed, our high spectral resolution slit-scan observations of Hα show that the main jet component has a uniform radial velocity of $V_{\rm LSR} = -160$ km s^{-1} (Δv = 10 km s^{-1}) and did not show the presence of slow Hα components ($\mid V_{\rm LSR} \mid \leq 120$ km s^{-1}) along the edges of the jets. Such slow Hα emission was reported in previous observations and was proposed to arise from turbulent boundary layers between the main flow and the ambient gas. Our results indicate that Hα and [NII] originate from the main jet component (i.e. the ejecta), and also from bow shocks and Hα filaments, but not from turbulent mixing layers.

We also investigated the ionization fraction in the jets using the [NII]/Hα flux ratio. In the case of HH 46/47, the ratio is 0.2–0.5 in the main jet component and even higher in some other regions. Shock model calculations show that the ratio is sensitive to the ionization fraction of preshock gas if the shock velocity is less than 100 km s^{-1}. The observed high ratio for HH 46/47 is expected if its main jet component is considerably ionized, although previous observations proposed a much lower ionization fraction of $\leq$ 0.2. The [NII]/Hα flux ratio is significantly smaller than 0.2 in the one-sided bow shocks and Hα filaments, indicating that the gas surrounding the ejecta is rather neutral.

For the HL Tau jet, the observed [NII]/Hα flux ratio markedly vary from one region to another: 0.1–0.7 at the base of the jet, less than 0.1 in knot A, $\sim$0.2 in knot B, $\sim$0.4 in knot C, and $\sim$0.7 in knot D. Because the shock velocities of the HL Tau jet exceed 100 km s^{-1} in some regions, the ratio does not directly reflect the ionization fraction of preshock gas. At the knots A–D, the [NII]/Hα flux ratio increases from $<$0.1 to 0.7 with distance from the source. This suggests that the preshock density decreases with distance from the source. The ratio at the lateral of the bow shocks is less than $\sim$0.1, suggesting that the ambient medium is almost neutral. At the base

of the jet, the observed [NII]/Hα flux ratio decreases from 0.7 to 0.1 as the distance from the source increases. This suggests that the ionization fraction decreases with distance as a result of radiative recombination.

We compared the [NII]/Hα ratio in the main jet components of the HH 46/47 jet and HL Tau jet. The ratio for the HH 46/47 jet is higher (0.2–0.5) than that for the HL Tau ($\leq$0.2), indicating high ionization fraction. Such a difference suggests that the radiation from a nearby O star irradiates the ambient gas of the HH 46/47 system, which is located near the HII region Gum nebula, causing the high ionization fraction in the main jet component. Another possible interpretation is that radiative cooling by recombination is not efficient in the HH 46/47 jet because of its low density, thus allowing the high ionization fraction in the jet significantly away from the driving source.

Contents

List of Figures

List of Tables

Chapter 1

Introduction

1.1 OUTFLOWS FROM YOUNG STELLAR OBJECTS

Jets and winds emanating from young stellar objects (YSOs) hold a key to understanding star formation. They are believed to play important roles in removing excess angular momentum from circumstellar disks and promoting mass accretion onto YSOs. Consequently, YSOs can maintain stable conditions without attaining brake-up speed. In addition, jets and winds dissipate gas and dust around YSOs. Studies of mass ejection from YSOs will thus lead us to understand the determination mechanism of stellar mass and also the evolution of accretion disks. Large infrared excess and blueshifted forbidden lines toward YSOs suggested the presence of circumstellar disks in the 1980's (Adams et al. 1987; Kenyon & Hartmann 1987; Appenzeller et al. 1984). Direct imaging by *HST* confirmed it (HH 30, Burrows et al. 1996; silhouette disks, O'dell et al. 1993). Much observational evidence revealed that jets obtain energy through mass accretion toward central stars from accretion disks. An example for such evidence is the correlation between the mass accretion rate and mass loss rate from YSOs. The ratio of mass loss to accretion fluxes is $\sim$0.1, suggesting that 10% of accreting mass is ejected as a jet (Calvet et al. 1997). This is consistent with magnethydrodynamic (MHD) model calculations, which show that jets efficiently transport angular momentum from the stellar vicinity to the interstellar space. Although the magnetic field structure at the jet launching point located close to an accreting star is not clear at this moment, magnetically driven and collimated jets/winds provide the most natural explanation of these outflow phenomena in YSOs.

For low mass stars ($M < 2\ M_{\odot}$), YSOs show various forms of outflow activ-

ities depending on their evolutional phases (Class 0, I, II and III; Figure 1.1) such as optical jets, molecular outflows, high velocity neutral winds, T-Tauri winds and radio jets. Table 1.1 summarizes the characteristics (velocity, scale, mass loss rate, etc.) of those outflows. The outflows may be classified into three categories: a jet, wind or molecular outflow. The jets have fast velocities and are well-collimated and partially ionized. The winds also have high velocity, but are moderately-collimated and partially ionized or neutral. The molecular outflows are slow, poorly-collimated neutral gas that is believed to be entrained by faster outflows. Figure 1.2 shows a schematic of the various outflows. The characteristics of optical jets and molecular outflows are described in the following subsections in detail.

1.1.1 Optical Jets (Herbig Haro Objects)

Herbig-Haro (HH) objects are small nebulosities seen in star-forming regions, with their characteristic emission line optical spectra independently discovered by George Herbig (1951, 1952) and Guillermo Haro (1952, 1953). The emission line characteristics imply that the HH emission originates from the cooling region behind a shock wave (Schwartz 1975). Some HH objects are part of highly collimated jets (Dopita et al. 1982; Mundt & Fried 1983) and are called HH jets or HH flows. In some cases (HH34, HH1/2 and HH46/47), bright jets are associated with embedded protostars which show weak molecular outflows (Chernin & Masson 1991, 1995a; Olberg et al 1992). Those may be the cases when most of the molecular gas around the protostars are blown away and the visual extinction to the jets become low. Major bow shocks are often seen at the head of a protostellar jet (Reipurth 1989). Bally & Devine (1994) found the first parsec-scale jets from a low-mass star, showing that the HH 34 jet is merely the innermost part of a giant flow. The parsec-scale jets were subsequently confirmed by radial velocity and proper motion measurements. Devine et al. (1997) demonstrated that all the HH objects suspected of being part of the parsec-scale outflow from HH 34 are actually moving away from the driving source of HH 34. Giant HH flows provide fossil records of the evolution of protostars and their outflow activities, since the dynamical ages of the flows, typically several times 10^4 years, are comparable to the accretion ages of their driving sources.

Classical T Tauri stars (CTTSs) often show small-scale HH flows so called microjets with an extent of a few arcseconds (Solf 1997), much smaller than that of embedded protostars. Although direct imaging of microjets is difficult because of the presence of bright stars and reflection nebulae, long-slit spectroscopy enables efficient subtraction of the continuum in the vicinity of a central star, allowing detection of microjets (Solf 1989; Hirth et al. 1994a).

Optical forbidden lines of many T Tauri stars show blueshifted double-peaked profiles with respect to the systemic velocities. The redshifted emission is absent because the receding part of an outflow is obscured by a thick circumstellar disk (Mundt 1984; Edwards et al 1987; Appenzeller & Mundt 1989; Cabrit et al 1990; Hirth et al 1994a,b; Appenzeller et al. 1984; Edwards et al. 1994; Hamann, 1994; Hartigan et al. 1995). The high and low velocity peaks of the double-peaked line profiles are called the high velocity component (HVC) and the low velocity component (LVC), respectively. The HVC has a typical radial velocity of 50–150 km s^{-1}, while the LVC has 5–20 km s^{-1}. It has been interpreted that the two components originate from different viewing angle parts of a single outflow (e.g. Edwards et al. 1987; Hartmann & Raymond 1989; Gomez de Castro & Pudritz 1993; Ouyed & Pudritz 1993, 1994). Kwan & Tademaru (1988, 1995), on the other hand, proposed the presence of two physically different outflows in order to explain the two velocity components. The HVC is a well collimated, magnetically driven jet that originates from the star or from the inner edge of its accretion disk, while the LVC could be a slower wind originating from the disk within several AU from the star. The HVC is spatially more extended compared with the LVC. The peak emission of the HVC is located further away from the driving source than that of the LVC. The two velocity components have different densities and temperatures. Line ratios of various forbidden lines indicate that the gas in the LVC has generally higher density and lower excitation than that of the HVC (Hamann 1994).

High resolution observations revealed detailed structure of jets emanating from CTTSs. Spatial resolutions of $0\farcs1$ (Ray et al. 1996; Bacciotti et al. 2000, 2002; Coffey et al. 2004; Woitas et al. 2005) and $\sim0\farcs5$ (Dougados et al. 2000; Lavalley et al. 1997; Lavalley-Fouquet et al. 2000; Pyo et al. 2003) were achieved by *HST* and ground based telescopes with adaptive optics, respectively. Slit-less spectroscopy was carried out with *HST*/STIS (Hartigan et al. 2004). This technique enables us to obtain non-overlapping images at various emission line wavelengths including those that lack narrowband filters if the spectral resolution is sufficiently large. One of the high spatial resolution results is the study of the jet width as a function of distance from driving sources. The jet widths rapidly increase on a scale of 15–50 AU from the sources suggestive of a large opening angle of 20–30 degrees. Beyond 50 AU, they appear to increase gradually with a much smaller opening angle of a few degrees. The widths are 20–40 AU (FWHM) at ~100 AU away from the sources. Such variation of the jet width is consistent with magnetohydrodynamic disk wind models with medium to high efficiency ($\dot{M}_{\rm jet}/\dot{M}_{\rm acc} > 0.03$), where the efficiency is defined as the ratio of the total bipolar jet mass flux to the accretion rate (e.g., Garcia et al. 2001, Dougados et al. 2004).

Another manifestation of MHD models is the rotation of a jet around its axis. First observational hints of rotation were found in HH 212 at 10^4 AU from its driving source by Davis et al. (2000), who found radial veloicty asymmetry in the H_2 v=1-0 S(1) line emission across the HH 212 jet axis. The direction of rotation was consistent with that of the ammonia core around the source (Wiseman et al. 2001). Recent high angular resolution observations both from space and the ground revealed further indication of jet rotation across a jet width of 100–200 AU (Bacciotti et al. 2002; Coffey et al. 2004; Woitas et al. 2005). Such velocity asymmetries have been seen in all the T Tauri jets observed with *HST*/STIS (DG Tau, RW Aur, CW Tau, Th 28, and HH 30), with different emission lines and slit orientations both parallel and perpendicular to the outflow axis. For example, systematic shifts in radial velocity, typically from 5 to 25 $\pm$ 5 km s^{-1}, in the optical emission lines were found at jet positions displaced symmetrically with respect to the outflow axes, at 50–60 AU from driving sources and 20–30 AU from axis centers. The footpoint radius of jet components is derived from the above results from the measured v_ϕ and v_p under the assumption of a magneto-centrifugal wind (Anderson et al. 2003). This model suggests $B_\phi/B_\mathrm{p} \sim$ 3–4 at 30 AU from the axis and about 80 AU from the disk (Woitas et al. 2005). These values are consistent with disk wind models, and hence jets extract excess angular momentum from inner disks. However, recent radio observation revealed that the rotational direction of the disk around RW Aur is opposite to that of its jet (Cabrit et al. 2006). Further high-resolution observations should be conducted in order to confirm the rotation of jets.

Velocity channel maps show that jets have at their bases an onion-like kinematic structure, more collimated at higher velocities and excitation. The high velocity spine can be identified with the HVC. The channel maps also show progressively wider, slower and less excited layers further out from the outflow axis, in a continuous transition between the HVC and the LVC. At a distance of about 50–80 AU from driving sources, the low velocity material gradually disappears, while the axial HVC is seen to larger distances. The flow as a whole thus appears to be accelerated on a scale of 50–100 AU. The onion-shell structure has recently been seen extended out to the H_2-emitting region of outflow (Takami et al., 2004). Several small scale H_2 jets have been found recently in HH 72, HH 26, and HH 7-11. H_2 winds are also associated with well known jets from T Tauri stars, for example, DG Tau. In the latter case the emission originates from a warm (T $\sim$ 2000 K) molecular wind with a flow length and width of 40 and 80 AU, respectively, and has a radial velocity of $\sim$15 km s^{-1} (Takami et al., 2004). It is not clear if such a molecular component is entrained by the axial jet, or if it is a slow external component of the same disk wind that generates the fast jet.

1.1.2 Molecular Outflows

High velocity molecular gas ($\Delta V \sim 100$ km s^{-1}) was detected in CO (J=1-0) towards OMC-1 molecular cloud (Zuckerman et al. 1976; Kwan & Scoville 1976). Its nature was unknown until Snell et al (1980) discovered a bipolar molecular outflow with spatially separated blueshifted and redshifted gas in the dark cloud L1551. Since then, nearly 400 bipolar molecular outflows have been found so far (Wu et al. 1996; Wu et al. 2004). They can be roughly classified into two types: the Standard High-Velocity (SHV) component of V = a few km s^{-1} to about 30 km s^{-1} and the Extremely High-Velocity (EHV) component of $V \sim 100$ km s^{-1}. The CO molecues in these outflows observed in the millimeter-wavelength are collisionally excited at the temperature of $\sim$10 K at the density typically seen in molecular clouds.

SHV molecular outflows have been extensively studied (Bally & Lada 1983; Edwards & Snell 1982, 1983, 1984; Snell et al 1984). They are poorly collimated and contain most of the mass in an outflow (Bachiller 1996, Bachiller & Tafalla 1999). The masses of the molecular outflows (0.1–100 $M_\odot$, Fukui 1989) are the same or more than that of driving sources, implying that they are swept-up cloud gas rather than directly emanated from the protostars (Lada 1985; Fukui et al. 1993). Flow lengths are < 0.1 to $\sim$5 pc (Fukui et al. 1993). The collimation factor (length to width, or major to minor radii ratio) and initial opening angles of the CO outflows range from 3 to > 20 and 20° to 90°, respectively. Bolometric luminosity seems to be related with the mass, force, and mechanical luminosity (Bally & Lada 1983; Cabrit & Bertout 1992; Wu et al. 2004). Molecular outflows show the highest-observed radial velocities increase nearly linearly with distance from the source, so called the "Hubble law" (e.g., Uchida et al. 1987; Moriarty-Schieven & Snell 1988, 1989; Meyers-Rice & Lada 1991; Lada & Fich 1996; Tafalla et al. 1997).

High resolution and sensitivity observations at the millimeter-wavelength revealed the presence of jet-like CO molecular outflows at the extreamly high velocities (V $\sim$100 km s^{-1}) (Bachiller et al 1990). The EHV components have been found only in the highly embedded Class 0 protostars ($\sim 10^4$ yr) (L1448, Bachiller et al 1990; IRAS 03282, Bachiller et al 1991; HH211, Gueth & Guilloteau 1999). In some cases, EHV jets are formed by a series of molecular bullets interconnected with weak emission (Cernicharo & Reipurth 1996; Cernicharo et al. 1997). Typical size and mass of such bullets are 10^2 pc and 10^4 $M_\odot$, respectively (Bachiller et al 1990). Their kinematical time scale is from 10^3 to 10^4 yr. The molecular bullets seem to have the same origin as the successive shocked knots associated with optical and near-infrared jets (Reipurth 1989; Reipurth & Heathcote 1991a, 1992; Hartigan et al 1993;

Bally et al 1993; Eislöffel & Mundt 1994). The CO outflow mass decreases with increasing velocity from the systemic velocity of molecular clouds with a broken power law $dM(v)/dv \propto v^{-\gamma}$. The power law index ranges from 1 to 3 at low outflow velocities, and more than 10 in some cases at higher velocities (e.g., Masson & Chernin 1992; Rodríguez et al. 1982; Stahler 1994; Lada & Fich 1996). It rapidly falls off with age and energy in the outflow (Richer et al. 2000).

The SHV outflows are found as extended lobes surrounding EHV jets (Gueth & Guilloteau 1999; Tafalla et al. 2004; Lee et al. 2000). The maximum velocity of the EHV outflows decreases with distance from the outflow sources, while the maximum velocity of the SHV outflows increases with the distance. This strongly suggests that the EHV outflows entrain ambient gas to produce SHV outflows (Bachiller et al. 1990, 1991). As the YSOs age and their outflows evolve, the jets appear to fall off the degree of collimation and carve out large cavities from the surrounding medium to produce the classical outflow lobes. The evolution of the YSOs causes the jets to become less collimated and carve out large cavities from the surrounding medium to produce the classical outflow.

In some cases, the SiO emission was detected in molecular jets. The origin of the SiO molecular jets is mysterious at present, because SiO emission is believed to arise from outflow shocks and not from the entire length of jets. Three scenarios have been proposed so far; (a) protostellar jet, (b) the entrained gas (e.g., Stahler 1994; Raga et al. 1995) (c) shock excited (internal working surfaces, Raga & Cabrit 1993a).

Episodic ejection events seem to be a common property of young molecular outflows, causing discrete peaks in space and in velocity. Morphologically, an outflow is a superposition of several shocked/outflowing gas structures, as it shows multiple Hubble wedges in the position-velocity diagrams (Arce & Goodman 2001). Such a phenomenon can be explained by recurrent ejection events of outbursts such as the one observed in FU Ori stars as a result of an abrupt change in the accretion rate onto the central star (Reipurth 1989).

1.2 THEORITICAL MODELS OF OUTFLOWS

1.2.1 Launching Mechanisms of Jets

Many models have been proposed to explain bipolar molecular outflows so far. Radiation pressure from low mass protostars was not sufficient to drive the molecular outflows, since the momentum flux of a molecular outflow is typically two orders of magnitude larger than the photon momentum flux

L/c (Lada 1985). Thermal pressure is also insufficient when the gas sound speed is much less than the typical escape velocity. In fact, the temperatures of protostellar and T Tauri winds are $< 10^4$ K, thus the resulting sound speed $c_s < 10$ km s^{-1} is much smaller than the typical escape velocity of 200–400 km s^{-1}. Only magnetohydrodynamic (MHD) models are now seem to be favorable.

High velocity, highly collimated gas streams — jets — raise two major problems: how the jet material is accelerated and how it is collimated. The mass loss rates of "winds" observed in accreting T Tauri stars and FU Ori objects are roughly 10^{-1} of the mass accretion rates. The significance of this estimate can best be seen in terms of energy fluxes. Because typical wind or jet velocities are approximately a few times the Keplerian velocity of the inner disk, the above ratio of mass loss rates to accretion rates implies that similar amounts of energy are released in accretion and wind ejection. The process that accelerates the outflows of YSOs must be highly efficient in utilizing accretion power.

Magnetized rotating disks surrounding YSOs may allow to produce jets by converting a fraction of the gravitational energy released by mass accretion into outflow. Blandford & Payne (1982) proposed a magnetocentrifugally wind model driven from the surface of a magnetized accretion disk in order to explain galactic radio jets. The winds are accelerated along the magnetic field lines inside the Alfvén surface where the magnetic energy density becomes comparable to the kinetic energy density, if the magnetic fields are inclined by less than 60° from the disk plane. At the Alfvén surface, the rotation velocity is about the same as the Alfvén velocity of the gas, and the angular velocity of the gas decreases as it expands away from the surface by conservation of angular momentum. This decreasing angular velocity causes the magnetic field to wind up azimuthally through the inertia of the attached gas and generate a strong toroidal field, which is collimated toward the rotation axis. MHD models thus reasonably explain both the acceleration and collimation of a jet. When the model is applied to the YSO jets, it is divided into two types depending on the jet launching point, e.g., the disk surface or the star/disk boundary layer.

Pudritz & Norman (1983) proposed that molecular outflows are steady, centrifugally driven by the poloidal magnetic fields threading the disk. On the other hand, Uchida & Shibata (1985) proposed that magnetic pressure due to the twisted magnetic fields by disk rotation is also possible to drive the molecular outflow in a dynamic (non-steady) state. These disk wind models predicted that the classical molecular outflows, which show the velocity of $1 < V < 30$ km s^{-1} must be accelerated on the disk at 1–100 AU away from a central star. However, such regions have too low ionization because they

are located too far away from the central star, indicating that the external magnetic fields could be insufficient to launch the wind since they do not couple with the disk gas (Shu 1995).

Subsequently, these disk wind models are developed to explain high velocity jets and winds accelerated at the inner edge of the disk (e.g. Camenzind, 1990; Königl, 1995; Ferreira, 1997). Kudoh & Shibata (1995) confirmed that non-steady MHD models reproduce basically the same physical process as the magnetocentrifugally driven steady jet models. They also pointed out that the terminal velocity of a jet is of the order of Keplerian velocity at the footpoint of the jet and is comparable with the escape velocity from the central star. Furthermore, they suggested that even if the magnetic field is initially weak in the disk, the toroidal fields are generated from the poloidal fields by the rotation of the disk and the magnetic pressure force is dominated. These models are consistent with the interpretation that molecular outflows are the swept-up ambient gas accelerated by fast jets or winds rather than material directly ejected from a circumstellar disk.

On the other hand, Shu et al. (1988) proposed a model that a jet is generated at the region where the effective potential on the rigid rotation system with the angular velocity equal to that of stellar rotation has its maximum on the equatorial plane (the X-point). At the X-point located at a few to tens of stellar radii, the stellar magnetic fields interact with the inner edge of an accretion disk, and an outflow (X-wind) is generated along the open magnetic field lines. In the original model, a star should rotate at a breakup speed at its equator, while T Tauri stars rotate at about a tenth of this velocity (Bouvier et al 1986; Hartmann et al. 1986). Königl (1991) suggested that the stellar magnetic field is sufficiently strong to truncate a disk at the X-point radius R_X from the star. Later, the X-wind model has been modified to allow for the star rotating below breakup such as T Tauri stars (see Figure 1.3: Shu et al 1994a,b; Najita & Shu 1994; Ostriker & Shu 1995; Shu & Shang, 1997). This model also produces an infall funnel flow in addition to the bipolar outflow at the X-point. Detections of the inverse P Cygni absorption support the idea of the magnetic accretion onto stars from their disks (see Figure 1.4: Edwards et al. 1994; Hartmann et al. 1994. 1997).

The discovery of X-ray flares proved that protostars are in a very active phase of star formation (Montmerle et al. 1983; Koyama et al. 1994, 1996a, b). X-ray flares associated with YSOs show characteristics similar to solar flares, implying the thermal emission from the gas rapidly heated up (10^7–10^8 K) by the reconnection of magnetic fields. These mechanisms have been extensively applied to the YSO outflows (Hayashi et al. 1996; Hirose et al. 1997; Goodson et al. 1997, 1999). Hayashi et al. (1996) per-

formed time-dependent MHD numerical simulations assuming that the dipole magnetic field from a protostar threads the accretion disk (Figure 1.5). As the magnetic field is twisted by the rotation of the disk, magnetic pressure force is generated and expands in the same way as a solar flare. Eventually the reconnection of magnetic field lines occurs in a magnetic loop, and the high-temperature and high-velocity plasma is formed. This model reasonably explains jets and X-ray flares.

1.2.2 Entrainment Mechanisms of Molecular Outflows

Many CO molecular outflows are associated with collimated jets with similar orientations, suggesting that the two ejection phenomena are related with each other (e.g., L1551, Mundt & Fried 1983; HH1/2, Correia et al. 1997; Moro-Martin et al. 1999; HH34, Chernin & Masson 1995a; HH46/47, Olberg et al. 1992; HH111, Reipurth & Olberg 1991b; HH211, Gueth & Guilloteau 1999). If a jet is assumed to be fully ionized, the momentum of the optical jet is not sufficient to drive a molecular outflow (e.g., Mundt et al. 1987). Hartigan et al. (1994) found that the ionization fractions of jets is only a few percent. Bacciotti et al. (1999) also found that jets are partially ionized. In addition, the discovery of parsec-scale jets with wide-filed CCD detectors led to the large increase of the dynamical age of jets up to the accretion age of their driving sources (Bally & Devine 1994; Ogura et al. 1995). These results suggest that jets seem to provide sufficient momentum to drive molecular outflows (see §1.6).

To date, two major driving mechanism models have been proposed to explain molecular outflows: a wind-driven model and a jet-driven model. A schematic of molecular outflow properties predicted by different entrained models discussed below is shown in Figure 5. In the wind-driven model, wide-angle wind expands into a density-stratified ambient material through a forward shock, which runs ahead of the wind bubble. This produces widths consistent with observed poorly collimated molecular outflows in about 10^4 years and also the Hubble law, resulting from the sweep-up of a dense shell from a power law density distribution by a wide-angle wind (e.g., Shu et al. 1991, 1995, 2000; Shang et al. 1998; Matzner & McKee 1999). However, it is difficult to reproduce discrete bow shock features (e.g., Lee et al., 2000, 2002), and discrete position-velocity spur structures (and Hubble wedges). These models cannot explain the mass-velocity relation (much gas is contained at low velocities), observed spatial distribution of momentum of molecular outflows, and the morphology of the highly collimated CO molecular jet (Masson & Chernin 1992; Chernin & Masson 1995b). However, recent MHD simulations showed that, if the winds has a density gradient with little

gas along its polar axis, they have a wide opening angle at the base and the mass-velocity relation is reproduced as well as the shell structure of the CO outflow (Li & Shu 1996). They can also produce a dense jet-like structure at the downstream as a result of the MHD pinch effect (Shu et al. 1995; Ostriker 1997; Li & Shu 1996; Shang et al. 1998; Gardiner et al. 2003).

In the jet-driven model, highly collimated jets drive molecular outflows. Numerical hydrodynamical simulations performed by De Young (1986) categorized jet-driven model as two basic processes, i.e. the turbulent entrainment and prompt entrainment. The turbulent entrainment is the case where steady entrainment occurs within a viscous mixing layer along the outer surface of a jet as a result of the Kelvin-Helmholtz instability (De Young 1986; Canto & Raga 1991; Raga et al. 1993; Stahler 1994; Lizano & Giovanardi 1995; Canto et al. 2003). The numerical simulations (De Young 1986) show that the prompt entrainment is a dominant mechanism for intermediate Mach number jets ($M = 5 \sim 10$) with internal densities comparable to that of the external medium. Turbulent steady-state entrainment is the dominant process in low-velocity jets ($M \sim 1$).

In the jet-driven turbulent entrainiment model, the mixing layer grows both into the ambient gas and into the jet, and eventually the whole flow becomes turbulent. Some simulations are performed to estimate atomic emissions such as Hα and [SII] in order to investigate how molecular outflows are created by a turbulent jet (Raga et al. 2004; Micono et al. 1998). Radiatively cooled jet simulations reproduce the broken power law of the observed mass-velocity distribution (Micono et al. 2000). Shallower power law indices in the low velocity molecular outflows may come from the steady state entrainment. Such models seem to reproduce the velocity shear observed at the bases of some molecular outflows (Tafalla et al. 1993). However, these models produce decreasing molecular outflow momentum and velocity with distance from the source, contrary to that observed in most molecular outflows. In addition, they do not reproduce the observed poorly collimated molecular outflows (e.g., Stone & Norman 1993; Canto & Raga 1991, Raga et al. 1993; Chermin et al. 1994; Suttner et al. 1997; Völker et al. 1999).

In the jet-driven promt entrainment model, bow shocks at the head of a jet sweep up large amounts of ambient material and the prompt entrainment by the bow shocks produce a thin outflow shell around the jet (Raga & Cabrit 1993; Masson & Chernin 1993). These models successfully reproduce several observed features such as the forward momentum increase, Hubble law, and mass-velocity relation. They can also reproduce the PV spur structure, broad velocity widths of CO near H_2 shocks, the morphological relation between the CO and H_2 emission and the observed molecular widths seen in young and collimated outflows (Bachiller et al. 1995; Gueth & Guilloteau 1999; Lee

et al. 2001). However, they are difficult to reproduce the observed width of poorly collimated outflows because the shocked gas in the bow shock working surfaces limits the transverse momentum that can be delivered to the ambient medium.

Nonsteady jets with velocity variations produce internal shocks whose debris can splash sideways to widen the outflow channel, and the collision of the spreading postshock debris with the ambient medium accelerates it (Biro & Raga 1994; Raga & Kofman 1992; Kofman & Raga 1992). Jet precession also produce broad outflow lobes (Masson & Chernin 1993) and has been proposed to occur in several outflows based on outflow morphology (Shepherd et al. 2000; Bachiller et al. 2001). Thus, highly collimated and time-variable jets can drive poorly collimated lower-velocity molecular outflows by the combination of jet precession and internal velocity variations. This scenario is being numerically explored (e.g., Stone & Norman 1994; Suttner et al. 1997; Smith et al. 1997; Völker et al. 1999).

Whether jets or wide-angle winds drive molecular outflows is not clear, although many observations have been conducted so far. A combination of a jet-driven bow shock model and a wind-driven shell model could reasonably explain the characteristics of the observed molecular outflows (e.g., Nagar et al. 1997; Gueth & Guilloteau 1999; Lee et al. 2000; Yu et al. 1999; Arce and Goodman 2002). One possible explanation is that in an early phase, a dense collimated jet blows away a narrow part of the surrounding envelope along the jet axis. Less dense and wider wind might later entrain the gas unaffected by the collimated component, and then make the poorly collimated molecular outflow.

1.3 FORMATION MECHANISMS OF BOW SHOCKS/KNOTS

Recognizing that the emission lines from HH objects arise in the gas excited by the passage of shock waves, we can estimate physical quantities from their intensities, ratios, and line profiles (Schwartz 1975, 1978). When two fluids, such as a jet and ambient gas, impinge supersonically, a shock should propagate into each fluid (Figure 1.7). The forward shock, which accelerates the slower material, is the bow shock, while the reverse shock, which decelerates the faster gas closer to the star, is the Mach disk. Comparison of observed line ratios and plane-shock models showed that such models cannot explain the presence of both low-excitation lines (such as [OI] and [SII]) and high-excitation lines (such as [OIII] and [CIV]) simultaneously (Dopita 1978;

Raymond 1979).

On the other hand, bow-shock models successfully reproduce a range of shock velocities as the superposition of oblique angle plane shocks, with high-excitation lines produced at the apex and increasingly lower-excitation lines along the bow wings. In a comoving system of a bow shock, shocked gas appear to flow along the surface of the bow shock because the velocity parallel to the surface is conserved while that perpendicular is thermalized and significantly reduced (e.g., Hartmann & Raymond 1984; Hartigan et al. 1987; Raga et al. 1988; Raymond et al. 1988; Noriega-Crespo et al. 1990).

Bow shocks also naturally explain the large line widths because material is pushed aside from the flow axis as it enters the bow shock. Double-peaked emission line profiles characteristic of bow shocks were observed in a large number of objects and their position-velocity diagrams provide kinematics, shock velocity (FWZI seen in Hα), orientation angle, and physical conditions in the recombination regions of HH flows (Hartigan et al. 1987, 1987; Morse et al. 1994). Observed spectra are in good agreement with models for many outflows (e.g., Choe et al. 1985; Raga & Bohm 1985, 1986; Raga et al. 1986; Solf et al. 1986; Hartigan et al. 1990).

The Mach disks are probably time-variable structure, and would be affected by many instabilities (Blondin et al. 1990; Stone and Norman 1993). Theoretically, both bow shocks and Mach disks should be radiative (Hartigan 1989). In a large number of objects, both kinds of shock are found to show distinctively different line ratios and kinematics (Morse et al. 1992; Reipurth & Heathcote 1992). In many cases, the velocityof a bow shock is larger than that of a Mach disk, indicating that the jet has a higher density than the ambient gas. Although observations show that line widths and line excitations in bow shocks are larger than those in the jet ejecta, they are lower than those calculated for the bow shocks accelerate in quiescent ambient gas. Furthermore, shock velocities derived from line ratios of HH objects are often much lower than the 3-D velocities estimated from their proper motions and radial velocities. Thus, HH flows are formed by a series of nested bow shocks and the discrepancy between the shock and 3D velocities suggest that material ahead of the bow shocks is already moving at a substantial fraction of the jet speed into the wakes of previous mass ejections (Hartigan et al. 1990; Morse et al. 1994). In fact, high-resolution observations by *HST* have clearly shown such systems (Burrows et al. 1996; Heathcote et al. 1996; Ray et al. 1996; Reipurth et al. 1997; Hester et al. 1998). *HST* observations also revealed that the Hα bright filaments originate from collisional excitation of hydrogen at a shock front while the [SII] emission originates from a spatially extended region behind the shock as the gas cools and recombines. Morphology of Hα filaments shows that the filaments may be the wings of

one-sided bow shocks, where the outflow direction of the jet changes.

Raga et al. (1990) showed that a two-sided shock (internal working surface) is formed due to the time variability of the jet when faster material ejected at later times catches up slower moving material. The symmetry of locations and radial velocities of major bow shocks associated with a jet and counter jet would be caused by the intrinsic nature of the jet such as variability and instability rather than external causes (Devine et al. 1997; Gueth & Guilloteau 1999). Sinusoidal models with time variable jet ejection velocity suggest that spacing between major bow shocks seems to be in agreement with the eruptive cycles of FU Ori type stars. Such time variability would also be correlated with the orbital motion caused by the interaction within eccentric multiple systems (Reipurth 2000).

1.4 IONIZATION FRACTION AND LINE DIAGNOSIS

The ionization fraction, ratio of electron density to hydrogen density, is a key parameter to measure the mass in a jet. It is used to determine mass loss rates and mass momentum transfer rates, which provide useful constraints on theories of both accretion/ejection engines (Königl & Pudritz 2000; Shu et al. 2000) and interaction with ambient gas (Downes & Ray 1999; Suttner et al. 1997). The electron density is directly derived from the ratio of the [SII] 6716 Å and [SII] 6731 Å line intensities, while the hydrogen density can not. Thus the hydrogen density was previously derived from the assumed abundances of emitting species with respect to hydrogen together with the estimates of forbidden line luminosity and flow radius (Edwards et al. 1987; Cabrit et al. 1990). This approach is not popular because of the difficulty in estimating reliable reddening values.

Hartigan et al. 1994 estimated average ionization fractions in jets by comparing observed forbidden line ratios with those predicted by planar shock models, calculating radiative transfer with fixed cosmic abundances. The derived ionization fractions were 0.026 for HH34, 0.055 for HH47, and 0.052 for HH111, suggesting that jets are almost neutral. In this model, however, the ionization state of preshock gas significantly affects the line fluxes and flux ratios expected from a shock. Unfortunately, the preshock ionization state in front of a bow shock cannot be easily determined. If the UV radiation escaped forward from shock fronts fully ionizes all the incident material, then the fully preionization condition (H^+, He^{++}) should be employed. In contrast, if the ionization state of preshock gas is the same as that before the

shock passes, then the situation is similar to the equilibrium preionization. In such a case, the preshock gas is fully ionized at the apex of the bow but neutral at the lateral. Furthermore, the results are also affected by the assumed preshock conditions such as preshock density and magnetic field, and the assumed planar shock geometry.

Bacciotti et al. (1995) developed a spectroscopic diagnostic technique, allowing us to determine the ionization fraction in a jet without depending on models. This model assumes the abundances of [SII], [OI] and [NII] with respect to Hα and local ionization equilibrium for the fractional ionization of hydrogen. In the low excitation conditions in jets, the ionization fractions of oxygen and nitrogen are enhanced by charge exchange with hydrogen. Subsequently, Bacciotti et al. (1999) pointed out that Hα emission can be produced at physically different regions if the gas is not homogeneous, e.g., such as a region with high temperature (several 10^4) and moderate ionization where collisional excitation of hydrogen is dominated, or a region with low temperature (less than 6000–7000 K) moderate ionization where recombination emission is dominated. In a postshock cooling region where a steep temperature gradient is present, both emission mechanisms contribute to the Hα line emission. They then proposed that the Hα emission is not a proper probe to estimate physical conditions of emitting regions. On the contrary, since the forbidden lines arise from regions with similar temperature and ionization, they provide precise estimates of physical quantities (Bacciotti et al. 1999; Bally & Reipurth 2002). Only the forbidden lines, indeed, can be used for shock diagnostics, although the accuracy is low (Bacciotti et al. 1999; Hartigan et al. 1994). In addition, the ionization fraction (derived from [OI] (6300 Å + 6363 Å)/[NII] (6548 Å + 6583 Å)) and electron temperature (derived from [SII] (6716 Å + 6731 Å)/[OI] (6300 Å + 6363 Å)) can be determined from the relative fluxes of the brightest lines in a jet without assuming a heating mechanism. As demonstrated by Hartigan et al. (1994), weak shocks in jets cannot produce high ionization regions more than a few percent at the shock fronts. On the contrary, Bacciotti et al. (1995) suggested that typical recombination time in jet gas is the same order as the travel time of bright section of the jet. Thus, if the jet gas is ionized at the acceleration region, it can be partially ionized even at a large distance from the source. In such a case, the ionization fraction is determined by the recombination time and flow speed, decreasing with distance from the source along the jet. Since this model does not take into account photoionization, it cannot be applied to a jet in an HII region. This model was applied to a large number of jets to which long-slit and integral filed spectra were obtained with *HST*/STIS (Bacciotti & Eislöffel 1999; Lavalley-Fouquet et al. 2000; Dougados et al. 2000; Bacciotti 2002). The forbidden line ratios in these

jets are reasonably interpreted by shock excitation rather than by turbulent mixing layer or ambipolar diffusion (Lavalley-Fouquet et al. 2000; Dougados et al. 2003). In the case of DG Tau, to which the spectra were obtained with *HST*/STIS, the electron density (N_e) is highest when the position is closest to the star and on the axial region and when the veocity is highest. At the jet base, the ionization fraction is typically $0.01 \leq N_e \leq 0.4$. It rapidly increases with distance from the source and becomes constant at 100–200 AU from the source, slowly decreasing following a recombination curve. In the same region the total density is up to 10^6 cm^{-3} and the electron temperature (T_e) is from 8×10^3 to 2×10^4 K. These values are similar to those predicted by MHD disk wind models (Königl & Pudritz 2000; Shu et al. 1995; Cabrit, Ferreira & Raga 1999; Lery & Frank 1999). The mass flux rate ($\dot{M}_{\rm jet}$) in jets, determined from the density, jet diameter and de-projected velocity, is $\sim 10^{-7}$ M$\odot$ yr^{-1}, with the colder and slower external layers of a jet contributing most to the flux. The mass accretion rate $\dot{M}_{\rm acc}$ is determined from line veiling (Hartigan et al. 1995). The ratio of $\dot{M}_{\rm jet}$ to $\dot{M}_{\rm acc}$ ranges from 0.05 to 0.1, which seems to be consistent with warm disk winds rather than cold disk wind models (Casse & Ferreira 2000).

1.5 THE GOAL OF THIS THESIS

As described in §1.3.2, it is not clear how molecular outflows are driven. In order to understand this, one should investigate the interaction between jet/wind and ambient gas in detail. However, previous observations did not provide accurate estimates of physical conditions in jets because they were preformed at insufficient angular and spectroscopic resolutions with low positional accuracy. I therefore used the High Dispersion Spectrograph of the Subaru Telescope to study the kinematics and physical conditions of the entire jets with high positional accuracy. I made slit-scan observations of Hα and [NII] toward HH46/47 (Chapter 2) and HL Tau (Chapter 3) and discuss how the observed jets interact with ambient gas in this thesis.

The large aperture of the Subaru telescope and the high velocity resolution of the HDS allowed us to investigate the kinematics of the entire jets in unprecedented detail. The HDS slit viewer allowed us to measure slit positions with high accuracy. Assuming the jet-driven model, I discuss whether the prompt or turbulent entrainment mechanism predominantly works in the two cases. In addition, I derive the physical conditions in the jets and preshock gases by performing comparison with the observed [NII]/Hα flux ratios and those predicted by shock models.

Reference

Adams, F. C., Lada, C. J., & Shu, F. H. 1987, ApJ, 312, 788
Anderson, J. M., Li, Z.-Y., Krasnopolsky, R., & Blandford, R. D. 2003, ApJ, 590, L107
André, P. 2002, EAS Publications Series, 3, 1
Appenzeller, I., Oestreicher, R., & Jankovics, I. 1984, A&A, 141, 108
Appenzeller, I., & Mundt, R. 1989, A&ARv, 1, 291
Arce, H., & Goodman, A. 2001, ASP Conf. Ser. 235: Science with the Atacama Large Millimeter Array, 235, 99
Arce, H. G., & Goodman, A. A. 2002, ApJ, 575, 928
Bacciotti, F., Chiuderi, C., & Oliva, E. 1995, A&A, 296, 185
Bacciotti, F., & Eislöffel, J. 1999, A&A, 342, 717
Bacciotti, F., Mundt, R., Ray, T. P., Eislöffel, J., Solf, J., & Camezind, M. 2000, ApJ, 537, L49
Bacciotti, F., Ray, T. P., Mundt, R., Eislöffel, J., & Solf, J. 2002, ApJ, 576, 222
Bachiller, R., Martin-Pintado, J., Tafalla, M., Cernicharo, J., & Lazareff, B. 1990, A&A, 231, 174
Bachiller, R., Martin-Pintado, J., & Planesas, P. 1991, A&A, 251, 639
Bachiller, R., Guilloteau, S., Dutrey, A., Planesas, P., & Martin-Pintado, J. 1995, A&A, 299, 857
Bachiller, R. 1996, ARAA, 34, 111
Bachiller, R., & Tafalla, M. 1999, NATO ASIC Proc. 540: The Origin of Stars and Planetary Systems, 227
Bachiller, R., Pérez Gutiérrez, M., Kumar, M. S. N., & Tafalla, M. 2001, A&A, 372, 899
Bally, J., & Lada, C. J. 1983, ApJ, 265, 824
Bally, J., Lada, E. A., & Lane, A. P. 1993, ApJ, 418, 322
Bally, J., & Devine, D. 1994, ApJ, 428, L65
Bally, J., & Reipurth, B. 2002, Revista Mexicana de Astronomia y Astrofisica Conference Series, 13, 1
Biro, S., & Raga, A. C. 1994, ApJ, 434, 221
Blandford, R. D., & Payne, D. G. 1982, MNRAS, 199, 883
Blondin, J. M., Fryxell, B. A., & Königl, A. 1990, ApJ, 360, 370
Bouvier, J., Bertout, C., Benz, W., & Mayor, M. 1986, A&A, 165, 110
Burrows, C. J., et al. 1996, ApJ, 473, 437
Cabrit, S., Edwards, S., Strom, S. E., & Strom, K. M. 1990, ApJ, 354, 687
Cabrit, S., & Bertout, C. 1992, A&A, 261, 274
Cabrit, S., Ferreira, J., & Raga, A. C. 1999, A&A, 343, L61
Cabrit, S., Pety, J., Pesenti, N., & Dougados, C. 2006, A&A, 452, 897

Calvet, N. 1997, IAU Symp. 182: Herbig-Haro Flows and the Birth of Stars, 182, 417
Camenzind, M. 1990, Reviews in Modern Astronomy, 3, 234
Canto, J., & Raga, A. C. 1991, ApJ, 372, 646
Cantó, J., Raga, A. C., & Riera, A. 2003, Revista Mexicana de Astronomia y Astrofisica, 39, 207
Casse, F., & Ferreira, J. 2000, A&A, 353, 1115
Cernicharo, J., & Reipurth, B. 1996, ApJ, 460, L57
Cernicharo, J., Neri, R., & Reipurth, B. 1997, IAU Symp. 182: Herbig-Haro Flows and the Birth of Stars, 182, 141
Chernin, L. M., & Masson, C. R. 1991, ApJ, 382, L93
Chernin, L., Masson, C., Gouveia dal Pino, E. M., & Benz, W. 1994, ApJ, 426, 204
Chernin, L. M., & Masson, C. R. 1995a, ApJ, 443, 181
Chernin, L. M., & Masson, C. R. 1995b, ApJ, 455, 182
Choe, S.-U., Boehm, K.-H., & Solf, J. 1985, ApJ, 288, 338
Coffey, D., Bacciotti, F., Woitas, J., Ray, T. P., & Eislöffel, J. 2004, ApJ, 604, 758
Correia, J. C., Griffin, M., & Saraceno, P. 1997, A&A, 322, L25
Davis, C. J., Berndsen, A., Smith, M. D., Chrysostomou, A., & Hobson, J. 2000, MNRAS, 314, 241
De Young, D. S. 1986, ApJ, 307, 62
Devine, D., Bally, J., Reipurth, B., & Heathcote, S. 1997, AJ, 114, 2095
Dopita, M. A. 1978, ApJS, 37, 117
Dopita, M. A., Evans, I., & Schwartz, R. D. 1982, ApJ, 263, L73
Dougados, C., Cabrit, S., Lavalley, C., & Ménard, F. 2000, A&A, 357, L61
Dougados, C., Cabrit, S., Lopez-Martin, L., Garcia, P., & O'Brien, D. 2003, ApSS, 287, 135
Dougados, C., Cabrit, S., Ferreira, J., Pesenti, N., Garcia, P., & O'Brien, D. 2004, Ap&SS, 292, 643
Downes, T. P., & Ray, T. P. 1999, A&A, 345, 977
Edwards, S., & Snell, R. L. 1982, ApJ, 261, 151
Edwards, S., & Snell, R. L. 1983, ApJ, 270, 605
Edwards, S., & Snell, R. L. 1984, ApJ, 281, 237
Edwards, S., Cabrit, S., Strom, S. E., Heyer, I., Strom, K. M., & Anderson, E. 1987, ApJ, 321, 473
Edwards, S., Hartigan, P., Ghandour, L., & Andrulis, C. 1994, AJ, 108, 1056
Eisloeffel, J., & Mundt, R. 1994, A&A, 284, 530
Ferreira, J. 1997, A&A, 319, 340
Fukui, Y. 1989, Low Mass Star Formation and Pre-main Sequence Objects, 95

Fukui, Y., Iwata, T., Mizuno, A., Bally, J., & Lane, A. P. 1993, Protostars and Planets III, 603
Garcia, P. J. V., Cabrit, S., Ferreira, J., & Binette, L. 2001, A&A, 377, 609
Gardiner, T. A., Frank, A., & Hartmann, L. 2003, ApJ, 582, 269
Gomez de Castro, A. I., & Pudritz, R. E. 1993, ApJ, 409, 748
Goodson, A. P., Winglee, R. M., & Boehm, K.-H. 1997, ApJ, 489, 199
Goodson, A. P., Böhm, K.-H., & Winglee, R. M. 1999, ApJ, 524, 142
Gueth, F., & Guilloteau, S. 1999, A&A, 343, 571
Haro, G. 1952, ApJ, 115, 572
Haro, G. 1953, ApJ, 117, 73
Hamann, F. 1994, ApJS, 93, 485
Hartigan, P., Raymond, J., & Hartmann, L. 1987, ApJ, 316, 323
Hartigan, P. 1989, ApJ, 339, 987
Hartigan, P., Raymond, J., & Meaburn, J. 1990, ApJ, 362, 624
Hartigan, P., Morse, J. A., Heathcote, S., & Cecil, G. 1993, ApJ, 414, L121
Hartigan, P., Morse, J. A., & Raymond, J. 1994, ApJ, 436, 125
Hartigan, P., Edwards, S., & Ghandour, L. 1995, ApJ, 452, 736
Hartigan, P., Edwards, S., & Pierson, R. 2004, ApJ, 609, 261
Hartmann, L., & Raymond, J. C. 1984, ApJ, 276, 560
Hartmann, L., Hewett, R., Stahler, S., & Mathieu, R. D. 1986, ApJ, 309, 275
Hartmann, L., & Raymond, J. C. 1989, ApJ, 337, 903
Hartmann, L., Hewett, R., & Calvet, N. 1994, ApJ, 426, 669
Hartmann, L. 1997, IAU Symp. 182: Herbig-Haro Flows and the Birth of Stars, 182, 391
Hayashi, M. R., Shibata, K., & Matsumoto, R. 1996, ApJ, 468, L37
Heathcote, S., Morse, J. A., Hartigan, P., Reipurth, B., Schwartz, R. D., Bally, J., & Stone, J. M. 1996, AJ, 112, 1141
Herbig, G. H. 1951, ApJ, 113, 697
Herbig, G. H. 1952, ApJ, 116, 369
Hester, J. J., Stapelfeldt, K. R., & Scowen, P. A. 1998, AJ, 116, 372
Hirose, S., Uchida, Y., Shibata, K., & Matsumoto, R. 1997, PASJ, 49, 193
Hirth, G. A., Mundt, R., & Solf, J. 1994a, A&A, 285, 929
Hirth, G. A., Mundt, R., Solf, J., & Ray, T. P. 1994b, ApJ, 427, L99
Kenyon, S. J., & Hartmann, L. 1987, ApJ, 323, 714
Königl, A. 1991, ApJ, 370, L39
Kofman, L., & Raga, A. C. 1992, ApJ, 390, 359
Königl, A. 1995, Revista Mexicana de Astronomia y Astrofisica Conference Series, 1, 275
Königl, A., & Pudritz, R. E. 2000, Protostars and Planets IV, 759
Koyama, K., Maeda, Y., Ozaki, M., Ueno, S., Kamata, Y., Tawara, Y., Skinner, S., & Yamauchi, S. 1994, PASJ, 46, L125

Koyama, K., Tsuboi, Y., & Ueno, S. 1996a, IAU Colloq. 153: Magnetodynamic Phenomena in the Solar Atmosphere - Prototypes of Stellar Magnetic Activity, 243
Koyama, K., Hamaguchi, K., Ueno, S., Kobayashi, N., & Feigelson, E. D. 1996b, PASJ, 48, L87
Kudoh, T., & Shibata, K. 1995, ApJ, 452, L41
Kwan, J., & Scoville, N. 1976, ApJ, 210, L39
Kwan, J., & Tademaru, E. 1988, ApJ, 332, L41
Kwan, J., & Tademaru, E. 1995, ApJ, 454, 382
Lada, C. J. 1985, ARAA, 23, 267
Lada, C. J., & Fich, M. 1996, ApJ, 459, 638
Lavalley, C., Cabrit, S., Dougados, C., Ferruit, P., & Bacon, R. 1997, A&A, 327, 671
Lavalley-Fouquet, C., Cabrit, S., & Dougados, C. 2000, A&A, 356, L41
Lee, C.-F., Mundy, L. G., Reipurth, B., Ostriker, E. C., & Stone, J. M. 2000, ApJ, 542, 925
Lee, C.-F., Stone, J. M., Ostriker, E. C., & Mundy, L. G. 2001, ApJ, 557, 429
Lee, C.-F., Mundy, L. G., Stone, J. M., & Ostriker, E. C. 2002, ApJ, 576, 294
Lery, T., Frank, A., Henriksen, R. N., & Fiege, J. D. 1999, Star Formation 1999, Proceedings of Star Formation 1999, held in Nagoya, Japan, June 21 - 25, 1999, Editor: T. Nakamoto, Nobeyama Radio Observatory, p. 291-292, 291
Li, Z.-Y., & Shu, F. H. 1996, ApJ, 472, 211
Lizano, S., & Giovanardi, C. 1995, ApJ, 447, 742
Masson, C. R., & Chernin, L. M. 1992, ApJ, 387, L47
Masson, C. R., & Chernin, L. M. 1993, ApJ, 414, 230
Matzner, C. D., & McKee, C. F. 1999, ApJ, 526, L109
Meyers-Rice, B. A., & Lada, C. J. 1991, ApJ, 368, 445
Micono, M., Massaglia, S., Bodo, G., Rossi, P., & Ferrari, A. 1998, A&A, 333, 1001
Micono, M., Bodo, G., Massaglia, S., Rossi, P., Ferrari, A., & Rosner, R. 2000, A&A, 360, 795
Montmerle, T., Koch-Miramond, L., Falgarone, E., & Grindlay, J. E. 1983, ApJ, 269, 182
Moriarty-Schieven, G. H., & Snell, R. L. 1988, ApJ, 332, 364
Moriarty-Schieven, G. H., & Snell, R. L. 1989, ApJ, 338, 952
Moro-Martín, A., Cernicharo, J., Noriega-Crespo, A., & Martín-Pintado, J. 1999, ApJ, 520, L111
Morse, J. A., Hartigan, P., Cecil, G., Raymond, J. C., & Heathcote, S. 1992,

ApJ, 399, 231
Morse, J. A., Hartigan, P., Heathcote, S., Raymond, J. C., & Cecil, G. 1994, ApJ, 425, 738
Mundt, R., & Fried, J. W. 1983, ApJ, 274, L83
Mundt, R. 1984, ApJ, 280, 749
Mundt, R., Brugel, E. W., & Buehrke, T. 1987, ApJ, 319, 275
Nagar, N. M., Vogel, S. N., Stone, J. M., & Ostriker, E. C. 1997, ApJ, 482, L195
Najita, J. R., & Shu, F. H. 1994, ApJ, 429, 808
Noriega-Crespo, A., Bohm, K. H., & Raga, A. C. 1990, AJ, 99, 1918
O'dell, C. R., Wen, Z., & Hu, X. 1993, ApJ, 410, 696
Ogura, K. 1995, ApJ, 450, L23
Olberg, M., Reipurth, B., & Booth, R. S. 1992, A&A, 259, 252
Ostriker, E. C., & Shu, F. H. 1995, ApJ, 447, 813
Ostriker, E. C. 1997, ApJ, 486, 291
Ouyed, R., & Pudritz, R. E. 1993, ApJ, 419, 255
Ouyed, R., & Pudritz, R. E. 1994, ApJ, 423, 753
Pudritz, R. E., & Norman, C. A. 1983, ApJ, 274, 677
Pyo, T.-S., et al. 2003, ApJ, 590, 340
Raga, A. C., & Bohm, K.-H. 1985, ApJS, 58, 201
Raga, A. C., Bohm, K. H., & Solf, J. 1986a, AJ, 92, 119
Raga, A. C., & Bohm, K. H. 1986b, ApJ, 308, 829
Raga, A. C., Mateo, M., Bohm, K.-H., & Solf, J. 1988, AJ, 95, 1783
Raga, A. C., Binette, L., Canto, J., & Calvet, N. 1990, ApJ, 364, 601
Raga, A. C., & Kofman, L. 1992, ApJ, 386, 222
Raga, A. C., Canto, J., Calvet, N., Rodríguez, L. F., & Torrelles, J. M. 1993, A&A, 276, 539
Raga, A. C., Cabrit, S., & Canto, J. 1995, MNRAS, 273, 422
Raga, A. C., Beck, T., & Riera, A. 2004, APSS, 293, 27
Ray, T. P., Mundt, R., Dyson, J. E., Falle, S. A. E. G., & Raga, A. C. 1996, ApJ, 468, L103
Raymond, J. C. 1979, ApJS, 39, 1
Raymond, J. C., Hartmann, L., & Hartigan, P. 1988, ApJ, 326, 323
Reipurth, B. 1989, Nature, 340, 42
Reipurth, B., & Heathcote, S. 1991a, A&A, 246, 511
Reipurth, B., & Olberg, M. 1991b, A&A, 246, 535
Reipurth, B., & Heathcote, S. 1992, A&A, 257, 693
Reipurth, B., Hartigan, P., Heathcote, S., Morse, J. A., & Bally, J. 1997, AJ, 114, 757
Reipurth, B., Yu, K. C., Heathcote, S., Bally, J., & Rodríguez, L. F. 2000, AJ, 120, 1449

Richer, J. S., Shepherd, D. S., Cabrit, S., Bachiller, R., & Churchwell, E. 2000, Protostars and Planets IV, 867
Rodríguez, L. F., Carral, P., Moran, J. M., & Ho, P. T. P. 1982, ApJ, 260, 635
Schwartz, R. D. 1975, ApJ, 195, 631
Schwartz, R. D. 1978, ApJ, 223, 884
Shang, H., Shu, F. H., & Glassgold, A. E. 1998, ApJ, 493, L91
Shepherd, D. S., Yu, K. C., Bally, J., & Testi, L. 2000, ApJ, 535, 833
Shu, F. H., Lizano, S., Ruden, S. P., & Najita, J. 1988, ApJ, 328, L19
Shu, F. H., Ruden, S. P., Lada, C. J., & Lizano, S. 1991, ApJ, 370, L31
Shu, F., Najita, J., Ostriker, E., Wilkin, F., Ruden, S., & Lizano, S. 1994a, ApJ, 429, 781
Shu, F. H., Najita, J., Ruden, S. P., & Lizano, S. 1994b, ApJ, 429, 797
Shu, F. H., Najita, J., Ostriker, E. C., & Shang, H. 1995, ApJ, 455, L155
Shu, F. H., & Shang, H. 1997, IAU Symp. 182: Herbig-Haro Flows and the Birth of Stars, 182, 225
Shu, F. H., Najita, J. R., Shang, H., & Li, Z.-Y. 2000, Protostars and Planets IV, 789
Smith, M. D., Suttner, G., & Yorke, H. W. 1997, A&A, 323, 223
Snell, R. L., Loren, R. B., & Plambeck, R. L. 1980, ApJ, 239, L17
Snell, R. L., Scoville, N. Z., Sanders, D. B., & Erickson, N. R. 1984, ApJ, 284, 176
Solf, J., Boehm, K.-H., & Raga, A. C. 1986, ApJ, 305, 795
Solf, J. 1989, Low Mass Star Formation and Pre-main Sequence Objects, 399
Solf, J. 1997, IAU Symp. 182: Herbig-Haro Flows and the Birth of Stars, 182, 63
Stahler, S. W. 1994, ApJ, 422, 616
Stone, J. M., & Norman, M. L. 1993, ApJ, 413, 198
Stone, J. M., & Norman, M. L. 1994, ApJ, 420, 237
Suttner, G., Smith, M. D., Yorke, H. W., & Zinnecker, H. 1997, A&A, 318, 595
Tafalla, M., & Bachiller, R. 1993, Bulletin of the American Astronomical Society, 25, 855
Tafalla, M., Bachiller, R., Wright, M. C. H., & Welch, W. J. 1997, ApJ, 474, 329
Tafalla, M., Santiago, J., Johnstone, D., & Bachiller, R. 2004, A&A, 423, L21
Takami, M., Chrysostomou, A., Ray, T. P., Davis, C., Dent, W. R. F., Bailey, J., Tamura, M., & Terada, H. 2004, A&A, 416, 213
Uchida, Y., & Shibata, K. 1985, PASJ, 37, 515
Uchida, Y., Kaifu, N., Shibata, K., Hayashi, S. S., Hasegawa, T., & Hamatake,

H. 1987, PASJ, 39, 907
Völker, R., Smith, M. D., Suttner, G., & Yorke, H. W. 1999, A&A, 343, 953
Wiseman, J., Wootten, A., Zinnecker, H., & McCaughrean, M. 2001, ApJ, 550, L87
Woitas, J., Bacciotti, F., Ray, T. P., Marconi, A., Coffey, D., & Eislöffel, J. 2005, A&A, 432, 149
Wu, Y., Huang, M., & He, J. 1996, A&AS, 115, 283
Wu, Y., Wei, Y., Zhao, M., Shi, Y., Yu, W., Qin, S., & Huang, M. 2004, A&A, 426, 503
Yu, K. C., Billawala, Y., & Bally, J. 1999, AJ, 118, 2940
Zuckerman, B., Kuiper, T. B. H., & Rodríguez Kuiper, E. N. 1976, ApJ, 209, L137

Outflow	Diagnostics	Velocity (km s^{-1})	Scale (AU)	Mass Loss Rate (M yr^{-1})	Collimation	Observation
Jet						
Optical Jet HH Jet / flow	Optical & NIR Forbidden Line Emissions ([S II], [O I], [N II], [Fe II], H2), Hα Emission	100–400	10^3–10^6	10^{-8}–10^{-7} (Ionization fraction taken into account)	Well	Many Class 0 & I. Some Class II. Partially ionized
Radio Jet	Thermal Continuum	–	10–10^2	$< 10^{-7}$–10^{-5}	Well	Some Class 0 & I
Wind						
T Tauri Wind	Optical Permitted Line P Cygni Absorptions (Hα, Na D, Ca II, Mg II)	50–200	> 0.1 AU	10^{-8}–10^{-7}	Unresolved	All Class II
T Tauri Forbidden Emission Line Region	Optical & NIR Forbidden Line Emissions, Hα Emission	5–20 (LVC) (50–100 HVC=Jet)	> 0.1 AU	$< 10^{-7}$	Unresolved	All Class II. Two velocity components
High Velocity Neutral Wind	OH (1665 & 1667 MHz), HI	50–200	10^4–10^6	10^{-8}–10^{-7}	Moderate	A few Class I. Neutral
Molecular Outflow						
Extremely High Velocity Molecular Outflow	CO, SiO	40–150	10^4–10^6	10^{-7}–10^{-6}	Moderate	Some Class 0 & I. Neutral
"Classical" Bipolar Molecular Outflow	CO	1–30	10^4–10^6	10^{-7}–10^{-6}	Poor	All Class 0 & I. Some Class II. Neutral

Table 1.1: Type of Outflows from Young Stars

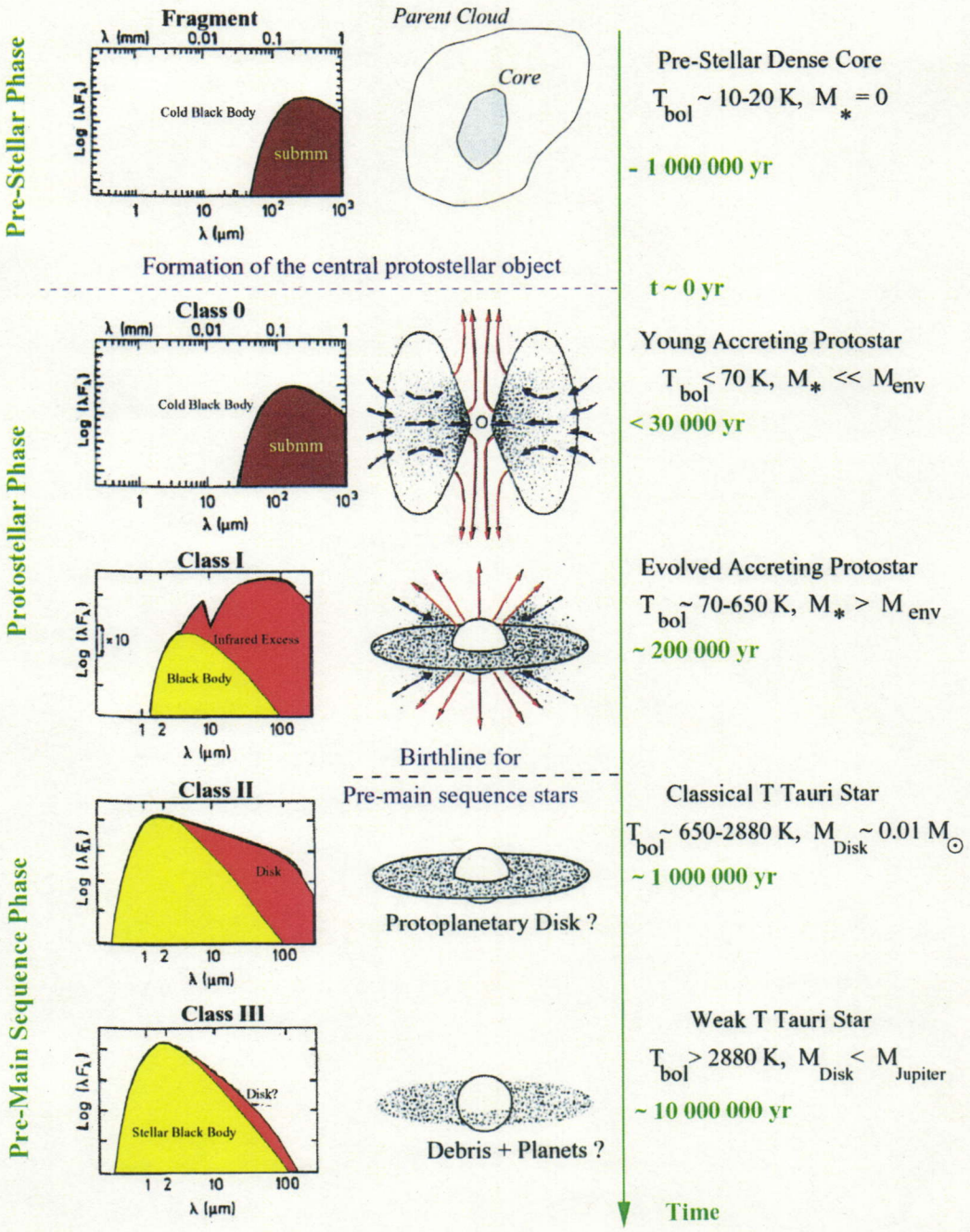

Figure 1.1: Empirical evolutionary sequence of the formation for low mass YSOs (André 2002). Spectral energy distribution and schematic diagram for each stage are shown on the left and middle, respectively. Bolometric temperature, mass of circumstellar disk and age are also indicated on the right.

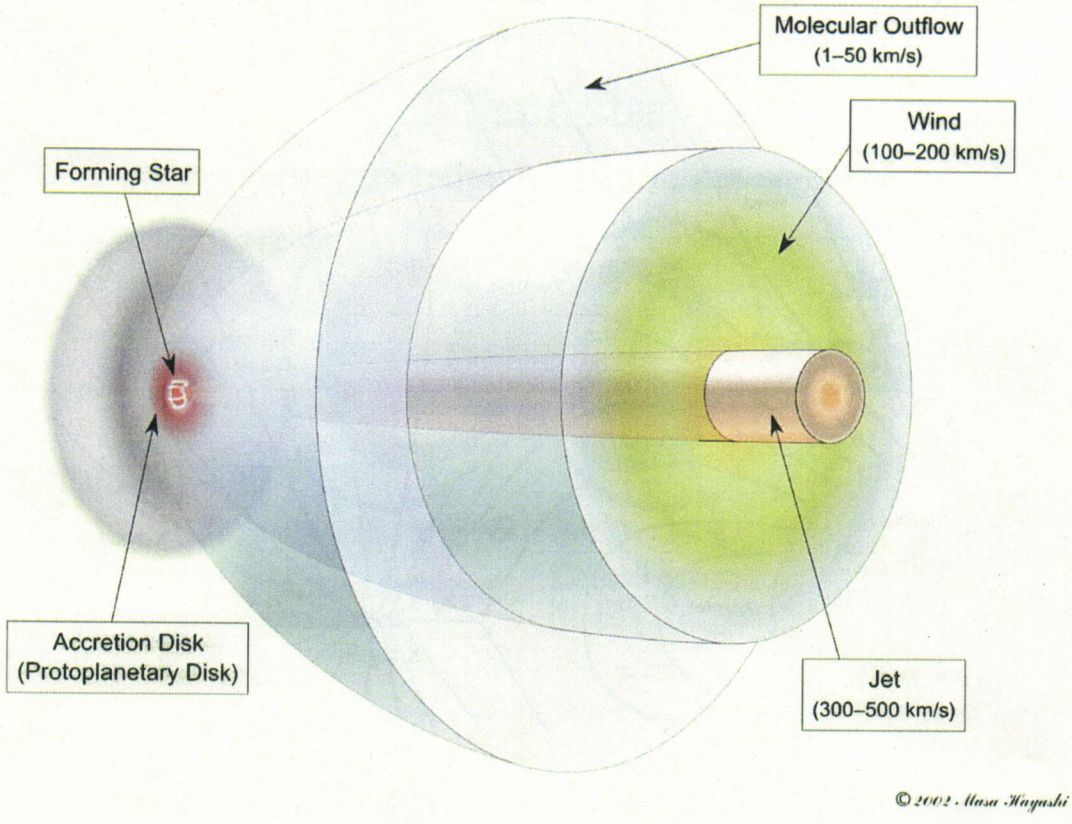

Figure 1.2: A schematic of various outflows emanating from a YSO (Hayashi, private communication).

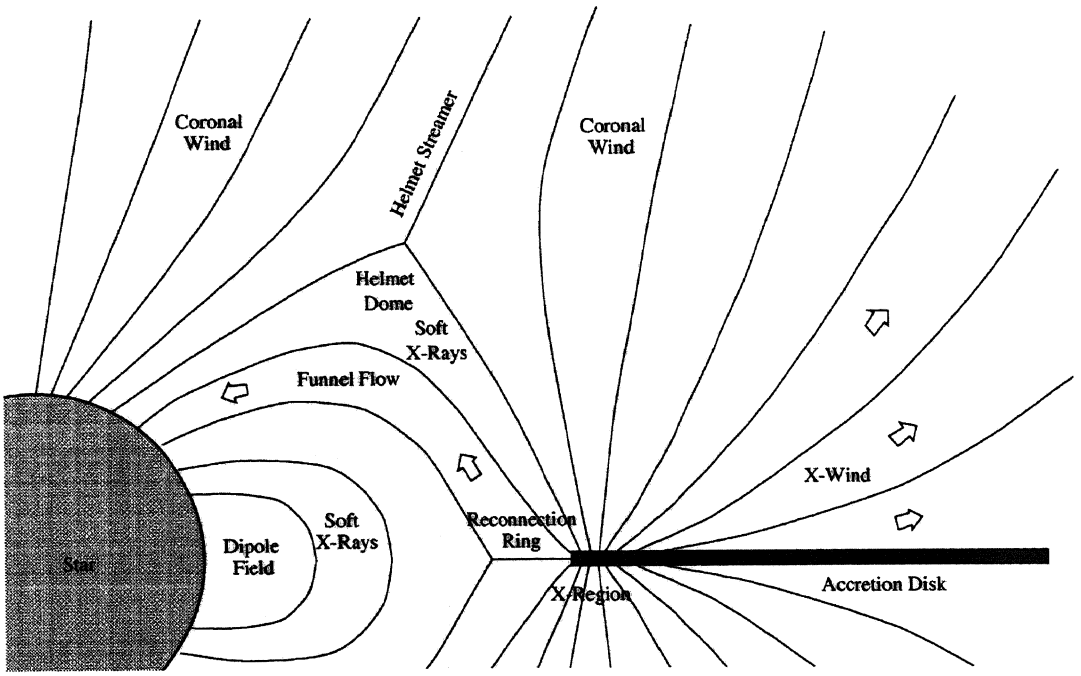

Figure 1.3: A schematic diagram of the X-wind model (Shu & Shang 1997).

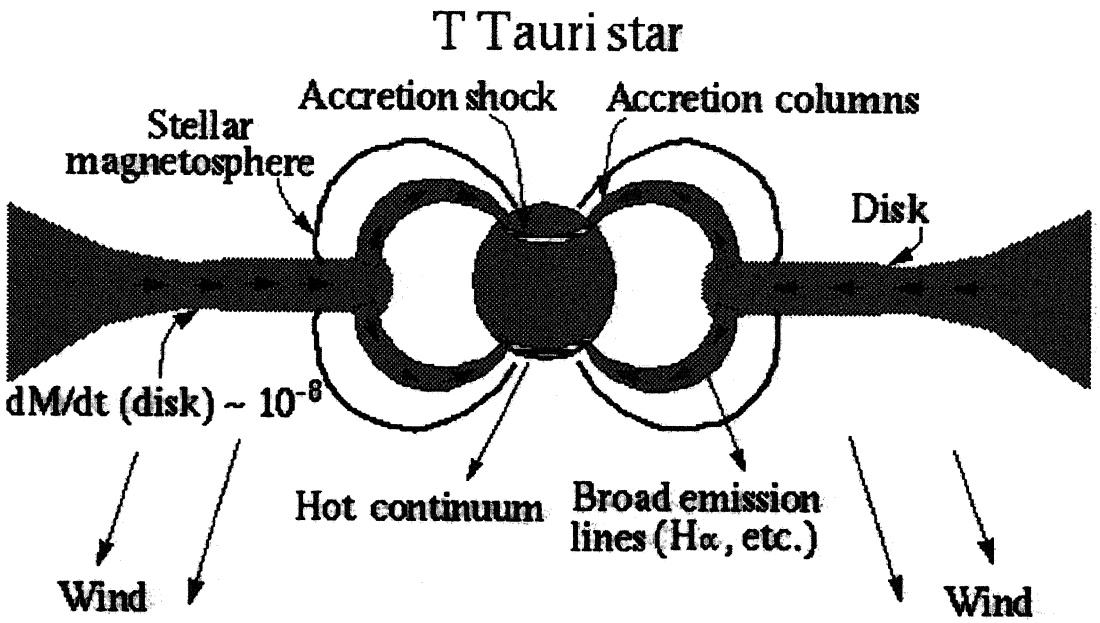

Figure 1.4: A schematic picture of accretion close to the T-Tauri stars (Hartmann 1997).

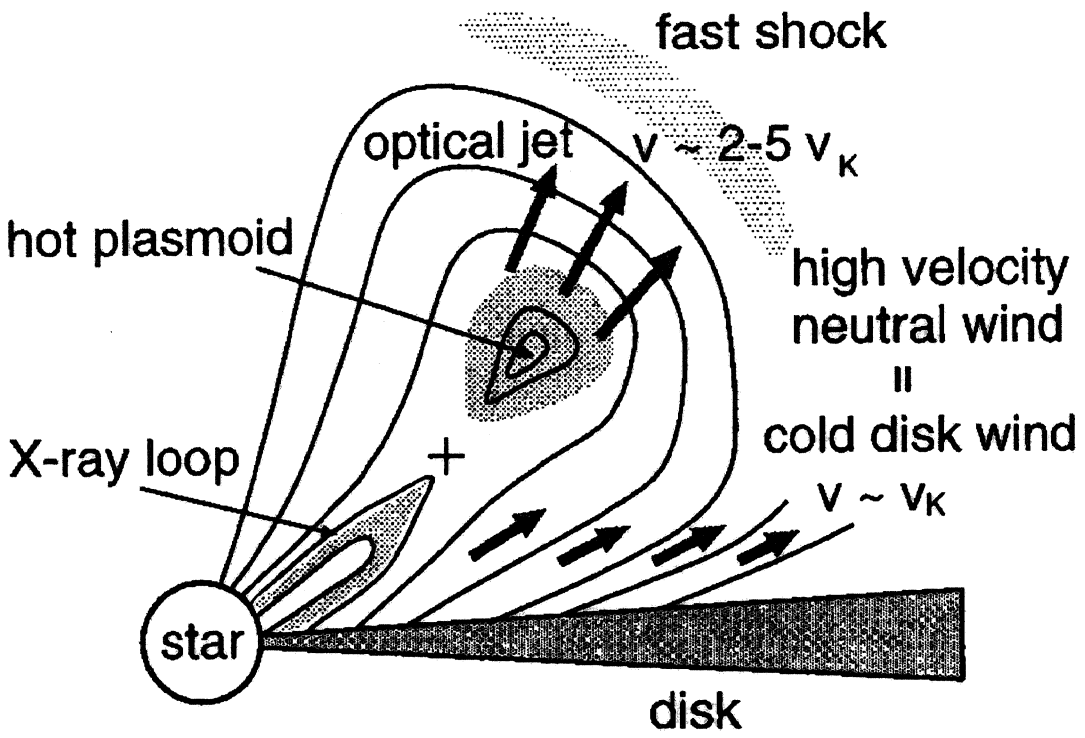

Figure 1.5: A schematic picture of an MHD simulation with reconnection by twisted dipole magnetic field (Hayashi et al. 1996).

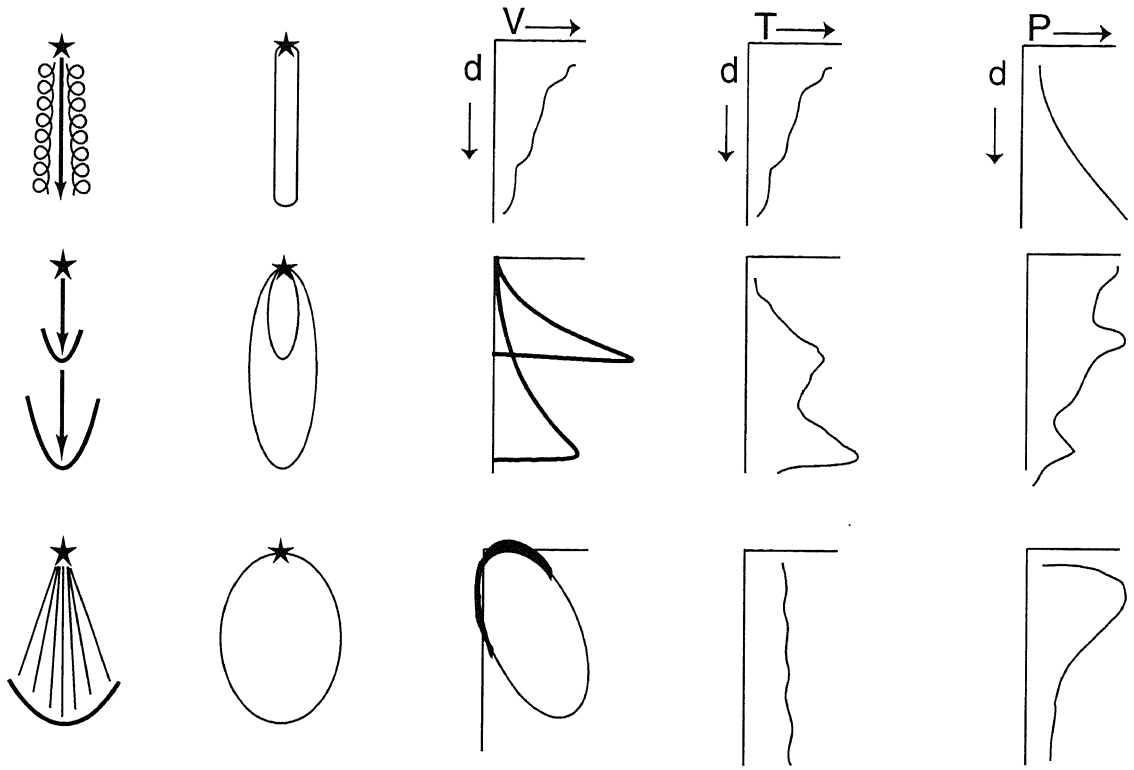

Figure 1.6: Observable molecular outflow properties predicted by three entrainment models (Arce & Goodman 2002): (1) turbulent jet (top); (2) jet bow shock (middle); (3) wide-angle wind (bottom). The columns from the left show a schematic drawing of the stellar wind and the model-predicted molecular outflow morphology, velocity profile, temperature profile, and momentum profile.

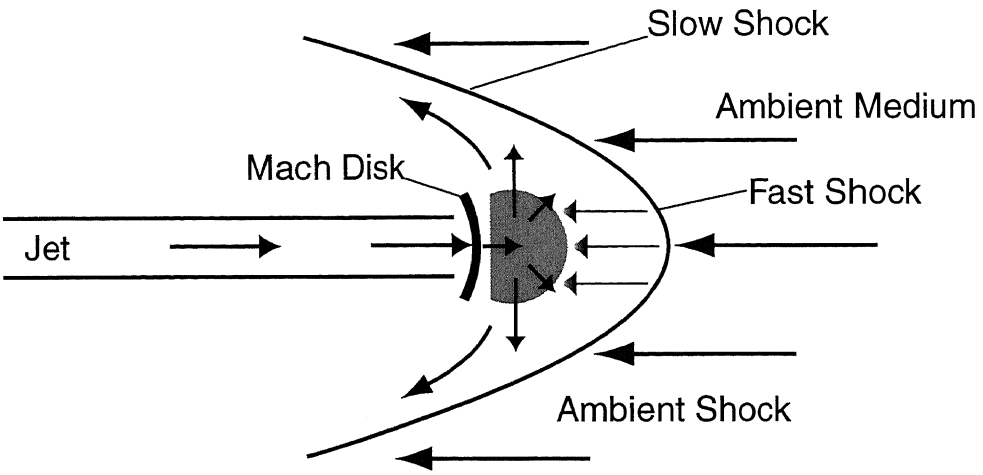

Figure 1.7: A schematic picture of the structure of a bow shock.

Chapter 2

SUBARU HIGH-DISPERSION SPECTROSCOPY OF Hα AND [NII] 6583 Å EMISSION IN THE HH 46/47 JET

Abstract

We present slit-scan observations of the Hα and [NII] 6583 Å emission lines toward the HH 46/47 jet with the Subaru Telescope. The spectral resolution of R = 3.6×10^4 allowed for studying kinematics of individual features in unprecedented detail. The Hα emission shows a main jet component ($V_{\rm LSR} \sim -160$ km s^{-1}) and distinct lower velocity components ($|V_{\rm LSR}| \leq 120$ km s^{-1}). The [NII] emission is primarily associated with the main jet component and it is much fainter or absent in the lower velocity components. The velocity of Hα and [NII] emissions in the main jet component well matches each other. The lower velocity components are associated with one-sided bow shocks, and also an Hα filament previously identified using the *Hubble Space Telescope*. While the main jet component is associated with the ejecta of the jet, these low velocity components are due to interaction between the jet and surrounding gas. The line profiles of the bow shocks and an Hα filament suggest that the surrounding gas moves outwards by ~ 200 km s^{-1}, similar to those for HH 47A and 47D. We conclude that this motion is due to prompt entrainment. In contrast to the previous observations, our high-resolution spectra do not show the presence of turbulent mixing layers. The [NII]/Hα ratios in some regions are remarkably higher than a typical ratio suggested by previous observations ([NII]/H$\alpha \sim 0.2$). Such regions include some regions in the main jet component (0.2–0.5), and also at the apices of the bow shocks ($\sim$0.5) and Hα filaments ($\sim$0.3). In contrast, the ratio is much smaller ($<$0.1) at the lateral of the bow shocks and Hα filaments. A possible interpretation is that the preshock gas is partially ionized in the main jet component, and also at the apices of bow shocks and Hα filaments (ionization fraction $\leq$ 0.2), while the ambient gas surrounding the jet is almost neutral. The same diagnostics is applied to the Hα filamentary structure in the HH 46 region, whose nature is not clear. We conclude that this feature is due to interaction between the jet and surrounding gas, analogous to the bow shock and the other Hα filament downstream.

2.1 INTRODUCTION

Optical jets and molecular bipolar outflows are two major manifestations of outflowing activities in young stellar objects (YSOs) (Mundt & Fried 1983; Bachiller 1996; Richer et al. 2000). Jets are highly collimated, while molecular outflows show various morphologies and velocities. It is not clear how these activities are related with each other. One of the major scenarios is that a collimated jet seen in the optical-IR wavelength entrains the ambient molecular material, allowing the molecular outflow to occur (e.g., Raga & Cabrit 1993; Masson & Chernin 1993). To tackle this issue, it is crucial to understand how the jet interacts with the ambient material.

Two entrainment scenarios have been proposed to date: these are, prompt entrainment and turbulent entrainment. According to the prompt entrainment scenario, bow shocks sweep up ambient material at the ahead and the edge of the jet (see e.g., Raga & Cabrit 1993; Masson & Chernin 1993; Davis et al. 1997). According to the turbulent entrainment scenario, surrounding material is entrained along the body of the jet in the turbulent mixing layer (Cantó & Raga 1991; Stahler 1994; Bachiller et al. 1994; Riera et al. 2001; Woitas et al. 2002). The prompt entrainment models predict that momentum per unit length decreases with distance from the source, while the turbulent entrainment models predict that it should increase as the distance increases (Masson & Chernin 1993; Chernin & Masson 1995). Recent observations using the *Hubble Space Telescope* (*HST*) have supported the prompt entrainment scenario (e.g. HH 1, Hester et al. 1998; HH 111, Reipurth et al. 1997; HH 34, Reipurth et al. 2002).

Mass loss rates and mass momentum transfer rates in a jet are key parameters to investigate how the jet interacts with the ambient material (Hartigan, Morse, & Raymond 1994; Bacciotti & Eislöffel 1999). If we assume that the jet is fully ionized, the mass momentum of the jet measured from its optical emission line is not sufficient to drive the molecular outflows (Mundt, Brugel, & Buehrke 1987). However, recent studies have suggested that the ionization fraction in the jet is only a few per-cents, indicating that the jet is almost neutral (e.g., Hartigan et al. 1994; Raga 1991; Bacciotti, Chiuderi, & Oliva 1995). If this is the case, the jet may have a momentum sufficient to drive a molecular outflow (Mitchell et al. 1994; Chenin & Masson 1995). However, mass momentum is poorly known because the electron density is directly derived (e.g., from the ratio of the [SII] doublet at 6716 Å and 6731 Å), while the hydrogen density is not.

The HH 46/47 system was discovered in the dense Bok globule ESO 210-6A, which is located in the Gum Nebula (Schwartz 1977). It contains prominent Herbig-Haro jets (HH 46, HH 47A–D) emanating from the infrared

source HH 46 IRS. The bright jet elongated to the northeast is conspicuous against the globule and is blueshifted with respect to the infrared driving source. HH 47A is a bright bow shock at the terminus of the blueshifted jet 1.′3 away from the infrared source. HH 47D is a faint blueshifted bow shock seen at $\sim$50″ away from HH 47A (Morse et al. 1994). Recent observations using the *HST* have shown the wiggled morphology of the jet in detail (Heathcote et al. 1996). The counter jet is faint to the southwest because of large extinction (Reipurth & Heathcote 1991). HH 47C is a redshifted bow shock $\sim$2′ away from the driving source (Eislöffel & Mundt 1994). The radial velocity (Meaburn & Dyson 1987; Hartigan et al. 1993; Morse et al. 1994) and proper motion (Eislöffel & Mundt 1994; Hartigan et al. 2005) of the knots indicate that the inclination angle of the HH 46/47 jet is $\sim$53° to the line of sight with the total velocity of $\sim$300 km s^{-1}. The driving source is a binary system with a separation of 0.″26 and the luminosities of $\sim$5 $L_\odot$ and $\sim$7 $L_\odot$ (Reipurth et al. 2000). The distance to this system has been estimated at 350 (Eislöffel et al. 1994) to 450 pc (Graham & Heyer 1989).

In this paper we present the high-resolution spectroscopy of the Hα 6563 Å and [NII] 6583 Å emission associated with the HH 46/47 jet. Slit-scan observations with a long-slit provided the kinematic information of the jet in unprecedented detail.

2.2 OBSERVATIONS AND DATA REDUCTION

We performed slit-scan observations with the High Dispersion Spectrograph (HDS) mounted on the Nasmyth focus of the 8.2-m Subaru Telescope on December 18–19 2002. The long-slit mode with a 1″ × 60″ slit provided a spectral resolution $\lambda/\Delta\lambda = 3.6 \times 10^4$ (8.3 km s^{-1}) on two 4k × 2k CCDs with a 13.5 μm pixel size. An order-blocking filter centered on 6580 Å allowed us to obtain the spectra at 6541–6588 Å. The spectra thus cover the Hα 6563 Å and also [NII] 6583 Å lines. The slit was placed parallel to the jet axis (P.A. = 58.°6), and the spectra were obtained at eight positions with a $\sim$1″ separation. Figure 2.1 shows the slit positions, labeled as SP1 to SP8 from the southwest to the northwest. Table 2.1 shows the offset of the slit positions with respect to SP1. Stars on a slit viewer allowed us to measure the offsets with a positional accuracy of 0.″2. The exposure time was 1800 s for each slit position. The average seeing was 0.″7.

Data were reduced with the IRAF packages. We removed bad pixels and cosmic-ray events, and subtracted the sky background. The dark cur-

rent, which is stable at 10 e^- per hour, was subtracted together with the sky background. We performed the wavelength calibration using a Th-Ar lamp and the IRAF tasks IDENTIFY, REIDENTIFY, FITCOORDS, and TRANSFORM in the noao.twodspec.longslit package. Relative atmospheric transparency was calibrated using stars in the slit viewer.

2.3 RESULTS

Figure 2.2 shows the position-velocity diagram (PVD) of the Hα and [NII] emission summed for the eight slit positions. The vertical axis Y indicates the projected angular distance from the south-eastern end of the slit position. HH 46 IRS is located near $0\farcs7$ on SP2. The PVD shows three prominent components described below. First, there is a bright component at $V_{\rm LSR} \sim -4$ km s^{-1} extended over the entire slit. This component peaks at -8 km s^{-1} $\leq V_{\rm LSR} \leq -4$ km s^{-1} and -4 km s^{-1} $\leq V_{\rm LSR} \leq 3$ km s^{-1} at $Y \leq 40''$ and $Y \geq 40''$, respectively. The $FWHM$ velocity is $\sim$30 km s^{-1} over the entire slit. Second, an extended blueshift component is seen at -260 km s^{-1} $\leq V_{\rm LSR} \leq -50$ km s^{-1} for $Y \geq 15''$. The typical radial velocity and $FWHM$ velocity are $V_{\rm LSR} = -160$ km s^{-1} and 45 km s^{-1}, respectively. Third, a broad velocity component is seen at $Y \leq 15''$. This component extends over a velocity range of -300 km s^{-1} $\leq V_{\rm LSR} \leq +200$ km s^{-1}. The component appears to be asymmetric about the systemic velocity of the molecular core of $V_{\rm LSR} = +5$ km s^{-1} (Kuiper et al. 1987; de Vries et al. 1984) because of the prominent velocity feature at -260 km s^{-1} $\leq V_{\rm LSR} \leq -110$ km s^{-1} and $0'' \leq Y \leq 8''$, which is in fact part of the first component.

All the components are shown by previous spectroscopic observations including Meaburn & Dyson (1987), Hartigan, Raymond, & Meaburn (1990), and Reipurth & Heathcote (1991). The origin of these components was discussed in detail by the authors. The bright component at $V_{\rm LSR} \sim -3$ km s^{-1} originates from a diffuse H_2 region ionized by the nearby O stars ζ Pup and γ^2 Vel, and also the ionization rim of the globule ESO 210-6A, in which HH46/47 IRS is embedded (Hartigan et al. 1990). The blueshifted component is associated with the HH 46/47 jet (Meaburn & Dyson 1987; Hartigan et al.1990). The broad velocity component is a scattered Hα emission of HH 46/47 IRS (Reipurth & Heathcote 1991). The rest of the paper is focused on the second component: the blueshifted component associated with the jet.

Figure 2.3 shows the PVDs at eight slit positions with the corresponding slit positions on the Hα image taken by Hartigan (private communication). We measured the locations of knotty features with their peak radial velocities and velocity widths on each slit and summarized them in Table 2.2. Some

knots are labelled on the PVDs and in Table 2.2 according to Eislöffel & Mundt (1994), who identified them in their [SII] image.

The slit position 1 (hearafter SP1) is placed at the edge of the jet. At this position the [SII] 6716 + 6731 Å emission is not seen in the image obtained by Eislöffel & Mundt (1994). In our PVD, however, two bright features are seen in Hα at $Y = 19''$ and $23''$. The latter shows a large velocity variation from $V_{\rm LSR} = -145$ km s^{-1} to -185 km s^{-1} for $Y = 21''$ to $25''$. A fainter and less blueshifted feature is seen at $Y = 26''$.

In the PVD for SP2, the feature corresponding to HH 46-1 becomes clear at $Y \sim 3''$ mingled in the scattered Hα light from the driving source. It has a peak radial velocity of $V_{\rm LSR} = -220$ km s^{-1}, 60 km s^{-1} blueshifted compared with the typical radial velocity of the jet ($V_{\rm LSR} \sim -160$ km s^{-1}). The PVD at $Y = 18''$–$28''$ shows three knotty features, which are also seen at SP1. These features are brighter at SP2 than SP1. The position of the feature around $Y = 23''$ coincides with the knot B7. This feature shows a large velocity gradient ($\Delta V \sim 20$ km s^{-1} at $Y = 21''$–$24''$). In addition to these features, fainter features are apparent at $Y = 35''$–$41''$.

At SP 3, diffuse emission appears between all the knotty structures distributed from HH 46-1 to $Y \sim 40''$. For the rest of the paper, we use the term "the main jet component" for this chain of knotty structure with diffuse emission. The HH 46-1 feature is brightest at SP3. The emission complex at $Y = 23''$ corresponds to B7′, a feature close to B7 but identified as a separate feature by Eislöffel & Mundt (1994). It has a velocity structure similar to B7. A low velocity feature appears at $V_{\rm LSR} = -80$ km s^{-1}, $Y \sim 41''$.

In the PVD for SP4, the bright emission feature corresponding to HH 46-1 becomes faint while the other features corresponding to HH 46-2 and HH 46-NW are apparent. Mingled with the scattered Hα line, the emission features for HH 46-2 and HH 46-NW lie spatially displaced by $\sim 2''$ from each other. HH 46-2 has a slightly less blueshifted radial velocity than HH 46-1. There is an emission feature connecting HH 46-2/HH 46-NW and B8, a bright knot located around $Y = 21''$, where the slit intersects the Hα knot complex. The feature corresponding to the knot B6 appears while that of the knot B7 becomes fainter. The main jet component then extends from B6 to A26 at $V_{\rm LSR} \sim -160$ km s^{-1} through HH 47B (B0). The typical angular scale and velocity variation are $1''$–$4''$ and 10–30 km s^{-1}, respectively. A low velocity feature at $V_{\rm LSR} = -110$ km s^{-1} is seen at $Y \sim 42''$. Another low velocity feature is visible associated with the knot complex B6 and B8.

The PVD for SP5 shows the features very similar to that for SP4 because the slit positions overlap with each other in some extent. The feature for HH 46-2, however, disappears.

HH 46-NW becomes weak at SP6. The slit position is close to the curved

emission ridge at $Y = 10''$–$20''$ seen in the *HST* image, thus the features in this region are bright. The emission in the jet shows a peak at $Y \sim 28''$, and this corresponds to B4. HH 47B shows two velocity components at $V_{\rm LSR} \sim -110$ km s^{-1} and -170 km s^{-1} with similar brightness to each other. The main jet component then reaches the knot A22 at $Y = 46''$. The lower velocity component at $Y = 21''$ shows a peak velocity at $V_{\rm LSR} \sim -70$ km s^{-1}.

At SP7, the slit is mostly on the ridge of the Hα jet at $Y = 10''$–$20''$, where the emission shows a velocity at $V_{\rm LSR} \sim -150$ km s^{-1}. The main jet component beyond this position becomes broken into separate features corresponding to HH 47B and A22. The lower velocity emission is now brighter at $Y = 34''$, where SP7 intersects the flank of a bow shock corresponding to HH 47B. The velocity in this feature increases with Y: $V_{\rm LSR} = -80$ km s^{-1} and -120 km s^{-1} at $Y = 32''$ and $Y = 36''$, respectively. The lower velocity emission at $Y = 21''$ is brighter than that at SP6.

In the PVD for SP8, features at $Y < 40''$ become faint, and diffuse emission between the knots diminishes. At $Y > 40''$, the knotty features corresponding to A15, A18, A20 and A23 appear with diffuse emission connecting the knots. The knots corresponding to A15, A18 and A20 show a peak velocity $V_{\rm LSR} \sim -170$ km s^{-1}, $\sim$10 km s^{-1} blueshifted from the main jet component at $Y < 40''$. The feature corresponding to A23 shows a peak velocity $V_{\rm LSR} \sim -160$ km s^{-1}, same as the main jet component at $Y < 40''$. The high velocity peak associated with HH 47B disappears. The lower velocity component associated with HH 47B shows a velocity $V_{\rm LSR} \sim -80$ km s^{-1}.

To examine the kinematics of the jet in a different manner, we show in Figure 2.4 the Hα line profile for individual $1'' \times 1''$ grids. The major component shows a gaussian-like symmetric profile in most of the regions, with a $FWHM$ velocity of 30–50 km s^{-1}. The lower velocity ($|V_{\rm LSR}| \leq 120$ km s^{-1}) components are seen as redward wings or asymmetry of the line profiles in the following regions: knot B8 ($Y = 20''$–$23''$, SP6 and SP7) and knot B4 ($Y = 26''$ and $27''$, SP6). At HH 46 ($Y = 4''$–$5''$ in SP4), HH 47B ($Y = 33''$–$35''$ in SP6) and $Y = 40''$ in SP4 and SP5, the line profile shows two velocity components: i.e. the higher velocity component (i.e. "the main jet component" described above) and an additional lower velocity component.

Heathcote et al. (1996) suggest that preshock medium around the jet is tenuous, neutral material ($\leq$100 cm^{-3}). In such a region, one might expect that Balmer hydrogen lines have both a broad component caused by proton-neutral charge exchange and a narrow component caused by excitation of cold neutrals entering the shock, such as supernova remnants (Chevalier & Raymond 1978; Ghavamian et al. 2001). We carefully compared our spectra with literature that shows such two components. However, we do not find clear evidence for a symmetric broad component due to charge exchange.

Figure 2.5 shows the PVDs of the [NII] 6583 Å emission in contours superposed on the Hα emission in gray scale. The distribution of [NII] appears to match the main jet component of Hα. In contrast, the [NII] emission does not show the presence of the low velocity ($|V_{\rm LSR}| \leq 120$ km s^{-1}) components seen in the Hα emission. Furthermore, while the PVDs for Hα shows a scattered emission within 15″ of the driving source, the [NII] emission does not show this component.

Figure 2.6 shows the flux distribution of Hα and [NII] integrated over the velocity (from -313 km s^{-1} to -37 km s^{-1}), and also the distribution of the [NII]/Hα flux ratio. The flux distribution of the [NII] image is similar to Hα, although the peak at HH 47B is far less clear in the [NII] image. The observed [NII]/Hα flux ratio ranges between 0.2 and 0.5, highest at the knot B8. The ratio shows clear correlation with the flux distribution of Hα except for HH 47B. The measured [NII]/Hα flux ratio in some regions is significantly larger than the previous observations ($\sim$0.2) by Morse et al. (1994). This discrepancy clearly shows the importance of the slit-scan technique with the accurate slit positioning, which we performed this time.

In the following subsections we describe the results of HH 46 ($0'' \leq Y \leq 8''$), HH 47B ($33'' \leq Y \leq 36''$) and the Hα filaments at the flank of the knots B7, A26 and A22 ($23'' \leq Y \leq 25''$, $40'' \leq Y \leq 42''$, $44'' \leq Y \leq 47''$) in detail.

2.3.1 HH 46

Figure 2.7 shows the line profiles in the HH 46 region. The region includes HH 46-1 (SP3, $Y = 3\farcs9$), HH 46-2 (SP4, $Y = 5\farcs6$) and an Hα filamentary structure (SP 5, $4'' \leq Y \leq 9''$) mingled with the scattered light from the driving source. Our slit-scan observations reveal the two velocity components described below.

The higher velocity component in Hα emission lies at SP3 and SP4, and this is likely to be associated with the main jet component. The peak velocity and $FWHM$ velocity in this component are $V_{\rm LSR} \sim -210$ km s^{-1} and $V_{\rm FWHM} \sim 50$ km s^{-1}, respectively. The peak velocity is $\sim$50 km s^{-1} larger than the typical peak velocity in the main jet component ($V_{\rm LSR} \sim -160$ km s^{-1}). The velocity of this component decreases by 20 km s^{-1} toward the downstream from SP3 (a) to SP3 (e). The lower velocity component in Hα emission, corresponding to HH 46-NW in Figure 2.3, lies at SP4 and SP5. The peak velocity and $FWHM$ velocity are $V_{\rm LSR} \sim -150$ km s^{-1} and $V_{\rm FWHM} \sim 60$ km s^{-1}, respectively. The position of this component corresponds with the Hα filamentary structure seen in the HST image. The radial velocity of the Hα filament gradually increases with Y: ~ -150 km s^{-1} at SP5, $Y = 5''$, and ~ -175 km s^{-1} at SP5, $Y = 8''$.

Toward the downstream, the radial velocity of the higher velocity component decreases whereas its tangential velocity increases. The higher velocity component at HH 46-1 and HH 46-2 shows a peak velocity of ~ -220 km s^{-1} and ~ -200 km s^{-1}, respectively, in our spectra. Proper motion measurements by Hartigan et al. (2005) have shown the tangential velocity of 261 km s^{-1} and 273 km s^{-1} at HH 46-1 and HH 46-2, respectively. These results are explained if the jet has a constant 3D velocity of 340 km s^{-1}, and it changes the direction by 4° along the line of sight in the HH 46 region.

The [NII] emission also shows the two velocity components corresponding to those in Hα. However, the lower velocity component is significantly fainter than the higher velocity component. The higher velocity component peaks at $V_{\rm LSR} \sim -210$ km s^{-1} as well as the Hα emission. The $FWHM$ velocitys at SP3 and SP4 are $\sim$40 km s^{-1}, $\sim$10 km s^{-1} lower than Hα. The [NII]/Hα flux ratios are $\sim$0.6 at HH 46-1 and HH 46-2. In contrast to the Hα emission, the lower velocity component in [NII] emission is significantly faint. The [NII]/Hα flux ratio is between 0.1 and 0.2 along the low velocity.

In addition to the two velocity components, the intermediate velocity component lies at the apex of the Hα filament in Hα emission (SP4–SP5, e-g). The peak velocity and $FWHM$ velocity are $V_{\rm LSR} \sim -170$ km s^{-1} and $V_{\rm FWHM}$ $\sim$ 60 km s^{-1}, respectively. This component is explained by blending of the two velocity components, i.e. the higher velocity component decreases its velocity toward the downstream, and the lower velocity component increases its velocity toward the same direction. In contrast to the Hα emission, the [NII] emission shows only the higher velocity component at the same position. The [NII]/Hα flux ratio is $\sim$0.3 at the apex of the Hα filament.

The *HST* image in Figure 2.7 shows the presence of bright emission at SP6 as well as SP3–4. However, the Hα and [NII] emission at SP6 is much fainter than SP3-4. This indicates that the emission at SP6 of the *HST* image mainly results from the scattered continuum emission from the driving source, not the Hα emission.

2.3.2 HH 47B

Figure 2.8 shows the line profiles in the HH 47B region. This region includes the main jet component in SP4 and SP5, and a one-sided bow shock in SP6, SP7 and SP8. The main jet component has a single velocity in Hα emission. The peak velocity and $FWHM$ velocity in this component are $V_{\rm LSR} \sim -170$ km s^{-1} and $V_{\rm FWHM} \sim 30$ km s^{-1}, respectively. In contrast, the one-sided bow shock has two velocity components in Hα emission. The higher velocity component is located at the apex of the bow shock. Its peak velocity is the same as the main jet component. The $FWHM$ velocity at

the higher velocity component is 15 km s^{-1} less than the typical $FWHM$ velocity of ~45 km s^{-1} in the main jet component.

On the contrary, the lower velocity component is located at the lateral of the bow shock. The peak velocity and $FWHM$ velocity are $V_{\rm LSR} \sim -100$ km s^{-1} and $V_{\rm FWHM} \sim 50$ km s^{-1}, respectively. The peak velocity decreases with Y toward the end of the lateral: ~110 km s^{-1} at SP6, $Y = 34''$, and ~80 km s^{-1} at SP8, $Y = 32''$.

In [NII] as well as Hα emission, the higher velocity component is associated with the main jet component and apex of the bow shock. The peak velocity and $FWHM$ velocity are $V_{\rm LSR} \sim -170$ km s^{-1} and $V_{\rm FWHM} \sim 20$ km s^{-1}, respectively. The $FWHM$ velocity of the [NII] emission is ~10 km s^{-1} lower than that of the Hα emission. The [NII]/Hα flux ratio is ~0.5. In contrast to the Hα emission, the lower velocity component in [NII] emission is not clearly detected. The [NII]/Hα flux ratio is less than 0.05 at the lateral of the bow shock.

2.3.3 Hα filaments

The high resolution Hα image obtained using HST has shown the presence of sharp wisps located away from the jet axis (Heathcote et al. 1996). Such sharp Hα filaments are caused by interaction between the jet and the surrounding medium as well as bow shocks. Any corresponding features in the [SII] 6716 + 6731 Å image are either absent, or much fainter and more diffuse. This suggests that the preshock density is low (of an order of ~100 cm^{-3}) and the cooling zone of the shock is extended (Heathcote et al. 1996).

Figure 2.9 shows the line profiles at the flank of the knot A26. The Hα emission at SP4 shows two velocity components peaking at $V_{\rm LSR} \sim -165$ and ~ -100 km s^{-1}, respectively. Their $FWHM$ velocities are ~30 km s^{-1} and ~70 km s^{-1}, respectively. The velocity at the lower component is ~20 km s^{-1} larger than HH 47B. The brightness of the higher velocity component decreases toward the downstream. In contrast, that of the lower velocity component increases with Y. The Hα emission at SP3 corresponding to the Hα filament has a single velocity component at ~−80 km s^{-1}, which is 20 km s^{-1} lower than the lower velocity component at SP4. The $FWHM$ velocity is ~40 km s^{-1}.

The [NII] emission shows only the high velocity component at SP4. The peak velocity and $FWHM$ velocity in the jet are $V_{\rm LSR} \sim -165$km s^{-1} and $V_{\rm FWHM} \sim 15$ km s^{-1}, respectively. The [NII] emission does not show any velocity components at SP3.

Figure 2.10 shows the line profiles at the flank of the knot A22. This region contains a one-sided bow shock (SP4, SP5 and SP6) and the main jet

component (SP7 and SP8). The main jet component has a single velocity component in Hα emission. The peak velocity and $FWHM$ are $V_{\rm LSR} \sim -165$ km s^{-1} and $V_{\rm FWHM} \sim 40$ km s^{-1}, respectively. The [NII] emission shows a single velocity component as well as the Hα emission. The peak velocity and $FWHM$ velocity in the jet are $V_{\rm LSR} \sim -165$ km s^{-1} and $V_{\rm FWHM} \sim 30$ km s^{-1}, respectively, matching those of the higher velocity component in the Hα emission.

The one-sided bow shock in this region has two velocity components in Hα emission. The higher velocity component is located at the apex of the bow shock. The lower velocity component is located at the lateral of the bow shock. The peak velocity at the higher velocity component is the same as the main jet component, while the $FWHM$ velocity is 10 km s^{-1} less than that of the jet. In [NII] as well as Hα emission, the higher velocity component is associated with the main jet component and apex of the bow shock. The peak velocity and $FWHM$ velocity are $V_{\rm LSR} \sim -160$ km s^{-1} and $V_{\rm FWHM} \sim 20$ km s^{-1}, respectively. The [NII]/Hα flux ratio is 0.3–0.4. The peak velocity and $FWHM$ velocity at the lower velocity component are $V_{\rm LSR} \sim -120$ km s^{-1} and $V_{\rm FWHM} \sim 40$ km s^{-1}, respectively. The peak velocity of the lower velocity component decreases by 20 km s^{-1} toward the upstream from SP5 (a) to SP6 (d) along the Hα filament. In contrast to the Hα emission, the lower velocity component in [NII] emission is not clearly detected. The [NII]/Hα flux ratio is less than 0.1 at the lateral of the bow shock.

Figure 2.11 shows the line profiles at the flank of knot B7, where the jet changes the direction from the east to the north-east. This Hα filament shows a single velocity component in Hα and [NII] emission. The peak velocity and $FWHM$ velocity are $V_{\rm LSR} \sim -170$ km s^{-1} and $V_{\rm FWHM} \sim 50$ km s^{-1}, respectively. The peak velocity increases by 15 km s^{-1} toward the upstream from SP1 (a) to SP2 (c) along the filament. The [NII]/Hα flux ratio is $\sim$0.3 at the Hα filament.

2.4 DISCUSSION

2.4.1 Velocity of the Surrounding Gas

As shown in §3.1, HH 47B (Figure 2.8) and a filament at the flank of knot A22 (Figure 2.10) clearly shows two velocity components. The presence of such two velocity components is well explained by a bow shock (Hartigan, Raymond & Hartmann 1987): the two components are attributed to different regions in a bow shock; (1) the higher velocity component arises from near the bow apex, (2) the lower velocity component arises from its wings.

The observed line profiles are considerably blueshifted compared with those model by Hartigan et al. (1987). In HH 47B (Figure 2.7), the lower velocity component peaks at $\sim$$-$80 km s^{-1}, and the foot point of the line proliles is blueshifted by -30 km s^{-1}. This contrasts to those predicted by the shock models, whose lower velocity component peaks close to the systemic velocity of the ambient gas, with a wing emission extending toward the redshifted side. Such a blueshift have also been observed in HH 47A/D (Morse et al. 1994), HH 34 (Morse et al. 1992; Heathcote & Reipurth 1992), HH 111V (Morse et al. 1993) and HH 1 (Raga et al. 1988). As suggested by these authors, these results are explained if the ambient gas is already moving outward because of the passage of the previous bow shocks.

The preshock velocity of a bow shock is estimated by subtracting the shock velocity from the 3-D velocity of the bow shock. According to the model calculations by Hartigan et al. (1987), the shock velocity V_S is estimated from the measured full width zero intensity (FWZI) of the line profile:

$$Vs = FWZI = MX - MN, \tag{2.1}$$

where MX and MN are the maximum and minimum radial velocities, respectively. For Hα, we should take into account the thermal broadening effect to estimate the shock velocity. Hartigan et al. (1987) thus defined MX and MN as follows:

$$MX = MX0.1 - \frac{SM}{2}, \tag{2.2}$$

$$MN = MN0.1 + \frac{SM}{2}, \tag{2.3}$$

where $MX0.1$ and $MN0.1$ are the observed maximum and minimum radial velocities at 0.1 of the peak flux; SM is the $FWHM$ due to thermal broadening. From (1)-(3) we derive the following equation:

$$Vs = FWZI = MX0.1 - MN0.1 - SM, \tag{2.4}$$

In the case of HH 47B, we derive the shock velocity $V_S \sim 80$ km s^{-1} from $MX0.1 = 190$ km s^{-1}, $MN0.1 = 40$ km s^{-1}, and assumed temperature of 10^5 K, i.e. the typical temperature of Hα emission line regions in shocks (see §4.3). Adopting an inclination angle of 53° (Hartigan et al. 2005), we estimate its 3-D velocity of $\sim$280 km s^{-1} from the radial velocity of $\sim$170 km s^{-1} in the main jet component. The discrepancy between the shock velocity and 3-D velocity is explained if the preshock gas of HH 47B moves

outward by 200 km s^{-1}. In A22, we derive the shock velocity $V_S \sim 55$ km s^{-1} from $MX0.1 = 200$ km s^{-1}, $MN0.1 = 75$ km s^{-1}. We estimate its 3-D velocity of $\sim$280 km s^{-1} from the radial velocity of $\sim$170 km s^{-1} near A22. The discrepancy between the shock velocity and 3-D velocity is explained if the preshock gas of A22 moves outward by 225 km s^{-1}.

The velocity of the preshock gas derived here is comparable to the preshock gas of HH 47A and D, $\sim 40''$ and $\sim 90''$ ahead of HH 47B. Based on Fabry-Perot observations, low-resolution spectroscopy and the same shock model, Morse et al. (1994) derived $\sim$300 km s^{-1} and $\sim$180 km s^{-1} for HH 47A and D, respectively, assuming a viewing angle of 65°. Adopting the same inclination angle as we used for HH 47B, we derive the preshock velocity of HH 47A and D of $\sim$200 km s^{-1} and $\sim$130 km s^{-1}, respectively.

As shown in Figure 2.9, an Hα filament at the flank of A26 also shows two velocity components as well as HH 47B and A22. Performing comparisons with the *HST* image, we conclude that the higher velocity component is associated with the main jet component, not with the apex of the bow shock like HH 47B or A22. The peak velocity and the velocity at the end of the redward wing are -80 and -40 km s^{-1}, respectively, similar to those of the other bow shocks. This suggests that the ambient gas around A26 has a velocity similar to HH 47A/B/D and A22.

Morse et al. (1994) suggested that such outward motion of the ambient gas is due to prompt entrainment. One might think that the motion could also be explained by a wide-angled wind, whose presence is often suggested for young stellar objects (e.g., Shu et al. 2000; Königl et al. 2000; Lee et al. 2000; Davis et al. 2002; Saucedo et al. 2003). However, it is less likely that the HH 46/47 jet is surrounded by such a wide-angled wind. Indeed, simulations suggest that the morphology of a limb-brightened cavity moving outward in the counterflow is explained by interaction with a collimated jet, rather than a wide-angled wind (Raga et al. 2004).

In contrast to the filament at the flank of A26, the filament at the flank of B7 shows a peak velocity of -160 to -170 km s^{-1}, nearly the same as the velocity of the main jet component. In addition, the [NII]/Hα flux ratio in this filament is $\sim$0.3, the same as that in the main jet component (0.3–0.5). Such a ratio is much higher than that in the wings of the bow shocks (HH 47B and A22) and the other Hα filament (A26). We thus conclude that, the Hα filament at B7 results from a shock in the ejecta, not due to interaction between the jet and ambient material. The physical nature indicated by the [NII]/Hα flux ratio is discussed in §4.3 in detail.

2.4.2 Kinematics in Hα Emission and Implications for Entrainment

As described in §1, two entrainment mechanisms have been discussed to date: these are, turbulent entrainment and prompt entrainment. Previous observations provided different conclusions regarding the entrainment in the HH 46/47 system.

Based on the following results, Hartigan et al. (1993) argued the presence of turbulent entrainment with the HH 46/47 system. These author performed Fabry-Perot observations of Hα and [SII] 6716 + 6731 Å associated with the HH 46/47 jet. Their results suggest that the Hα emission occurs preferentially along the edges, where the flow moves significantly slower ($|V_{\rm LSR}| \leq 120$ km s^{-1}) than the jet axis ($V_{\rm LSR} \sim -160$ km s^{-1}). In addition, the boundary regions along the edge of the jet show high Hα/[SII] line ratios, indicative of high shock velocities. These are explained if Hα originates from turbulent mixing layers between the jet and surrounding material (see also Raymond et al. 1994).

In contrast, *HST* observations by Heathcote et al. (1996) do not show the presence of turbulent mixing layers. Their results show that the Hα emission arises from bow shocks, ejecta of the jet, and filamentary structures located at the edge of the jet. Based on these results, Heathcote et al. (1996) conclude that the dominant process that accelerates the surrounding gas is prompt entrainment, where the major bow shock HH 47D and HH 47A, aided by the lesser but more frequent Hα filaments, push material ahead of the jet. Different conclusions between Hartigan et al. (1993) and Heathcote et al. (1996) could be attributed to different aperture of the telescopes, and also pixel sampling. The *HST* observations would be less sensitive to faint and extended emission due to a relatively small aperture of the telescope, and also small pixel sampling. Thus, these might have missed the emission from the turbulent mixing layers observed by Hartigan et al. (1993). Indeed, our spectra show the presence of faint and extended emission, which is not clearly seen in the *HST* image.

However, despite a high sensitivity, our results do not show the presence of separate slow streams as the two sides of the HH 47 jets—the streams shown by Hartigan et al. (1993). Our spectra show that the Hα has a radial velocity of $V_{\rm LSR} \sim -160$ km s^{-1} even at the edge of the jet except for the bow shock regions. In addition, the observed velocity of Hα in the main jet component well matches that of [NII], whose excitation condition is similar to [SII], which originates from regions closer to the jet axis (see Hartigan et al. 1993). These suggest that Hα originates from the ejecta of the jet similar to [SII] and [NII], but not from turbulent mixing layers as was argued

by Hartigan et al. (1993) and Raymond et al. (1994). The low velocity strands seen in their image could be attributed to the relatively low spectral resolution of their Fabry-Perot observations ($\sim$30 km s^{-1}).

2.4.3 [NII]/Hα Flux Ratios and Implications for Pre-Ionization

The angular resolution of our observations ($\sim 0\farcs7$) does not seem to be sufficient to resolve the entire cooling zone of the shock predicted by models (e.g., Bacciotti & Eislöffel 1999) and observed using the *HST* (e.g., Heathcote et al. 1996). Indeed, the distributions of Hα and [NII] well match each other in the PV diagrams. Their peak positions differ to each other by $\sim 1''$ at some positions; however, the direction of the displacement is not systematic as predicted for the shock cooling zones. Such displacement could thus be attributed to multiple shocks with different shock conditions rather than an inner structure of the shock cooling zones.

Instead, our angular resolution allows for investigating the shock conditions by performing comparisons between the observed [NII]]/Hα ratio at each position and that predicted by shock models. One might think that optical emission lines in the main jet component are not excited by shock. However, the following results strongly suggest that these lines are shock excited. As mentioned in §3.2 and §3.3, the *FWHM* velocity of the Hα emission in the main jet component is $\sim$10 km s^{-1} larger than that of the [NII] emission. The discrepancy is attributed to the thermal broadening, which depends on the mass of the atoms/ions. Based on the results described above, we derived the temperature of the Hα emission line regions of $\sim 10^5$ K. Such a temperature agrees with the shock heating scenario in the jet (Raymond 1979; Raga & Binette 1991).

The observed [NII]/Hα flux ratio ranges from 0.2 to 0.5 in the main jet component (see Figure 2.6). It is 0.5 at the apex of the bow shock, and less than 0.1 at the lateral of the bow shock (§3.2). It is $\sim$0.3 at the Hα filament (§3.3). The ratios in some regions are markedly higher than the typical ratio suggested by previous observations ($\sim$0.2, Morse et al. 1994). A possible interpretation is that the preshock gas in these regions is significantly ionized, as described below in detail.

Figure 2.12 shows the [NII]/Hα flux ratio predicted by Morse et al. (1994) and Hartigan et al. (1987) for different shock conditions. The figure shows that, if the shock velocity V_S is less than 100 km s^{-1}, the [NII]/Hα flux ratio clearly depends on the ionization of the preshock gas. These are, $\sim$0.6 if the preshock gas is fully ionized; $\leq$0.2 if it is neutral. Such a tendency may

result from enhancement of N^+ via the following charge exchange reaction (e.g., Osterbrock 1989; Bacciotti & Eislöffel 1999):-

$$N^0 + H^+ \rightleftharpoons N^+ + H^0, \tag{2.5}$$

At $V_S \geq 100$ km s^{-1} the UV radiation from the postshock regions ionizes the preshock gas, hence the [NII]/Hα flux ratio is high (>0.3) independent of the initial ionization condition. However, this is not the case for the HH 46/47 jet: the absence of the [OIII] 5007 Å emission suggests that the shock velocity is less than 90 km s^{-1} (Morse et al. 1994). Some authors pointed out that a flux ratio of a forbidden line to Hα, such as [NII]/Hα, may not reliably indicate the ionization fraction due to different critical density and temperature, and also excitation mechanism (e.g., Bacciotti & Eislöffel 1999).

Performing comparisons with Figure 2.12, we suggest that the main jet component is considerably ionized compared with the previous estimates (< 0.2 —Hartigan et al. 1994; Bacciotti & Eislöffel 1999). Based on their optical spectroscopy, Bacciotti & Eislöffel (1999) estimated the jet has only one-third of the total momentum of the molecular outflow. Adopting a larger ionization fraction, the momentum of the jet should be even lower, thus one might think that the molecular outflow cannot be driven solely by an optical jet. However, we emphasize that the optical emission lines do not presumably provide the entire momentum of the jet because these are associated with shock, not from the entire ejecta (see, e.g., Hartigan et al. 2000). Thus, although the momentum of the jet discussed above is much smaller than that of the molecular outflow, this does not reject the jet-driven scenario of the molecular outflow.

The [NII]/Hα flux ratio in the Hα filament is significantly lower than that in the main jet component, indicating that the ambient gas surrounding the jet is almost neutral. As shown in §3.2 and §3.3, the [NII]/Hα flux ratio is high at the apex of the bow shocks, while it is low at the lateral. A possible interpretation is that the preshock gas is partially ionized at the apex, while the ambient gas surrounding the jet is almost neutral at the lateral.

2.4.4 Nature of HH 46-NW

As described in §3.1, HH 46 has two velocity components at $V_{LSR} \sim -210$ km s^{-1} and -150 km s^{-1} in Hα emission. Our spectra show that the position of the lower velocity component, HH 46-NW, coincides with a bright Hα filamentary structure revealed by Heathcote et al. (1996) using the *HST*. These authors show that structure is located at the position where the jet

(HH 46-1/2) changes the tangential orientation by $\sim$15°. In contrast to the other part of the HH 46/47 system, this Hα filament does not clearly show the proper motion (Hartigan et al. 2005). Hartigan et al. (2005) argue that the structure is a quasi-stationary deflection shock, where the jet currently collides with stationary material on northern edges of the cavity.

Our observations show that [NII]/Hα flux ratio in HH 46-NW is significantly lower ($\sim$0.3) than the main jet component HH 46-1/2 ($\sim$0.6). As described in §4.2, low [NII]/Hα flux ratios are also observed in the other Hα filaments and bow shocks. Thus, our results agree with the scenario that the HH 46-NW Hα filament is also due to interaction between the jet and surrounding material. The velocity of the HH 46-NW filament is $\sim$40 km s^{-1} larger than the other Hα filaments and bow shocks. This would be explained if the ambient gas moves outwards by $\sim$70 km s^{-1} larger than the ambient material downstream (cf. §4.1). The origin of such a large velocity is, however, not clear.

2.5 SUMMARY

We have presented slit-scan observations of the Hα and [NII] 6583 Å emission line toward the HH 46/47 jet with the Subaru Telescope. We have obtained main results as follows:

(1) The Hα emission shows the main jet component ($V_{\rm LSR} \sim -160$ km s^{-1}) and distinct lower velocity components ($|V_{\rm LSR}| \leq 120$ km s^{-1}). The lower velocity components are associated with one-sided bow shock, and also the Hα filaments previously identified using *HST*. In contrast, the [NII] emission is primarily associated with the main jet component and it is much fainter or absent in the lower velocity components. The observed velocity of [NII] in the main jet component well matches that of Hα. The $FWHM$ velocity of the Hα emission in the main jet components is 30-50 km s^{-1}, 10 km s^{-1} larger than that of the [NII] emission. The different $FWHM$ velocity between Hα and [NII] agrees with the shock heating scenario in the jet. The observed [NII]/Hα flux ratio ranges from 0.2 to 0.5 in the main jet component. It is 0.5 at the apex of the bow shock, and less than 0.1 at the lateral of the bow shock. It is $\sim$ 0.3 at the Hα filament.

(2) HH 47B and Hα filaments at the flank of knot A22 show two velocity components in Hα. The higher velocity component show $V_{\rm LSR} = -170$ km s^{-1} at the apex of the bow shock, while the lower velocity component show $V_{\rm LSR} = -100$ km s^{-1} at the lateral of the bow shock. The shock velocity derived from the line profiles is 60–80 km s^{-1}, markedly smaller than the 3-D velocity ($\sim$280 km s^{-1}). The discrepancy between the shock veloc-

ity and 3-D velocity is explained if the preshock gas moves outward by 200 km s^{-1} and 225 km s^{-1} for HH 47B and A22, respectively. The velocity of the preshock gas derived here is comparable to the preshock gas of HH 47A and D, $\sim 40''$ and $\sim 90''$ ahead of HH 47B.

The Hα filament at the flank of A26 also shows two velocity components as well as HH 47B and A22. However, the higher velocity component is associated with the main jet component, not with the apex of the bow shock like HH 47B or A22. The peak velocity and the velocity at the end of the redward wing are similar to those of the other bow shocks, indicating the ambient gas around A26 has a velocity similar to HH 47 A/B/D and A22. In contrast to the other Hα filament and bow shocks, the filament at the flank of B7 shows the same velocity of the main jet component. The [NII]/Hα flux ratio in the filament is also the same as that in the main jet component. We thus conclude that the Hα filament at B7 originates from a shock in the ejecta, not due to the interaction between the jet and ambient material.

(3) The Hα emission shows a uniform radial velocity of $V_{\rm LSR} = -160$ km s^{-1} in the main jet component (Δ V = 10 km s^{-1}). In contrast to the previous observations, our slit-scan observations with a high spectral resolution did not show the presence of slow Hα components ($|V_{\rm LSR}| \leq 120$ km s^{-1}) along the edges of the jet. Our results indicate that both Hα and [NII] originate from the ejecta of the jet, not from turbulent mixing layers. This rejects the presence of turbulent entrainment. Thus, we conclude that the outward motion of the ambient gas described in §2 is due to prompt entrainment.

(4) Our slit-scan observations revealed that the [NII]/Hα flux ratios in some regions of the main jet component, at the apex of the bow shocks (HH 47B and A22) and other Hα filament (A26) are remarkably higher than the typical ratio suggested by previous observations ([NII]/H$\alpha \sim 0.2$), while it is low at the lateral. By comparing observed values with predicted ones, a possible interpretation is that the preshock gas is partially ionized in the main jet component, and also at the apices of bow shocks and Hα filaments (ionization fraction ≥ 0.2), while the ambient gas surrounding the jet is almost neutral.

(5) HH 46 has two velocity components at $V_{\rm LSR} = -210$ km s^{-1} and $V_{\rm LSR} = -150$ km s^{-1}. The lower component, HH 46-NW, coincides with a bright Hα filamentary structure previously identified using *HST*. The [NII]/Hα flux ratio is significantly lower ($\sim$0.3) than the main jet component HH 46-1/2 ($\sim$0.6). This suggests that the Hα filament is due to interaction between the jet and surrounding material as well as the other Hα filaments and the bow shocks. The velocity of the HH 46-NW filament is ~ 40 km s^{-1} larger than the other Hα filament and the bow shocks. This would be explained if the ambient gas moves outwards by ~ 70 km s^{-1} larger than the

ambient material downstream.

Acknowlegements

We acknowledge the anonymous referee for helpful comments. We are grateful for Dr. Hartigan to provide us his *HST* WFPC2 F656N image. We also thank the staff at the Subaru Telescope for their excellent support. This research has made use of the NASA's Astrophysics Data System Abstract Service.

Reference

Bacciotti, F., Chiuderi, C., & Oliva, E. 1995, A&A, 296, 185
Bacciotti, F., & Eislöffel, J. 1999, A&A, 342, 717
Bachiller, R., Terebey, S., Jarrett, T., Martin-Pintado, J., Beichman, C. A., & van Buren, D. 1994, ApJ, 437, 296
Bachiller, R. 1996, ARA&A, 34, 111
Canto, J., & Raga, A. C. 1991, ApJ, 372, 646
Chernin, L. M., & Masson, C. R. 1995, ApJ, 455, 182
Davis, C. J., & Eislöffel, J. 1995, A&A, 300, 851
Davis, C. J., Eislöffel, J., Ray, T. P., & Jenness, T. 1997, A&A, 324, 1013
Davis, C. J., Stern, L., Ray, T. P., & Chrysostomou, A. 2002, A&A, 382, 1021
de Vries, C. P., Brand, J., Habing, H. J., Israel, F. P., de Graauw, T., Wouterloot, J. G. A., & van de Stadt, H. 1984, A&AS, 56, 333
Eislöffel, J., & Mundt, R. 1994, A&A, 284, 530
Eislöffel, J., Davis, C. J., Ray, T. P., & Mundt, R. 1994, ApJ, 422, L91
Graham, J. A., & Heyer, M. H. 1989, PASP, 101, 573
Gueth, F., & Guilloteau, S. 1999, A&A, 343, 571
Hartigan, P., Raymond, J., & Hartmann, L. 1987, ApJ, 316, 323
Hartigan, P., Raymond, J., & Meaburn, J. 1990, ApJ, 362, 624
Hartigan, P., Morse, J. A., Heathcote, S., & Cecil, G. 1993, ApJ, 414, L121
Hartigan, P., Morse, J. A., & Raymond, J. 1994, ApJ, 436, 125
Hartigan, P., Bally, J., Reipurth, B., & Morse, J. A. 2000, Protostars and Planets IV, 841
Hartigan, P., Heathcote, S., Morse, J. A., Reipurth, B., & Bally, J. 2005, AJ, 130, 2197
Heathcote, S., & Reipurth, B. 1992, AJ, 104, 2193
Heathcote, S., Morse, J. A., Hartigan, P., Reipurth, B., Schwartz, R. D., Bally, J., & Stone, J. M. 1996, AJ, 112, 1141
Königl, A., & Pudritz, R. E. 2000, Protostars and Planets IV, 759
Kuiper, T. B. H., Peters, W. L., Forster, J. R., Gardner, F. F., & Whiteoak, J. B. 1987, PASP, 99, 107
Lee, C.-F., Mundy, L. G., Reipurth, B., Ostriker, E. C., & Stone, J. M. 2000, ApJ, 542, 925
Masson, C. R., & Chernin, L. M. 1993, ApJ, 414, 230
Meaburn, J., & Dyson, J. E. 1987, MNRAS, 225, 863
Mitchell, G. F., Hasegawa, T. I., Dent, W. R. F., & Matthews, H. E. 1994, ApJ, 436, L177
Morse, J. A., Hartigan, P., Cecil, G., Raymond, J. C., & Heathcote, S. 1992, ApJ, 399, 231

Morse, J. A., Heathcote, S., Cecil, G., Hartigan, P., & Raymond, J. C. 1993, ApJ, 410, 764
Morse, J. A., Hartigan, P., Heathcote, S., Raymond, J. C., & Cecil, G. 1994, ApJ, 425, 738
Mundt, R., & Fried, J. W. 1983, ApJ, 274, L83
Mundt, R., Brugel, E. W., & Buehrke, T. 1987, ApJ, 319, 275
Osterbrock, D. E. 1989, Research supported by the University of California, John Simon Guggenheim Memorial Foundation, University of Minnesota, et al. Mill Valley, CA, University Science Books, 1989, 422 p.,
Raga, A. C., Mateo, M., Bohm, K.-H., & Solf, J. 1988, AJ, 95, 1783
Raga, A. C., Binette, L., Canto, J., & Calvet, N. 1990, ApJ, 364, 601
Raga, A. C. 1991, AJ, 101, 1472
Raga, A. C., & Binette, L. 1991, Revista Mexicana de Astronomia y Astrofisica, 22, 265
Raga, A., & Cabrit, S. 1993, A&A, 278, 267
Raga, A. C., Noriega-Crespo, A., González, R. F., & Velázquez, P. F. 2004, ApJS, 154, 346
Raymond, J. C. 1979, ApJS, 39, 1
Raymond, J. C., Morse, J. A., Hartigan, P., Curiel, S., & Heathcote, S. 1994, ApJ, 434, 232
Reipurth, B., & Heathcote, S. 1991, A&A, 246, 511
Reipurth, B., Yu, K. C., Heathcote, S., Bally, J., & Rodríguez, L. F. 2000, AJ, 120, 1449
Richer, J. S., Shepherd, D. S., Cabrit, S., Bachiller, R., & Churchwell, E. 2000, Protostars and Planets IV, 867
Riera, A., López, R., Raga, A. C., Anglada, G., & Estalella, R. 2001, Revista Mexicana de Astronomia y Astrofisica, 37, 147
Saucedo, J., Calvet, N., Hartmann, L., & Raymond, J. 2003, ApJ, 591, 275
Schwartz, R. D. 1977, ApJ, 212, L25
Shu, F. H., Ruden, S. P., Lada, C. J., & Lizano, S. 1991, ApJ, 370, L31
Stahler, S. W. 1994, ApJ, 422, 616
Woitas, J., Eislöffel, J., Mundt, R., & Ray, T. P. 2002, ApJ, 564, 834

slit number	1	2	3	4	5	6	7	8
offset	0	$0''.8$	$1''.7$	$3''.0$	$3''.6$	$4''.8$	$5''.9$	$6''.8$

Table 2.1: Offset of slit positions for HH 46/47

Knot (id)	Slit (number)	Y $''$	V_{peak} (km s^{-1})	ΔV (km s^{-1})	Remark
	1	1.4	−202	97	
	1	19.3	−153	49	
	1	23.0	−158	45	
	1	26.2	−115	42	
HH46-1	2	3.3	−224	55	
	2	19.5	−156	52	
B7	2	22.8	−158	44	
	2	26.6	−174, −128	28, 43	two components
	2	35.6	−155	32	
HH46-1	3	3.6	−221	51	
B7′	3	23.2	−163	47	
	3	27.4	−135	46	blue wing
B1	3	36.7	−167,−112	39, 50	two components
	3	41.3	−80	41	
HH46-2	4	5.3	−201, −146	52, 55	two components
HH46-NW	4	5.8	−199, −149	48, 54	two components
B8	4	20.7	−162	47	
B6	4	23.9	−158	52	
HH47B	4	34.5	−171	28	redshifted wing
A26	4	40.4	−168, −111	27, 67	two components
	4	41.5	−168, −110	28, 65	two components
HH46-NW	5	5.6	−157	66	
B8	5	20.7	−162	46	
B5	5	26.3	−161	43	
HH47B	5	34.2	−172	28	redshifted wing
A26	5	40.8	−168, −125	28, 57	two components
	5	41.8	−166, −121	33, 51	two components
HH46-NW	6	5.3	−237, −158	76, 64	two components
B9	6	19.1	−155	43	
B4	6	28.1	−156	31	red skewed
HH47B	6	34.1	−171, −113	31, 52	two components
A25	6	41.3	−164	32	redshifted wing
B10	7	16.8	−146	48	
	7	21.4	−160, −71	42, 38	two components
HH47B	7	34.2	−172, −105	33, 56	two components
A22	7	46.6	−170	33	red skewed
	8	15.7	−146	53	
HH47B	8	33.1	−77	45	
A23	8	43.6	−169	44	redshifted wing
A20	8	47.9	−174	31	redshifted wing
A18	8	52.2	−173	36	redshifted wing
A15	8	57.6	−181	31	redshifted wing

Table 2.2: Line profile parameters of knots in Hα

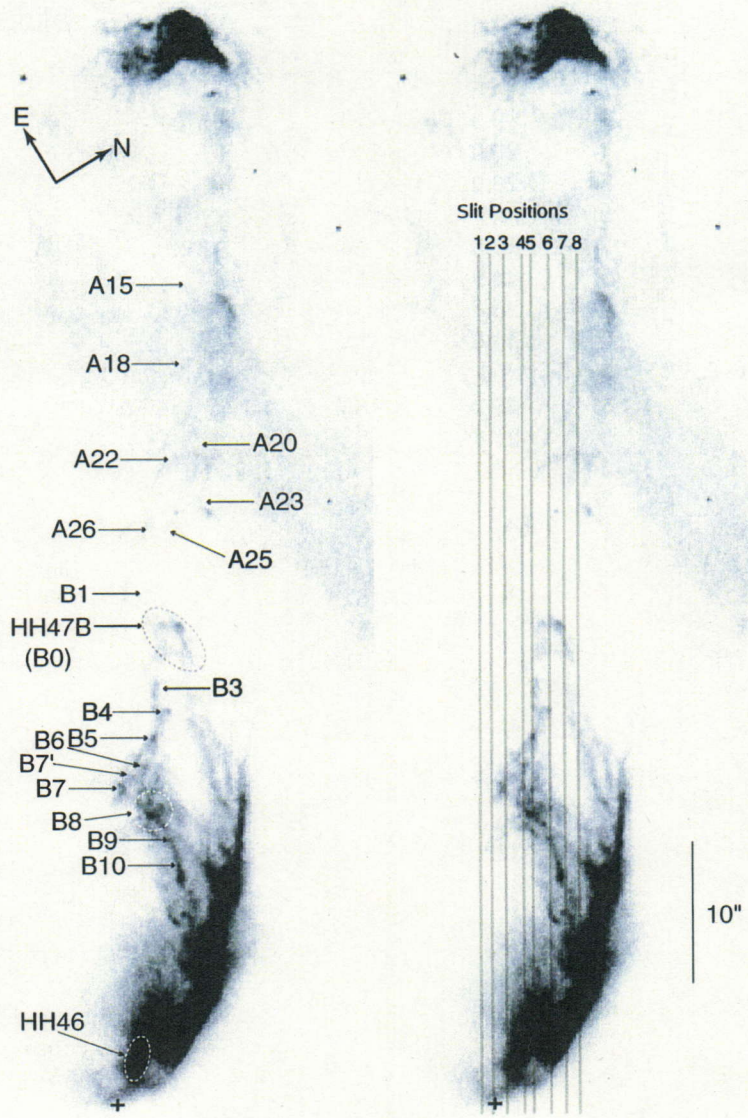

Figure 2.1: Identified knots and slit positions on an *HST* image of Hα emission toward the HH 46/47 jet. We use the nomenclature of Eislöffel & Mundt (1994) for some HH knots. The image was obtained in 1999 by WFPC2 (Hartigan, private communication). The cross designates the position of HH 46 IRS (α_{2000}= $08^h25^m43^s.91$, δ_{2000}= $-51°00'35''.6$, Hartigan et al. 2005). The slit length and width are $60''$ and $1''$, respectively. The position angle of the slit is 58.64°. The north and east are shown by arrows.

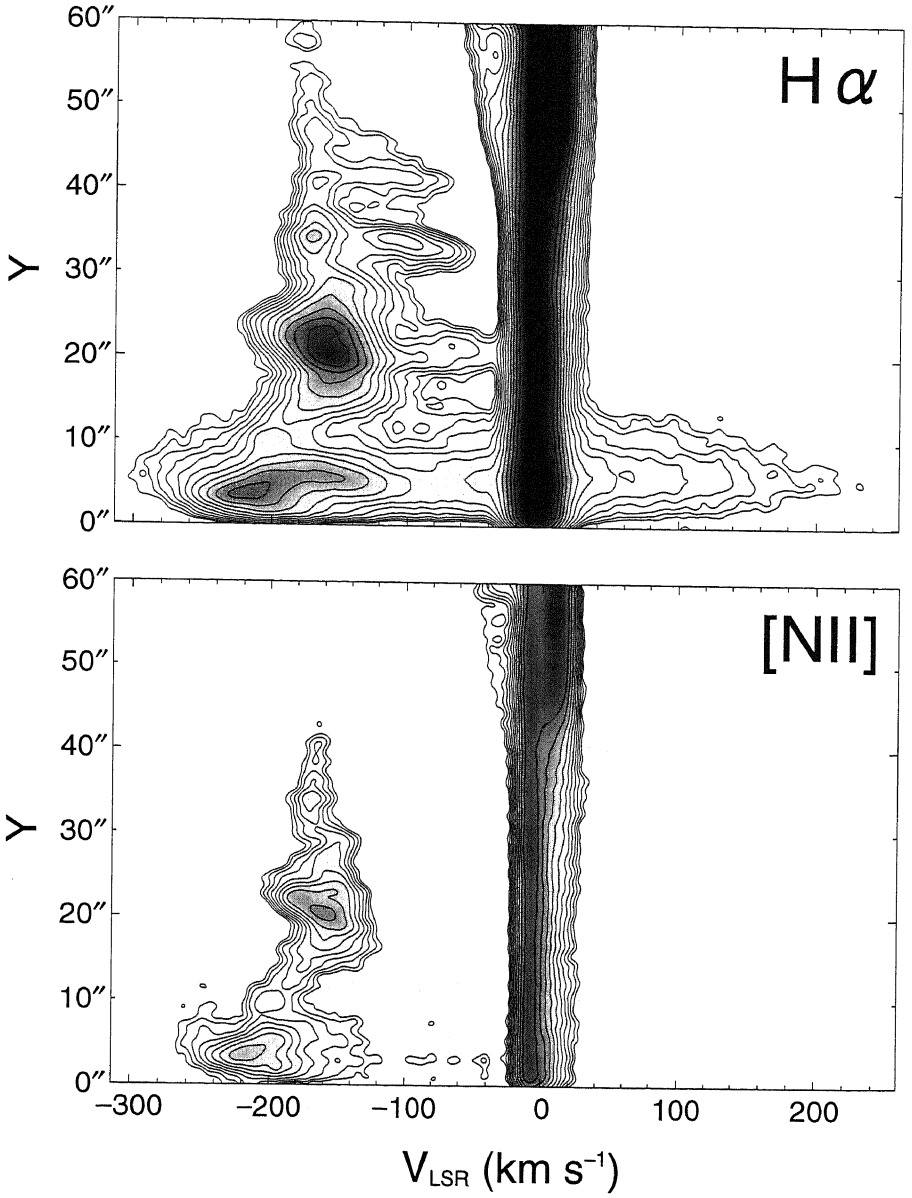

Figure 2.2: Position-velocity diagrams of the Hα (upper panel) and [NII] (lower panel) emission summed over the eight slit positions. The velocity is shown with respect to the local standard of rest (LSR). Y is the projected angular distance measured along the jet. The PVDs are smoothed by a Gaussian with $\sigma_G = 4$ pixel. Contours are indicated from 5 σ to 160 σ for Hα and from 7 σ to 105 σ for [NII] with equal intervals in a logarithmic scale.

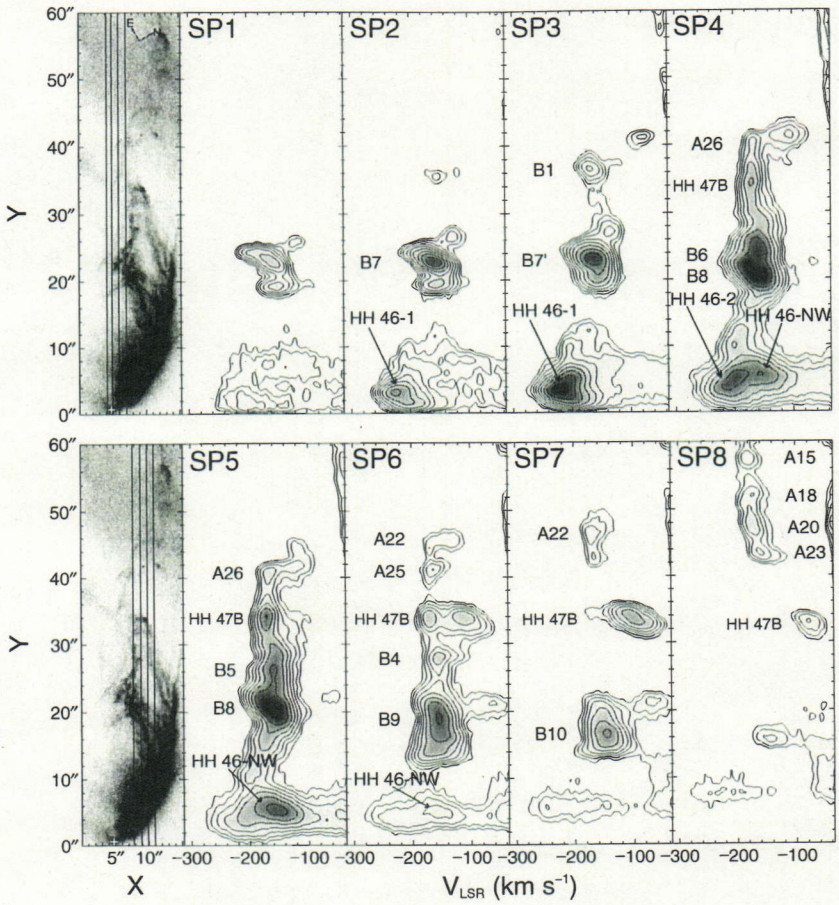

Figure 2.3: Hα image taken with *HST* and eight position-velocity diagrams obtained from our HDS observations toward the HH 46/47 jet. We use the nomenclature of Eislöffel & Mundt (1994) for some HH knots. The jet direction is up in each panel. Slit position 1 (SP1) to position 8 (SP8) are from the southeast to the northwest across the jet in the left image (thick vertical lines). Y is the projected angular distance measured along the jet. The HH 46 IRS is indicated by the cross and is located at $Y \sim 0\farcs7$. The north and east are shown by arrows. The PVDs are smoothed by a Gaussian with $\sigma_G = 4{\times}4$ pixel (3.4 km s^{-1} $\times$ $0\farcs6$). Contours are indicated from 10 σ to 40σ, from 10 σ to 130 σ, from 10 σ to 200 σ, from 10 σ to 210 σ, from 10 σ to 210 σ, from 10 σ to 110 σ, from 10 σ to 110 σ, from 10 σ to 40 σ with equal intervals in a logarithmic scale for SP1 to SP8, respectively. The *HST* image and the PVDs were obtained in different years (1999 and 2002, respectively).

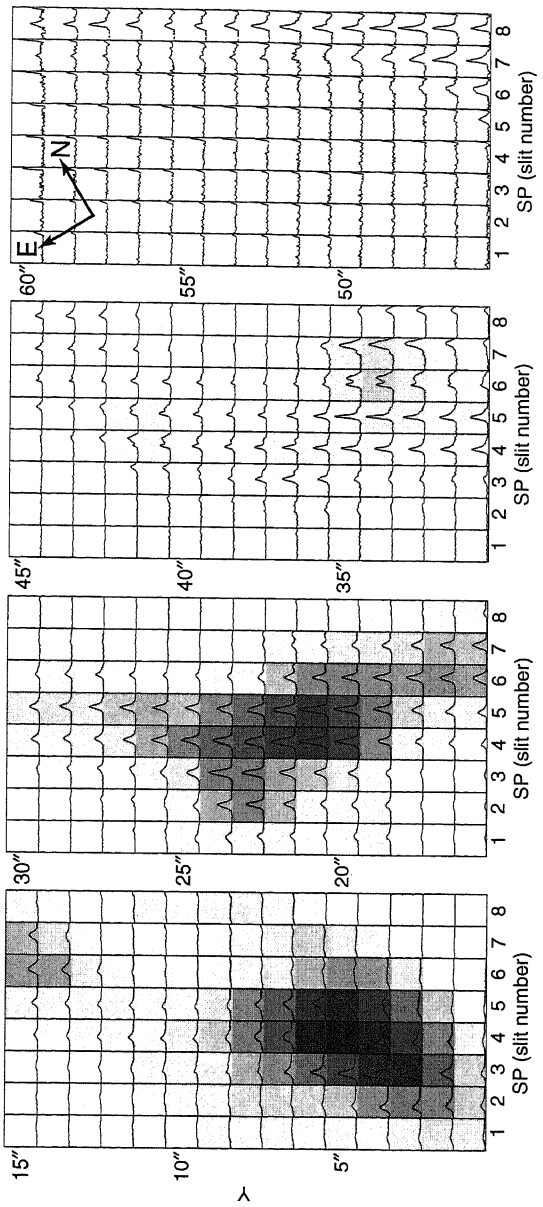

Figure 2.4: Hα profile maps for the Hα emission. They consist of four regions ($0'' \leq Y \leq 15''$, $16'' \leq Y \leq 30''$,$31'' \leq Y \leq 45''$ and $46'' \leq Y \leq 60''$, respectively). Each profile is shown between $V_{\rm LSR} = -313$ km s^{-1} and -37 km s^{-1}. Each bin covers an area of $1'' \times 1''$. The horizontal axis is the slit number and the vertical axis is the projected angular distance. The grayscale shows the integrated intensity over the above velocity range. The north and east are shown by arrows.

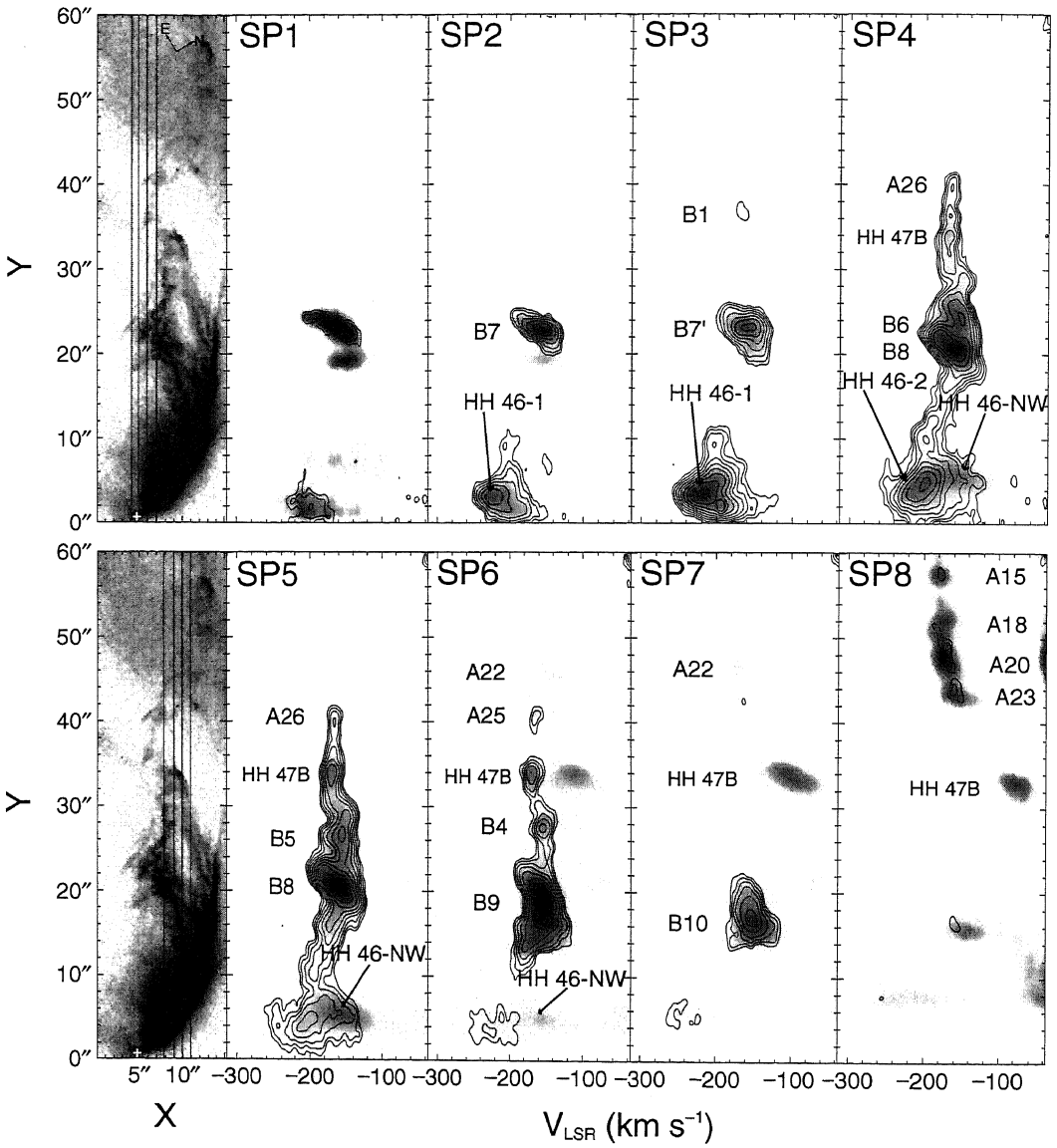

Figure 2.5: Same as Figure 2.3, but the contours show the [NII] 6583 Å emission. The gray scale shows the Hα emission in the Figure 2.3. The contours are indicated from 6 σ to 60 σ with equal intervals in a logarithmic scale.

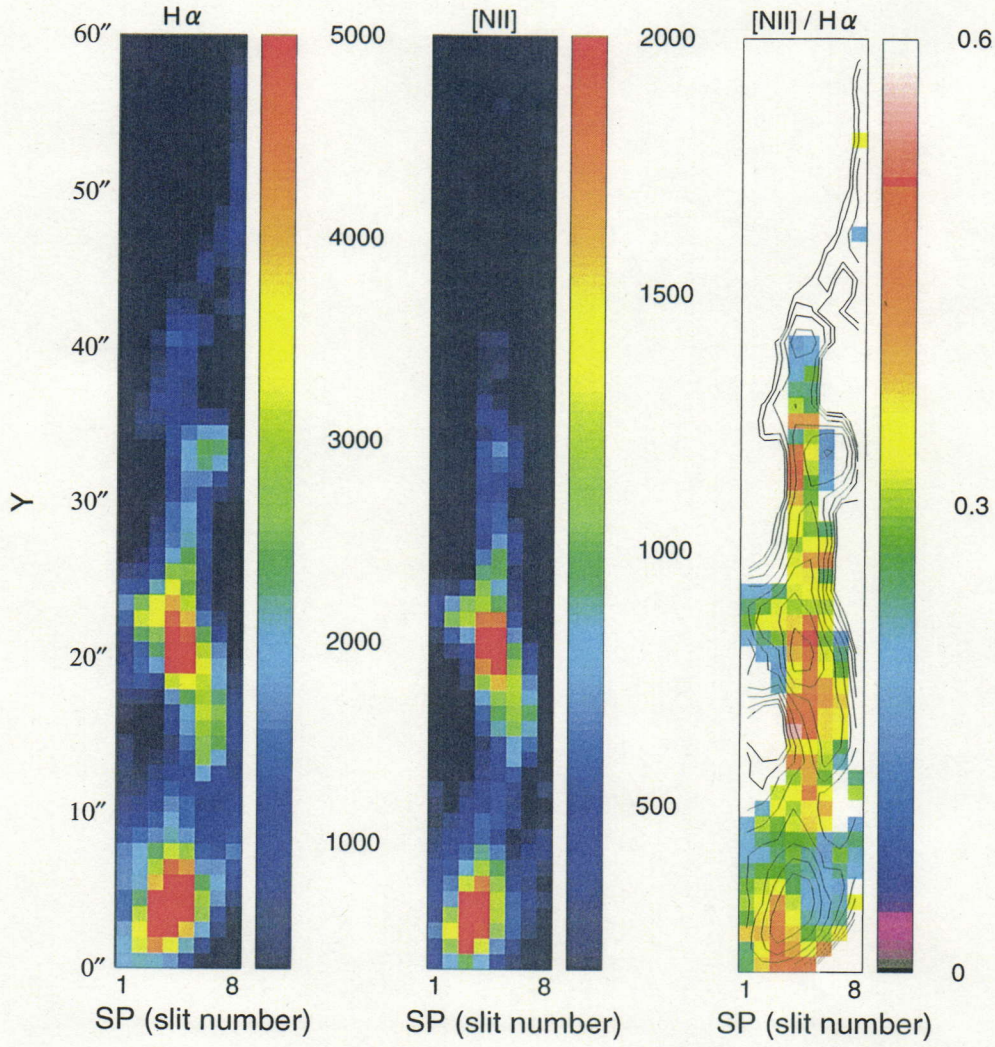

Figure 2.6: The intensity distribution of Hα (left) and [NII] 6583 Å (middle), and the [NII]/Hα flux ratio (right). The intensity for each grid in obtained by integrating the line profile from -313 km s^{-1} to -37 km s^{-1}. The horizontal axis is the slit number and the vertical axis is the projected angular distance. The right side bars for the left and middle figures are shown in arbitrary unit. The [NII]/Hα flux ratio in the right figure is shown for the regions with S/N $\geq$ 3. Contour is indicated with equal intervals in a logarithmic scale for intensity of Hα.

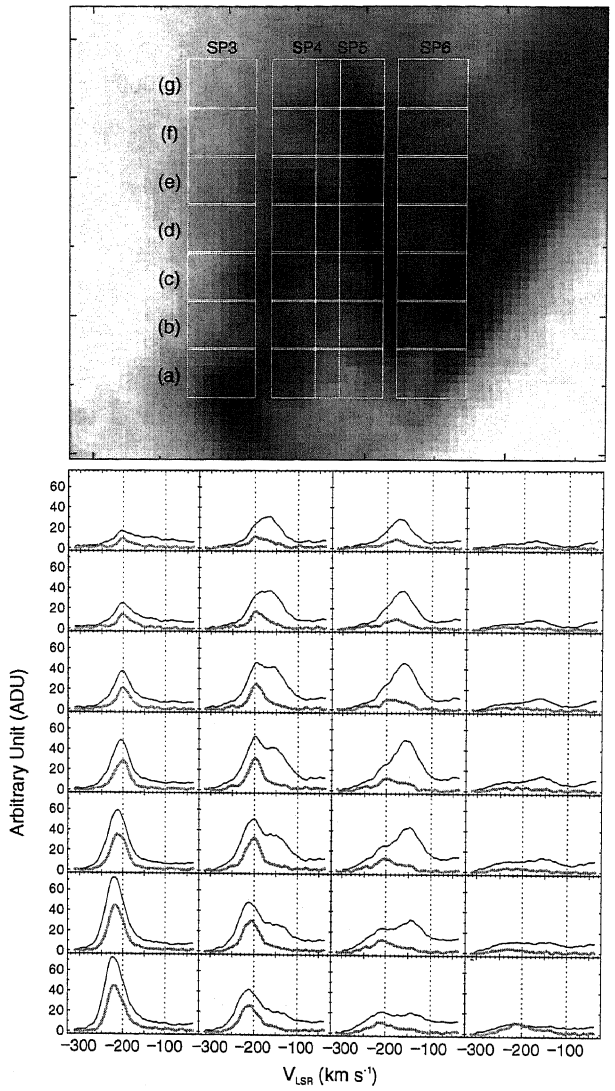

Figure 2.7: Line profiles of the Hα (black) and [NII] 6583 Å (gray) in the HH 46 region. Hα image obtained using *HST* (Hartigan, private communication) is also shown at the top. The white rectangles in the *HST* image show the regions where we obtain the line profiles. The horizontal and vertical scale of each rectangle corresponds to the slit width and seeing, respectively. The positions (a)–(g) correspond to $Y = 4\farcs2$, $4\farcs9$, $5\farcs6$, $6\farcs3$, $7\farcs0$, $7\farcs7$ and $8\farcs4$, respectively.

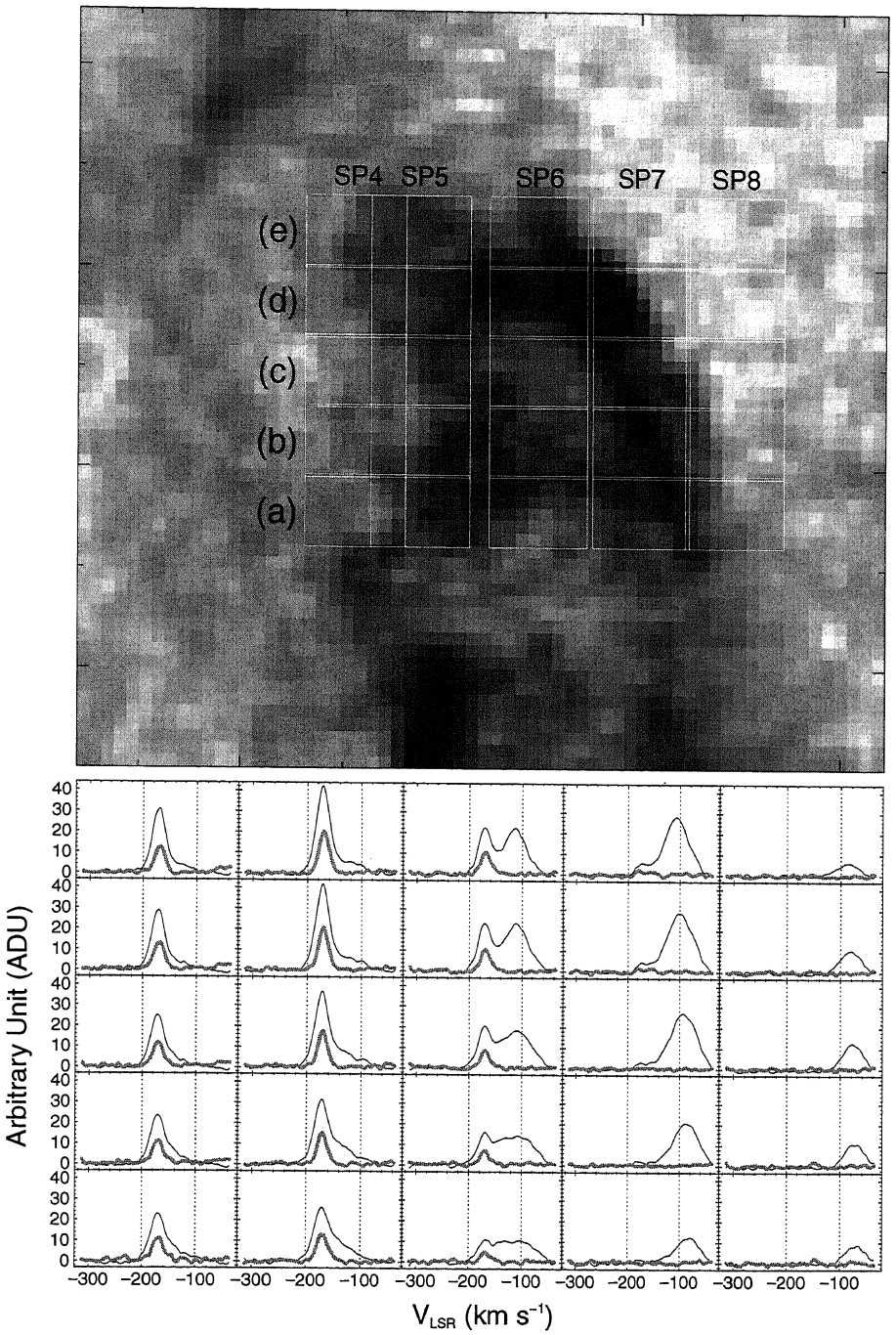

Figure 2.8: Same as Figure 2.7, but in the HH 47B. The positions (a)–(e) correspond to $Y = 32\overset{''}{.}6$, $33\overset{''}{.}3$, $34\overset{''}{.}0$, $34\overset{''}{.}7$ and $35\overset{''}{.}4$, respectively.

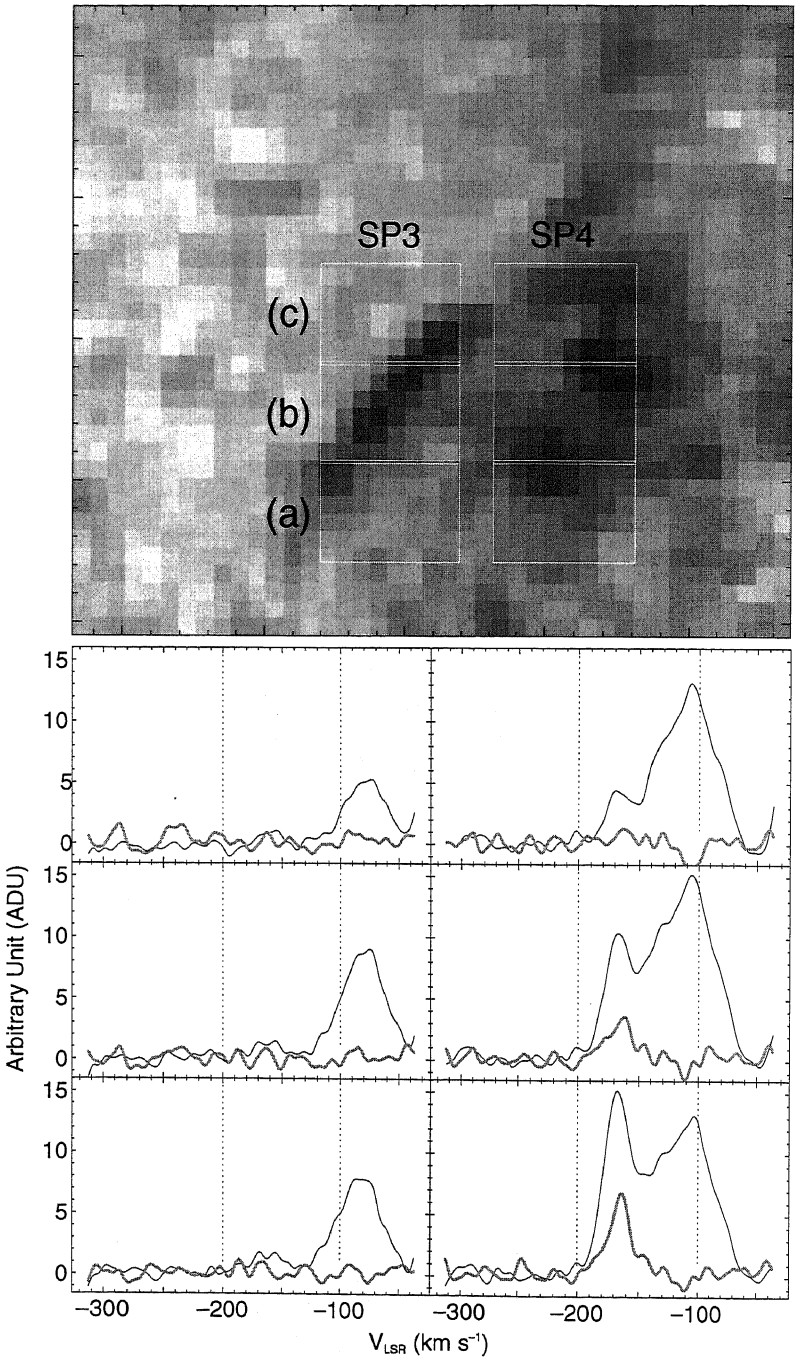

Figure 2.9: Same as Figure 2.7, but in the knot A26. The positions (a)–(c) correspond to $Y = 40\overset{''}{.}9$, $41\overset{''}{.}5$ and $42\overset{''}{.}2$, respectively.

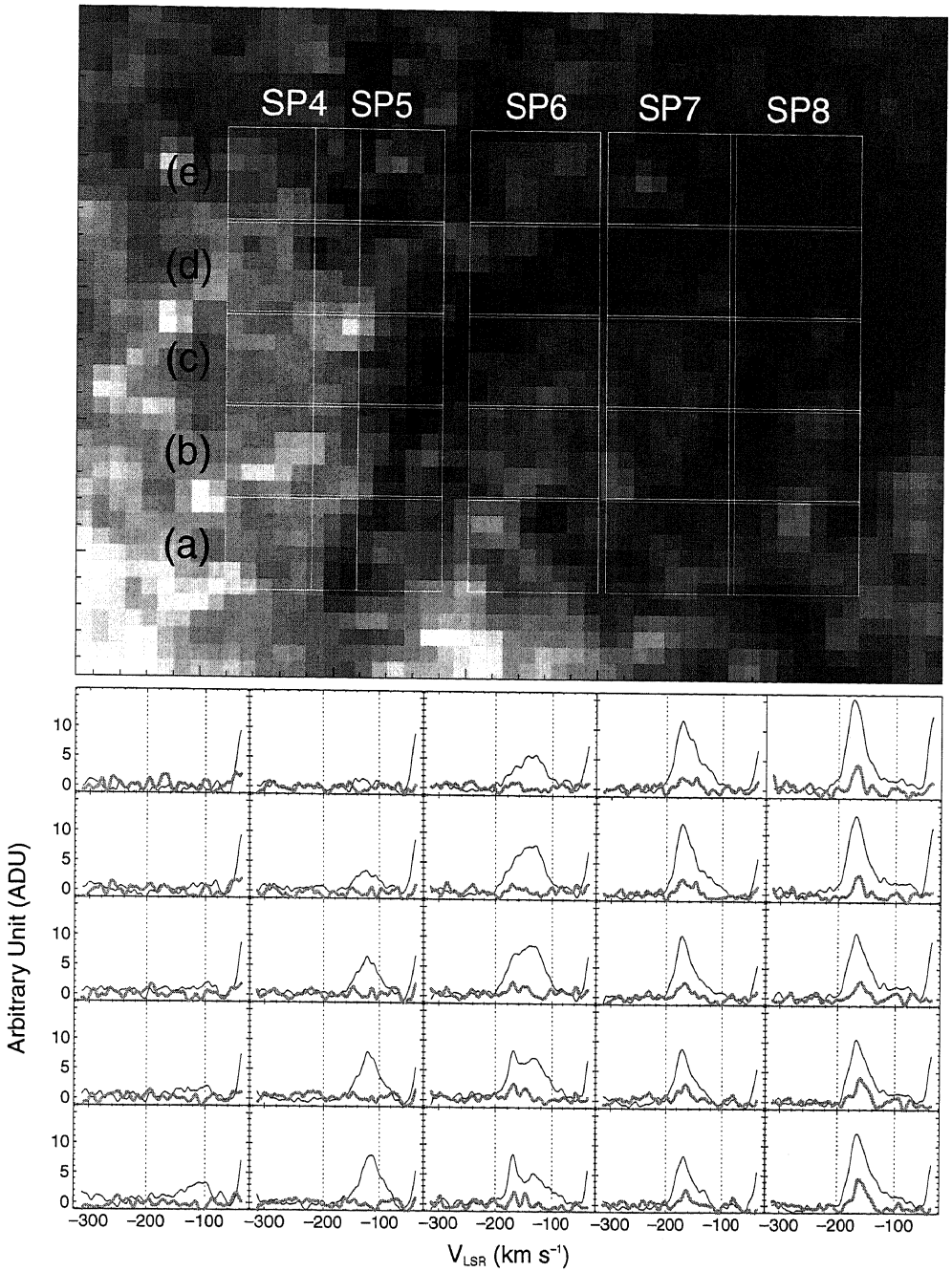

Figure 2.10: Same as Figure 2.5, but in the knot A22. The positions (a)–(e) correspond to $Y = 44\overset{''}{.}3$, $45\overset{''}{.}0$, $45\overset{''}{.}7$, $46\overset{''}{.}4$ and $47\overset{''}{.}0$, respectively.

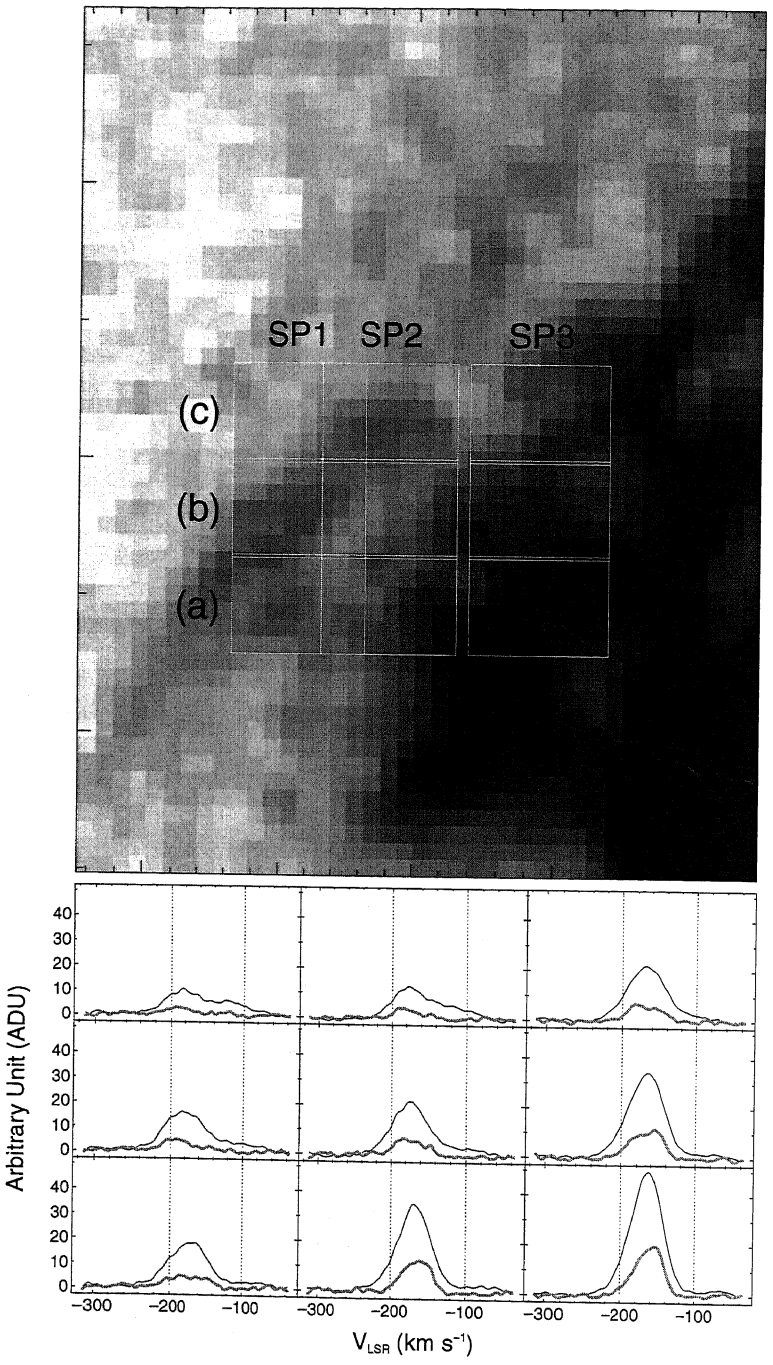

Figure 2.11: Same as Figure 2.5, but in the knot B7. The positions (a)–(c) correspond to $Y = 23\overset{''}{.}9$, $24\overset{''}{.}6$ and $25\overset{''}{.}3$, respectively.

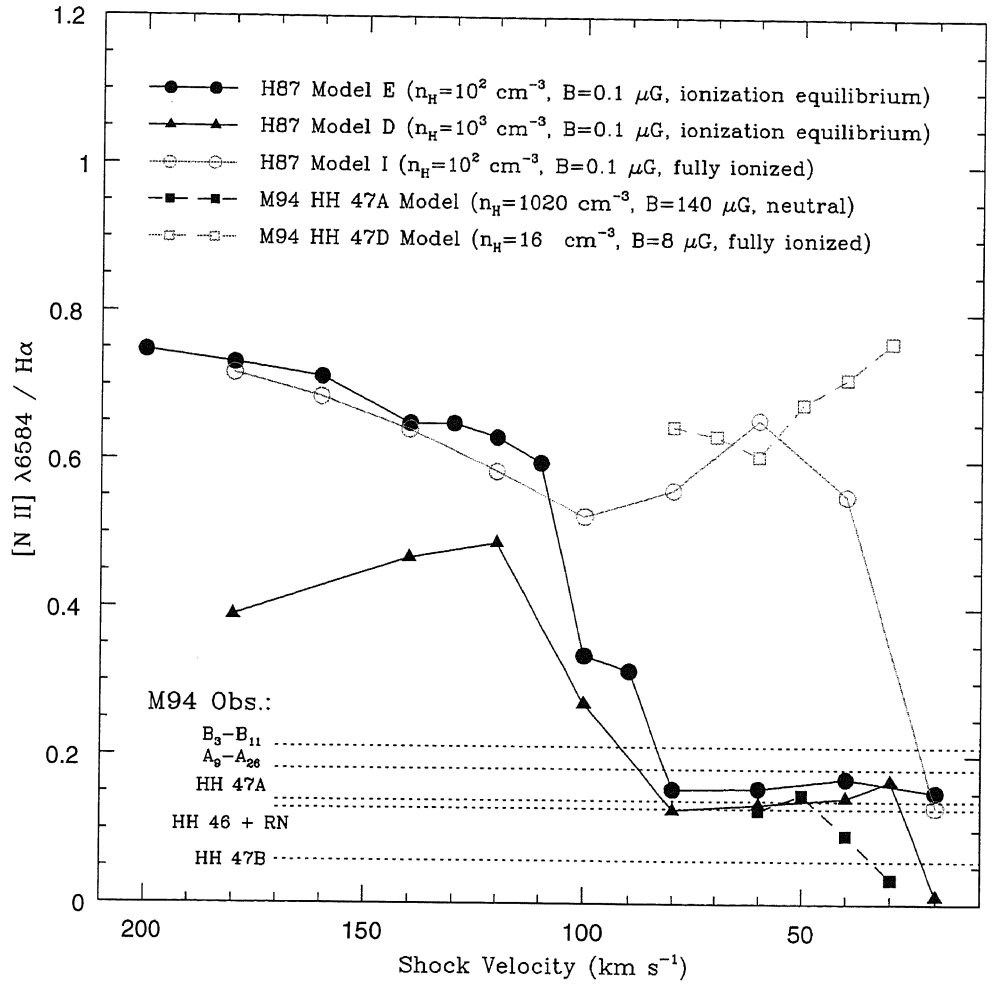

Figure 2.12: Modeled and observed [NII] 6583 Å/Hα flux ratios shown by Hartigan et al. (1987) and Morse et al. (1994). The solid and dashed lines show modeled ratios. The black dots and lines show modeled ratios in case that the ambient gas is neutral, or ionized by the radiation from the shock. The gray dots and lines indicate modeled ratios in case that the ambient gas is fully ionized. The dotted lines at the bottom indicate the observed ratios in the HH 46/47 system (Morse et al. 1994).

Chapter 3

SUBARU HIGH-DISPERSION SPECTROSCOPY OF Hα AND [NII] 6583 Å EMISSION IN THE HL Tau JET

Abstract

We made slit scan observations with Hα and [NII] 6583 Å emission toward the HL Tau jet using the Subaru Telescope. High spectral resolution (R = 3.6$\times$ 10^4) revealed detailed kinematics of the jet and knots. The Hα emission shows the main jet component (-180 km s^{-1}) and distinct lower velocity components ($|V_{\rm LSR}| \leq 120$ km s^{-1}). The former component is continuously located over $\sim 20''$ peaking at bright knots previously identified (Knots A/B/C/D). The latter velocity components are associated with the lateral of the knots. The spatial and velocity structure at the knots seen in Hα can be explained by bow shocks. The line profiles at the bow shocks suggest that the preshock gas of the knots A–C have already moved outward by 180 $\sim$ 190 km s^{-1}. We conclude that ambient gas surrounding the jet is accelerated by prompt entrainment. The [NII] emission is mainly associated with bright knots, and also the base of the jet, with the [NII]/Hα flux ratio ranging between $<$ 0.1 and 0.7. The peak velocity of [NII] on the PVDs matches well the main jet component of Hα. Different [NII]/Hα ratios are attributed to either density or ionization of the preshock gas. At knots A–D, the [NII]/Hα flux ratio increases from $<$0.1 to 0.7 with distance from the source. This suggests that the preshock density decreases with distance from the source. The ratio at the lateral of the bow shocks is less than $\sim$0.1, suggesting that the ambient medium is almost neutral. At the base of the jet, the observed [NII]/Hα flux ratio decreases from 0.7 to 0.1 as the distance from the source increases. This suggests that the ionization fraction decreases through the radiative recombination.

3.1 INTRODUCTION

HL Tau is an active young stellar object (YSO) in transitional phase from an embedded Class I protostar to a Class II pre-main sequence star. It is located in the northeastern part of the L1551 dark cloud at a distance of ~140 pc. The optical jet is associated with this YSO was first detected by Mundt & Fried (1983). Based on the radio and optical studies, Brown et al. (1985) and Mundt et al. (1987) suggested that a jet (Knots A–D) in the vicinity of HL Tau probably originates from the VLA 1 source, located ~12″ northeast of HL Tau. However, further observations did not show the presence of VLA 1 (Rodríguez et al. 1992; Rodríguez et al. 1994; Wilner et al. 1996), indicating that its detection by Brown et al. (1985) was false detection. Therefore, it is likely that Knots A–D are associated with HL Tau. The jet was also observed in an [FeII] (1.644 μm) line in the near-infrared (Pyo et al. 2006). Interferometric observations of ^{13}CO(2-1) revealed a circumstellar envelope with a radius of 1400–2000 AU, a mass of 0.03–0.14 $M_\odot$, inclination of $i \sim 67°$ to the plane of the sky (Sargent & Beckwith 1991; Hayashi et al. 1993). Molecular outflow is also associated with HL Tau, and this roughly aligns with the optical jet (Monin et al. 1996; Cabrit et al. 1996). Further millimeter and sub-millimeter interferometry has revealed a circumstellar disk (r $\sim$ 60–180 AU; M $\sim$ 0.05 $M_\odot$) inside the envelope (Lay et al. 1994; Mundy et al. 1996; Wilner et al. 1996). Close et al. (1997) showed the presence of an expanding cavity associated with this YSO.

In this paper, we present detailed kinematics for the HL Tau jet measured by the high-resolution spectroscopy of the Hα 6563 Å and [NII] 6583 Å lines with the slit scan technique.

3.2 OBSERVATIONS AND DATA REDUCTION

We made slit-scan observations on 2002 December 18–19 using the High Dispersion Spectrograpgh (HDS) mounted on the Nasmyth focus of the 8.2-m Subaru Telescope. The long-slit mode with a 1″ × 60″ slit provided a velocity resolution of 8.3 km s^{-1} ($\lambda/\Delta\lambda = 3.6 \times 10^4$). The pixel scale was 0.″138 pixel^{-1}. An order-blocking filter (Hα) centered on 6580 Å allowed us to obtain a single echelle order (6541–6588 Å), including the Hα 6563 Å and [NII] 6583 Å lines. The spectra were obtained along the jet axis (P.A.= 52.°6) at six positions with a ~1″ separation. The slit positions are labeled as SP1 to SP6 from the southwest to the northwest in Figure 3.1. The offsets of the slit positions with respect to SP1 are shown in Table 3.1. Stars on a slit

viewer provided the positional accuracy of $0''.2$. The exposure time was 5400 s for each slit position. The average seeing was $0''.7$.

Data were reduced with the IRAF packages as the same manner as Chapter 2. We removed bad pixels and cosmic-ray events by combining the some frames. The wavelength calibration was carried out using a Th-Ar lamp and the IRAF tasks IDENTIFY, REIDENTIFY, FITCOORDS, and TRANSFORM in the noao.twodspec.longslit package. We subtracted the sky background and the stellar continuum from the spectra using BACKGROUND task with a linear fitting. The dark current, which is stable at 10 e^- per hour, was subtracted together with the sky background. Relative atmospheric transparency was corrected using stars in the slit viewer.

3.3 RESULTS

Figure 3.2 shows the position-velocity diagram (PVD) of the Hα and [NII] emission summed for the six slit positions, where Y is the projected angular distance from the south-eastern end of the slit position along the jet. The nomenclature labeled on the PVD follows Cohen & Jones (1987). The PVD shows an extended blueshift component at -200 km s^{-1} $\leq V_{\rm LSR} \leq -40$ km s^{-1} for $Y \geq 2''$ in Hα. This consists of two velocity components. A higher velocity component (hereafter "the main jet component") shows a typical radial velocity of $V_{\rm LSR} = -180$ km s^{-1} and $FWHM$ velocity of $V_{\rm FWHM} =$ 45 km s^{-1}. In contrast, a lower velocity component shows a typical radial velocity of $|V_{\rm LSR}| \leq 120$ km s^{-1} and $FWHM$ velocity of $V_{\rm FWHM} \sim$80 km s^{-1}. In contrast with the main jet component, the low velocity components are seen only at knots A–D.

In addition, the Hα emission shows a broad velocity emission extending over $V_{\rm LSR} \sim \pm$400 km s^{-1} at $2'' \leq Y \leq 8''$ with a blueshifted absorption peaking at $V_{\rm LSR} \sim -120$ km s^{-1}. It is almost symmetric toward the systemic radial velocity of $V_{\rm LSR} \sim +6.4$ km s^{-1} (Hayashi et al. 1993). The spatial distribution of the broad component matches well with the continuum from the star, which is scattered above the plane of the dusty envelope and accretion disk (Stapelfeldt et al. 1995). This component is presumably produced by infalling magnetospheric gas at the very close proximity (< 0.1 AU) of the driving source (e.g., Hartmann et al. 1994).

In [NII], the main jet component is seen at -190 km s^{-1} $\leq V_{\rm LSR} \leq -160$ km s^{-1} for $Y \geq 2''$. The typical radial velocity and $FWHM$ velocity are $V_{\rm LSR} = -180$ km s^{-1} and $V_{\rm FWHM} = 30$ km s^{-1}. In addition, at $3 \leq Y \leq 6''$, the [NII] emission shows a low blueshifted velocity component, which is significantly fainter than the extended blueshift component. It does not

apparently show the peak radial velocity. It extends over -100 km s^{-1} $\leq$ $V_{\rm LSR} \leq 0$ km s^{-1}.

Figure 3.3 shows the PVD of the Hα emission at six positions, together with the flux distribution of Hα integrated over the velocity from -272 km s^{-1} to $+17$ km s^{-1}. The nomenclature of the knot A-E and H labeled on the PVDs follows Cohen and Jones (1987). In the PVD of the slit position 1 (SP1), two bright features are clearly seen at $Y = 21''$ and $26''$. The former shows a peak radial velocity of $V_{\rm LSR} = -100$ km s^{-1} with a fainter higher velocity component peaking at $V_{\rm LSR} = -170$ km s^{-1}. This corresponds to the lateral of the knot A. The latter shows a peak radial velocity of $V_{\rm LSR} = -60$ km s^{-1}. This corresponds to the lateral of the knot B. Moreover, two faint features are seen at $Y = 31''$ and $41''$. Their radial velocity peak at $V_{\rm LSR} = -80$ km s^{-1} and -60 km s^{-1}, respectively. They correspond to the lateral of the knots C and D, respectively.

At SP2, the slit is placed at the brightest part of the knot A. A diffuse main jet component is seen at $5'' \leq Y \leq 20''$ with a peak velocity of $V_{\rm LSR}$ ~ -180 km s^{-1}. The emission feature corresponding to the knot H appears at $V_{\rm LSR} = -170$ km s^{-1}, $Y = 17''$. The higher velocity component at the knot A shows a peak velocity of $V_{\rm LSR} = -180$ km s^{-1}, and it is brighter than the lower velocity component. A higher velocity component of the knot B appears with a peak velocity of $V_{\rm LSR} = -170$ km s^{-1}. The lower velocity component at knots B and C is brighter than SP1, and also ~ 20 km s^{-1} more blueshifted. Another lower velocity feature associated with the knot D appears at $V_{\rm LSR} = -90$ km s^{-1}, $Y = 41''$.

In SP3, all the features seen in SP2 are also seen. Compared with SP2, knot H and the main jet component of knot B are brighter; knot A, the low velocity component of knot B, and the main jet component at $5'' \leq Y \leq 20''$ are fainter. In addition to these features, two bright features in the knot C appear at $Y = 32''$. Their peak velocities are $V_{\rm LSR} = -170$ km s^{-1} and -140 km s^{-1}, respectively.

The slit position SP4 is located at the brightest part of the knots B and C. The PVDs show all the features in SP3. Compared with SP3, knot D, and the high velocity component in the knots B and C, and are brighter. In contrast, knot H, A, and the low velocity components of knot B and C are fainter than SP3.

In the PVD for SP5, the main jet component at $Y< 20''$ disappears. The higher and lower velocity components at the knots B and C are fainter than SP4. The peak velocity at the higher velocity component of the knot C shows $V_{\rm LSR} = -190$ km s^{-1}. The lower velocity component at the knot D shows a peak velocity of $V_{\rm LSR} = -100$ km s^{-1}, ~ 20 km s^{-1} blueshifted than SP4.

At SP6, the slit position is located at the brightest part of the knot D.

Compared with SP5, the higher velocity component of the knot B and C is fainter while the lower velocity component at the knot B is brighter. A higher velocity component corresponding to the knot D appears at $V_{\rm LSR} = -190$ km s^{-1}, $Y = 43''$. A feature of the knot E (HL-E) appears at $Y = 47''$ and has a peak radial velocity of $V_{\rm LSR} = -210$ km s^{-1}.

Figure 3.4 shows the PVD of the [NII] 6583 Å emission, together with the flux distribution integrated over the same velocity range as Hα. The emission at $Y > 10''$ shows only the high velocity component associated with the main jet component, and it does not show the lower velocity component at $|V_{\rm LSR}| \leq 120$ km s^{-1}. The peak velocity of [NII] on the PVDs matches well the main jet component of Hα. The flux distribution of [NII] seems to match the apex of the knot and the base of the jet seen in Hα. In contrast to Hα, the [NII] emission does not show the lower velocity at $|V_{\rm LSR}| \leq 120$ km s^{-1}. While the Hα emission shows the scattered component from the star at $2'' \leq Y \leq 8''$, the [NII] emission does not show this component. Instead, the [NII] emission shows the lower blueshifted component in addition to the main velocity component at SP3 and SP4, $3'' \leq Y \leq 6''$.

Figure 3.5 shows the flux distribution of Hα integrated over the following velocity ranges: -240 to -120 km s^{-1} (high velocity component or HVC), -120 to 0 km s^{-1} (low velocity component or LVC), -120 to -60 km s^{-1} (LVC-high) and -60 to 0 km s^{-1} (LVC-low). The HVC is continuously located with peaking at each knot from the driving source to the Knot D. The LVC is located at left side of the lateral of the knots except for at both side of the knot B. The flux of the HVC is significantly larger than that of the LVC. The LVC-low is located at upstream of the LVC-high further away from the jet axis. The flux of the LVC-low at the lateral of the Knot B is much larger than that at other knots.

Figure 3.6 shows the flux distribution of the Hα and the [NII] emission integrated over the velocity (from -272 km s^{-1} to $+17$ km s^{-1}), and also the distribution of the [NII]/Hα flux ratio of the HVC and the flux distribution of the HVC and LVC of Hα in contours. The observed [NII]/Hα flux ratio ranges between 0.1 and 0.5, highest ahead of the knot C. The ratio clearly correlates with the peak of the flux distribution of the HVC in Hα except the knot B. At the laterral of the knot B, it is associated with the LVC. The ratio at the base of the jet is between 0.1 and 0.3 at $2''$ *leq* Y *leq* $10''$.

In the subsequent subsections, we describe the results for the spectroscopy in the base of the jet ($5'' \leq Y \leq 14''$) and knots A, B, C, D ($20'' \leq Y \leq 25''$, $25'' \leq Y \leq 30''$, $30'' \leq Y \leq 35''$ and $40'' \leq Y \leq 46''$) in detail.

3.3.1 The base of the jet

Figure 3.7 shows the line profiles at the base of the jet. In the case of the Figure 3.7 (a), a constant flux corresponding to the scattered component is subtracted at SP3 and SP4. The Hα emission clearly shows a single peak velocity of $V_{\rm LSR} \sim -180$ km s^{-1} at SP3 and SP4, and it is faint at SP2. This is associated with the main jet component. The $FWHM$ velocity at this component is $V_{\rm FWHM} \sim 45$ km s^{-1} at $Y = 5''$. It decreases toward the downstream by 10 km s^{-1} to $Y = 14''$. The brightness at this component peaks at SP3, $Y = 5''$ and decreases toward the downstream.

As shown in Figure 3.4 as well, the [NII] emission shows two velocity components at $3'' \leq Y \leq 6''$. A higher velocity component peaks at $V_{\rm LSR} \sim -180$ km s^{-1} and is associated with the main jet component as well as the Hα emission. The $FWHM$ velocity of the higher velocity component is ~ 35 km s^{-1}, ~ 10 km s^{-1} lower than Hα. As well as the Hα emission, at $Y \geq 6''$, the [NII] emission shows a single velocity component peaking at $V_{\rm LSR} \sim -180$ km s^{-1}. The brightest position in the [NII] emission is the same as the Hα emission, and its brightness significantly decreases toward the downstream. As described above, the base of the HL Tau jet is significantly affected by the scattered Hα emission from the star. Thus, we derive the [NII]/Hα flux ratio from the line profiles subtracted a constant flux corresponding to the scattered Hα emission in Figure 3.7. The measured ratio gradually decreases with Y : ~ 0.7 to ~ 0.1 for $Y = 5''$ to $Y = 14''$.

3.3.2 Knot A–D

Figure 3.8 shows the Hα flux distribution and the line profiles of Hα and [NII] in the knots A–D. At the knot A, the Hα emission shows two velocity components on the jet axis. The $FWHM$ velocity at the higher and lower velocity components are $V_{\rm FWHM} \sim 50$ km s^{-1} and ~ 100 km s^{-1}, respectively. The brightness in the knot A peaks at SP2, $Y = 23''$. In the western side of the jet axis, the Hα emission shows two velocity components. Its $FWHM$ velocity at higher velocity component is ~ 60 km s^{-1}, which is 10 km s^{-1} larger than that on the jet axis. The peak velocity at the lower component is the same as on the jet axis while the $FWHM$ velocity is ~ 120 km s^{-1}, 20 km s^{-1} larger than that on the jet axis. In the eastern side of the jet axis, the Hα emission also shows two velocity components which the lower velocity component is brighter than the higher velocity component. The peak velocity and $FWHM$ velocity at the higher velocity component are the same as the western side of the jet axis. The peak velocity and $FWHM$ velocity at the lower velocity component are $V_{\rm LSR} \sim -100$ km s^{-1} at Y=21$''$ and ~ 90

km s^{-1}, respectively. In contrast to the Hα emission, the [NII] emission does not show any velocity components in the Knot A. Therefore, the [NII]/Hα flux ratio is less than $\sim$ 0.1.

At the knot B, the Hα emission shows a single velocity component with less blueshifted wing on the jet axis. Its $FWHM$ velocity is $V_{\rm FWHM} \sim 45$ km s^{-1}. This is associated with the main jet component. It is brightest at SP4, $Y = 27''$. In the western side of the jet axis, the Hα emission mainly shows two velocity components. The peak velocity and $FWHM$ velocity at the higher velocity component are $V_{\rm LSR} \sim -170$ km s^{-1} and $V_{\rm FWHM} \sim 50$ km s^{-1}, respectively. For the lower velocity component, the peak velocity and $FWHM$ velocity are $V_{\rm LSR} \sim -110$ km s^{-1} and $V_{\rm FWHM} \sim 70$ km s^{-1}, respectively. In the eastern side of the jet axis corresponding to the SP2, the Hα emission also shows two velocity components. The peak velocity and $FWHM$ velocity at the higher velocity component are the same as the eastern side. The peak velocity at the lower velocity component gradually decreases with Y toward the lateral: $V_{\rm LSR} \sim -100$ km s^{-1} to ~ -60 km s^{-1} for SP3, $Y = 28''$ to SP1, $Y = 25''$. In contrast to the Hα emission, the [NII] emission show a single velocity component on the jet axis. Its peak velocity is the same as the Hα emission, as shown in Figure 3.4. Its $FWHM$ velocity is $\sim$ 35 km s^{-1}, $\sim$ 10 km s^{-1} lower than Hα. The [NII]/Hα flux ratio is $\sim$0.1 to $\sim$0.3 for SP3, $Y = 25''$ to SP4, $Y = 25''$. At both side of the jet axis, the [NII] emission does not show any velocity components. Therefore, the [NII]/Hα flux ratio is less than $\sim$ 0.1.

At the knot C, the Hα emission shows a single velocity component with less blueshifted wing on the jet axis. Its $FWHM$ velocity is $V_{\rm FWHM} \sim 40$ km s^{-1}. It is brightest at SP5, $Y = 34''$. In the western side of the jet axis, the Hα emission mostly shows a single velocity component the same as the main jet component. In contrast, the Hα emission predominantly shows two velocity components in the eastern side of the jet axis corresponding to the SP3. The peak velocity and $FWHM$ velocity at the higher velocity component are the same as the main jet component on the jet axis. The $FWHM$ velocity at the lower velocity component is $V_{\rm FWHM} \sim 80$ km s^{-1}. The peak velocity at the lower velocity component gradually decreases with Y toward the lateral: $V_{\rm LSR} \sim -120$ km s^{-1} to ~ -80 km s^{-1} for SP3, $Y = 34''$ to SP1, $Y = 31''$. The [NII] emission as well as the Hα emission show a single velocity component associated with the main jet component on the jet axis. Its peak velocity is the same as the Hα emission. Its $FWHM$ velocity is $\sim$ 30 km s^{-1}, $\sim$ 10 km s^{-1} less than that in Hα. The [NII]/Hα flux ratio increases with Y : $\sim$0.3 to $\sim$0.4 for SP4, $Y = 30''$ to SP4, $Y = 35''$. In contrast to the Hα emission, the [NII] emission is not clearly detected at either side of the jet axis. Therefore, the [NII]/Hα flux ratio is less than $\sim$

0.1.

At the knot D, the Hα emission shows a single velocity component on the jet axis. Its $FWHM$ velocity is $V_{\rm FWHM} \sim 30$ km s^{-1}. This is associated with the main jet component. Toward the downstream of the main jet component at SP6, $Y = 44''$–$46''$, the Hα emission shows two velocity components. The peak velocity at the higher velocity component is the same as the main jet component on the jet axis. The $FWHM$ velocity is $V_{\rm FWHM} \sim -45$ km s^{-1}, 15 km s^{-1} larger than that on the jet axis. The peak velocity and $FWHM$ velocity at the lower velocity component are $V_{\rm LSR} \sim -140$ km s^{-1} and $V_{\rm FWHM} \sim 80$ km s^{-1}, respectively. In the eastern side of the jet axis, the Hα emission predominantly shows a single velocity component. The peak velocity at this component gradually decreases with Y toward the lateral: $V_{\rm LSR} \sim -110$ km s^{-1} to ~ -60 km s^{-1} for SP5, $Y = 44''$ to SP1, $Y = 41''$. The [NII] emission as well as the Hα emission show a single velocity component associated with the main jet component on the jet axis. Its peak velocity is the same as the Hα emission. Its $FWHM$ velocity is ~ 20 km s^{-1}, ~ 10 km s^{-1} less than that in Hα. The [NII]/Hα flux ratio is $\sim$0.5 to $\sim$0.7 for SP6, $Y = 42''$ to SP6, $Y = 45''$. In the eastern side of the jet axis, the [NII] emission does not show any velocity components. Therefore, the [NII]/Hα flux ratio is less than ~ 0.1.

3.4 DISCUSSION

3.4.1 Prompt/Bow-shock entrainment

The knots A–C show two velocity components as described in §3.3.2. The higher velocity component originates from the apex of the knot, while the lower velocity component originates from the laterals. A similar kinematic structure is also observed in the HH 46/47 system. In Chapter 2, we showed the velocity structure of one-sided bow shocks and Hα filaments in HH 46/47 by comparing the high spatial resolution images obtained by *Hubble Space Telescope* with the radial velocities obtained by HDS. These clearly show that the higher velocity component is located at the apex of the bow shock and the lower velocity component is located at the lateral of the bow shock. The velocity structure of the knots seen in HL Tau is similar to those one-sided bow shocks in HH 46/47. Therefore, although the detailed structure is not clearly seen in our HL Tau images, we interpret that such knotty structures are associated with bow shocks.

In the observed line profiles, the lower velocity component peaks at $V_{\rm LSR}$ = -90 to -130 km s^{-1}, and two foot points of the line profile are blueshifted.

These profiles are considerably blueshifted from those of bow shock models by Hartigan et al. (1987). In the modeled profiles, the lower velocity emission peaks near the velocity of the ambient cloud, and its wing emission is redshifted. Such a tendency is also observed for the line profiles of HH 47B, and also several Hα filaments associated with the HH 47 jet (Chapter 2).

These can be interpreted as the outward motion of the ambient gas caused by the passage of the bow shock. The preshock velocity is estimated by subtracting the shock velocity from the 3-D velocity. We derive the 3-D velocity of $\sim$310 km s^{-1} from the radial velocity of ~ -180 km s^{-1}, adopting the average inclination of 36°. In the case of the knots A–B, we derive the shock velocity of $V_{\rm S} \sim 130$ km s^{-1} from the FWZI for the line profiles, assuming that a typical temperature of the shock heating regions in Hα is 10^5 K. The discrepancy between the shock velocity and the 3-D velocity can be explain that the preshock gas of the knots A–B have already moved outward by $\sim$180 km s^{-1}. In the case of the knot C, we derive the shock velocity of $V_{\rm S} \sim 120$ km s^{-1}. The discrepancy between the shock velocity and the 3-D velocity can be explain that preshock gas of the knot C have already moved outward by $\sim$190 km s^{-1}. Note that the assumed temperature of 10^5 K in the Hα emission line region is roughly consistent with the fact that the Hα line profile is broader than [NII] by $\sim$10 km s^{-1}.

Such outward motion of ambient gas is often attributed to entrainment by the collimated jet (Riera et al. 2001; Woitas et al. 2002). Based on the results described below, Mundt et al. (1990) argued that turbulent entrainment occurs at the edge of the jet in the HL Tau system. These authors made imaging and spectroscopic observations of Hα and [SII] 6716/6731 Å emission towards the HL Tau jet. Their results showed that the diameter of the jet in Hα is almost twice as broad as [SII]. This leads one to expect that the majority of the Hα emission arises from the outer shear layer while the [SII] emission arises from closer to the jet axis. However, our high S/N spectra do not show the presence of the turbulent shear layers, whose velocity must be lower than the main jet component. As discussed above, the lower velocity components in our spectra are seen only at the lateral of the knotty structures, and these are attributed to (one-sided) bow shocks rather than the turbulent shear layers. We thus suggest that the ambient gas is accelerated by prompt entrainment, which is the other entrainment mechanism proposed over a decade (e.g., Raga & Cabrit 1993) and observed in many other objects (see Chapter 2, and references therein).

3.4.2 [NII]/Hα Flux Ratios and Implications for Pre-Ionization

Chapter 2 shows that the [NII]/Hα flux ratio depends on ionization and density of preshock gas. If the shock velocity is less than 100 km s^{-1}, the [NII]/Hα flux ratio significantly depends on the ionization fraction of the preshock gas. If the preshock gas is fully ionized, the ratio is $\sim$0.7. In contrast, if it is neutral, it is less than $\leq$0.2. In contrast, if the shock velocity is more than 100 km s^{-1}, the [NII]/Hα flux ratio does not depend on the ionization fraction of the preshock gas because the UV radiation from the postshock regions ionizes the preshock gas. Instead, the [NII]/Hα flux ratio clearly depends on the preshock density. If the preshock density is 10^2 cm^{-3}, the ratio is $\sim$0.6, and also if it is 10^3 cm^{-3}, it is $\sim$0.5. This indicates if the preshock density increases, the [NII]/Hα flux ratio decreases.

As shown in §4.1, the shock velocity for the knots A–C is V = 120 to 130 km s^{-1}. As described in §3, the high [NII]/Hα flux ratio is mainly associated with the bow shocks caused by interaction between the jet and ambient gas except for the base of the jet at $Y \leq 14''$, not the main jet component. These ratios at the apex of the knots A–D are $\sim$0.1, $\sim$0.2, $\sim$0.4 and $\sim$0.7, respectively. The increase of the [NII]/Hα flux ratio from knot A to knot D suggests that the preshock density decreases with distance from the source. In contrast, the ratio at the lateral is less than $\sim$0.1, suggesting that the ambient medium is almost neutral.

The shock velocity for the jet ejecta is not derived from the same way as the bow shock. Thus, we presume that the upper limit of the shock velocity in the main jet component is $FWHM$ velocity (45 km s^{-1}) at most. In the case of the base of the jet within $Y = 14''$, the observed [NII]/Hα flux ratio is 0.7 to 0.1 at $Y = 5''$ to $Y = 14''$. Such a decrease with distance from the source suggests that the ionization fraction decreases through the radiative recombination. In contrast, in the case of the main jet component at $Y \geq 14''$, it is less than $\sim$0.2, implying that the main jet component is almost neutral. The high [NII]/Hα flux ratio ahead of the knot C would be caused by the UV radiation from the postshock region.

3.5 SUMMARY

We have made slit scan observations with Hα and [NII] 6583 Å emission toward the HL Tau jet using the Subaru Telescope and HDS. The main results are summarized as follows:

(1) The Hα emission shows the main jet component ($-$180 km s^{-1}) and

distinct lower velocity components ($|V_{\rm LSR}| \leq 120$ km s^{-1}). The former component is continuously located over $\sim$ 30 peaking at bright knots previously identified (Knots A/B/C/D). The latter velocity components are associated with the lateral of the knots. The [NII] emission is mainly associated with bright knots, and also the base of the jet. The peak velocity of [NII] on the PVDs matches well the main jet component of Hα. The observed [NII]/Hα flux ratio remarkably vary from one region to another: 0.1–0.7 at the base of the jet, less than 0.1 in knot A, $\sim$0.2 in knot B, $\sim$0.4 in knot C, and $\sim$0.7 in knot D.

(2) The knots A–C show the two velocity components. The higher velocity component (-180 km s^{-1}) originates from the apex of the knot, while the lower velocity component (-90 to $-$ 130 km s^{-1}) originates from the laterals. The spatial and velocity structure at the knots seen in Hα can be explained by bow shocks. The shock velocity derived from the line profiles in Hα is 130 km s^{-1} for knots A–B and 120 km s^{-1} for knot C, remarkably smaller than the 3-D velocity ($\sim$310 km s^{-1}). The discrepancy between the shock velocity and the 3-D velocity can be explain that the preshock gas of the knots A–B and knot C have already moved outward by $\sim$180 km s^{-1} and $\sim$190 km s^{-1}, respectively.

(3) The Hα emission shows a constant radial velocity of $V_{\rm LSR} = -180$ km s^{-1} in the main jet component ($\Delta V = 10$ km s^{-1}) even at the edge of the jet except for the lower velocity components at the lateral of the knots (bow shock regions). Furthermore, the lower velocity components are attributed to bow shocks rather than the turbulent shear layers. We thus suggest that ambient gas surrounding the jet is accelerated by prompt entrainment, not turbulent entrainment.

(4) Our slit-scan observations revealed that the high [NII]/Hα flux ratio is mainly associated with the bow shocks caused by interaction between the jet and ambient gas and the base of the jet. At knots A–D, the [NII]/Hα flux ratio increases from $<$0.1 to 0.7 with distance from the source. This suggests that the preshock density decreases with distance from the source. In contrast, the ratio at the lateral is less than $\sim$0.1, suggesting that the ambient medium is almost neutral. The assumed upper limit of the shock velocity in the main jet component is $FWHM$ velocity (45 km s^{-1}) at most. At the base of the jet, the observed [NII]/Hα flux ratio decrease with distance from the source, suggesting that the ionization fraction decreases through the radiative recombination. In contrast, it is less than $\sim$0.2 in the main jet component further away from the source, suggesting that the main jet component is almost neutral.

Reference

Brown, A., Mundt, R., & Drake, S. A. 1985, ASSL Vol. 116: Radio Stars, 105

Cabrit, S., Guilloteau, S., André, P., Bertout, C., Montmerle, T., & Schuster, K. 1996, A&A, 305, 527

Close, L. M., Roddier, F., Northcott, M. J., Roddier, C., & Graves, J. E. 1997, ApJ, 478, 766

Cohen, M., & Jones, B. F. 1987, ApJ, 321, 846

Hartigan, P., Raymond, J., & Hartmann, L. 1987, ApJ, 316, 323

Hartmann, L., Hewett, R., & Calvet, N. 1994, ApJ, 426, 669

Hayashi, M., Ohashi, N., & Miyama, S. M. 1993, ApJ, 418, L71

Lay, O. P., Carlstrom, J. E., Hills, R. E., & Phillips, T. G. 1994, ApJ, 434, L75

Monin, J.-L., Pudritz, R. E., & Lazareff, B. 1996, A&A, 305, 572

Morse, J. A., Hartigan, P., Heathcote, S., Raymond, J. C., & Cecil, G. 1994, ApJ, 425, 738

Mundt, R., Buehrke, T., Solf, J., Ray, T. P., & Raga, A. C. 1990, A&A, 232, 37

Mundt, R., Brugel, E. W., & Buehrke, T. 1987, ApJ, 319, 275

Mundt, R., & Fried, J. W. 1983, ApJ, 274, L83

Mundy, L. G., et al. 1996, ApJ, 464, L169

Pyo, T.-S., et al. 2006, ApJ, 649, 836

Riera, A., López, R., Raga, A. C., Anglada, G., & Estalella, R. 2001, Revista Mexicana de Astronomia y Astrofisica, 37, 147

Raga, A., & Cabrit, S. 1993a, A&A, 278, 267

Rodríguez, L. F., Canto, J., Torrelles, J. M., Gomez, J. F., Anglada, G., & Ho, P. T. P. 1994, ApJ, 427, L103

Rodríguez, L. F., Canto, J., Torrelles, J. M., Gomez, J. F., & Ho, P. T. P. 1992, ApJ, 393, L29

Sargent, A. I., & Beckwith, S. V. W. 1991, ApJ, 382, L31

Stapelfeldt, K. R., et al. 1995, ApJ, 449, 888

Wilner, D. J., Ho, P. T. P., & Rodríguez, L. F. 1996, ApJ, 470, L117

Woitas, J., Eislöffel, J., Mundt, R., & Ray, T. P. 2002, ApJ, 564, 834

slit number	1	2	3	4	5	6
offset	0	$0''.9$	$1''.9$	$2''.9$	$4''.0$	$4''.9$

Table 3.1: Offset of slit positions for HL Tau

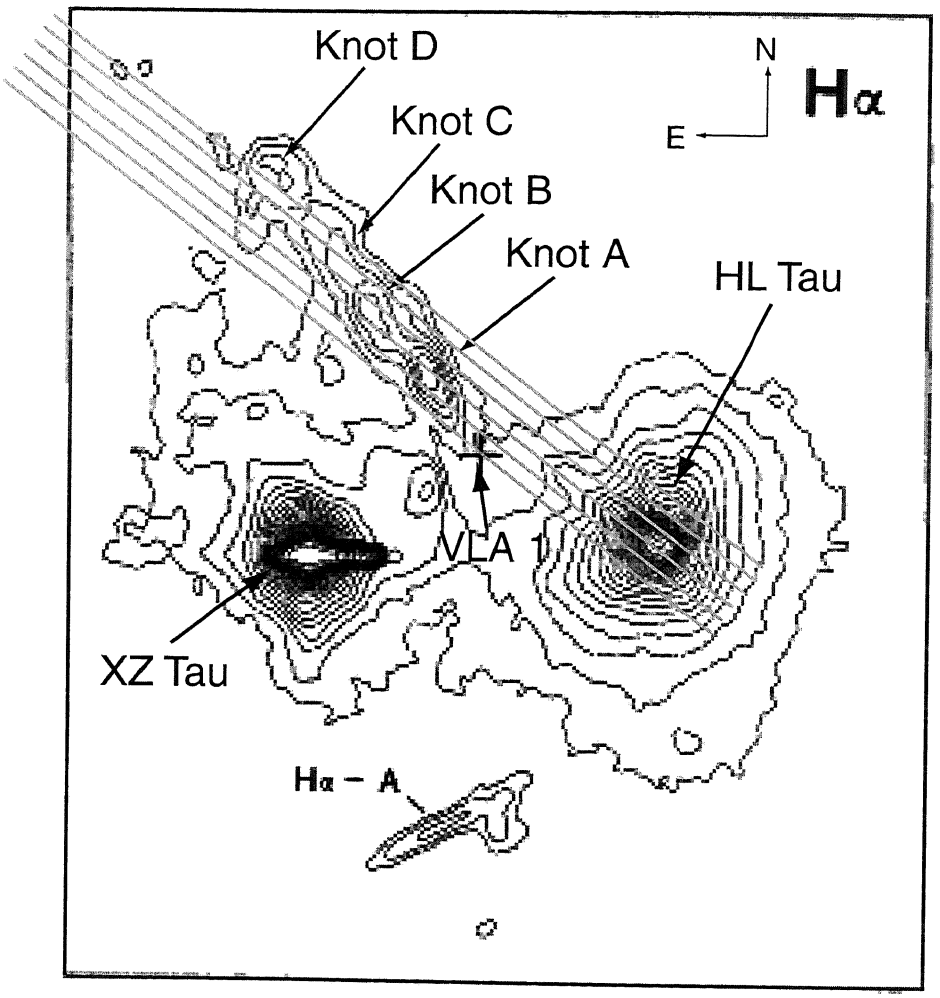

Figure 3.1: Slit positions on an image of Hα emission toward the HL Tau jet. We use the nomenclature of Cohen & Jones (1987) for some HH knots. The image was obtained by Mundt et al. (1987). The reflection nebula at optical wavelength extends northeast of the stellar position along the direction of HL Tau's optical jet. The slit length and width are 60″ and 1″, respectively. The position angle of the slit is 52.6°. The north is up and east is left.

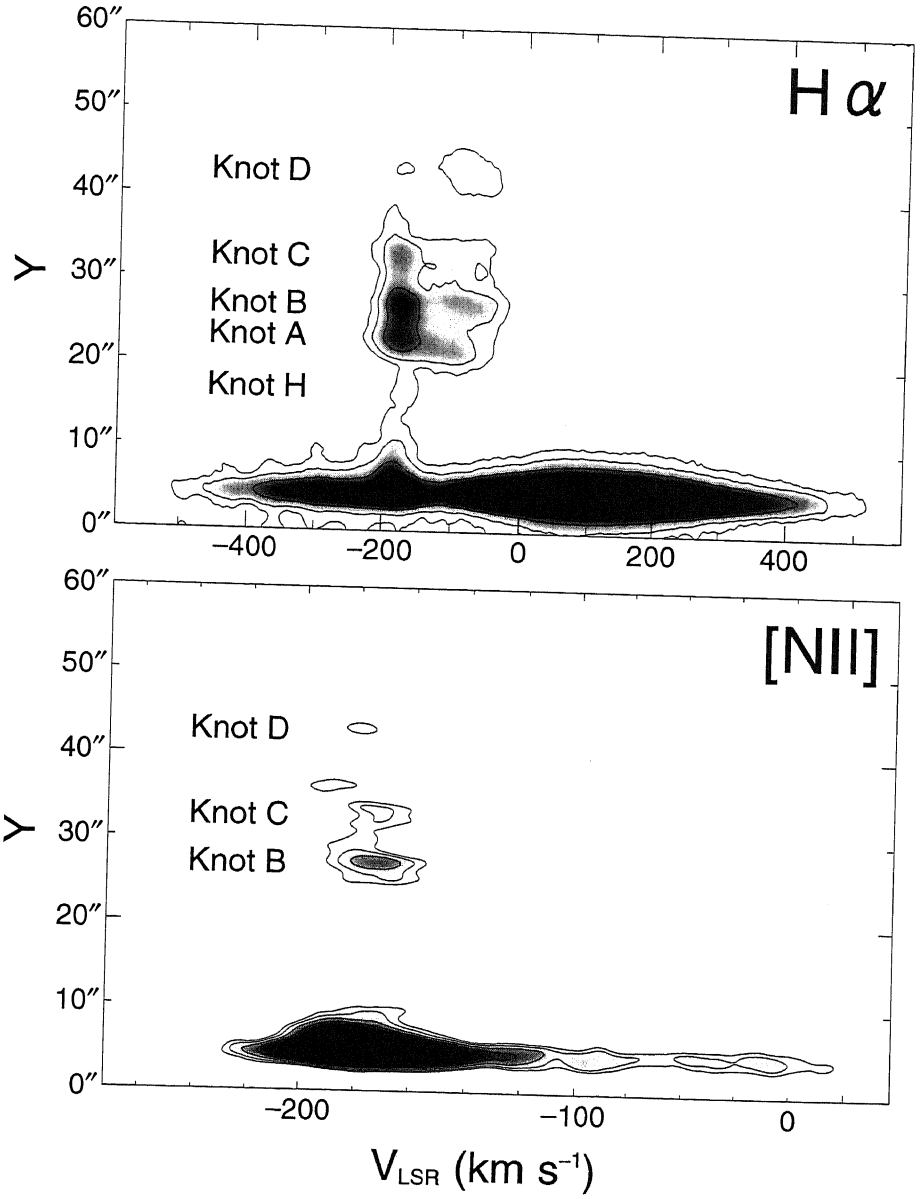

Figure 3.2: Position-velocity diagrams of the Hα (upper panel) and [NII] 6583 Å (lower panel) emission summed over the eight slit positions. The velocity is shown with respect to the local standard of rest (LSR). Y is the projected angular distance measured along the jet. The PVDs are smoothed by a Gaussian with $\sigma_G = 4$ pixel. Contours are indicated from 4 σ to 2700 σ for Hα and from 4 σ to 105 σ for [NII] with equal intervals in a logarithmic scale.

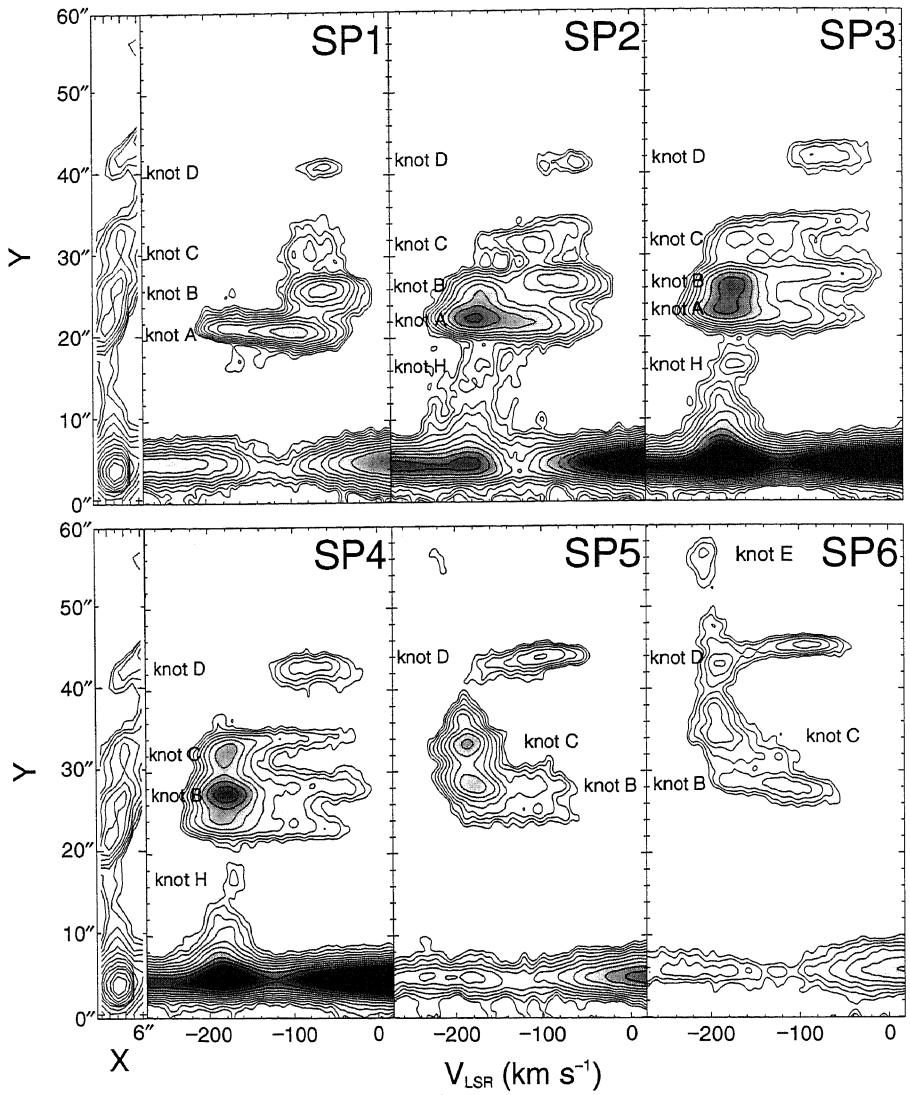

Figure 3.3: The Hα intensity distribution and eight position-velocity diagrams obtained from our HDS observations toward the HL Tau jet. We use the nomenclature of Cohen & Jones (1987) for some HH knots. The jet direction is up in each panel. The intensity for each grid in obtained by integrating the line profile from -272 km s^{-1} to $+17$ km s^{-1}. The horizontal axis is the slit number. Y is the projected angular distance measured along the jet. The PVDs are smoothed by a Gaussian with $\sigma_G = 4 \times 4$ pixel (3.4 km s^{-1} $\times$ 0.″6). Contours are indicated from 5-54σ, 5-108 σ, 5-135 σ, 5-162 σ, 5-81 σ, 5-135 σ, respectively, with equal intervals in a logarithmic scale for SP1 to SP8.

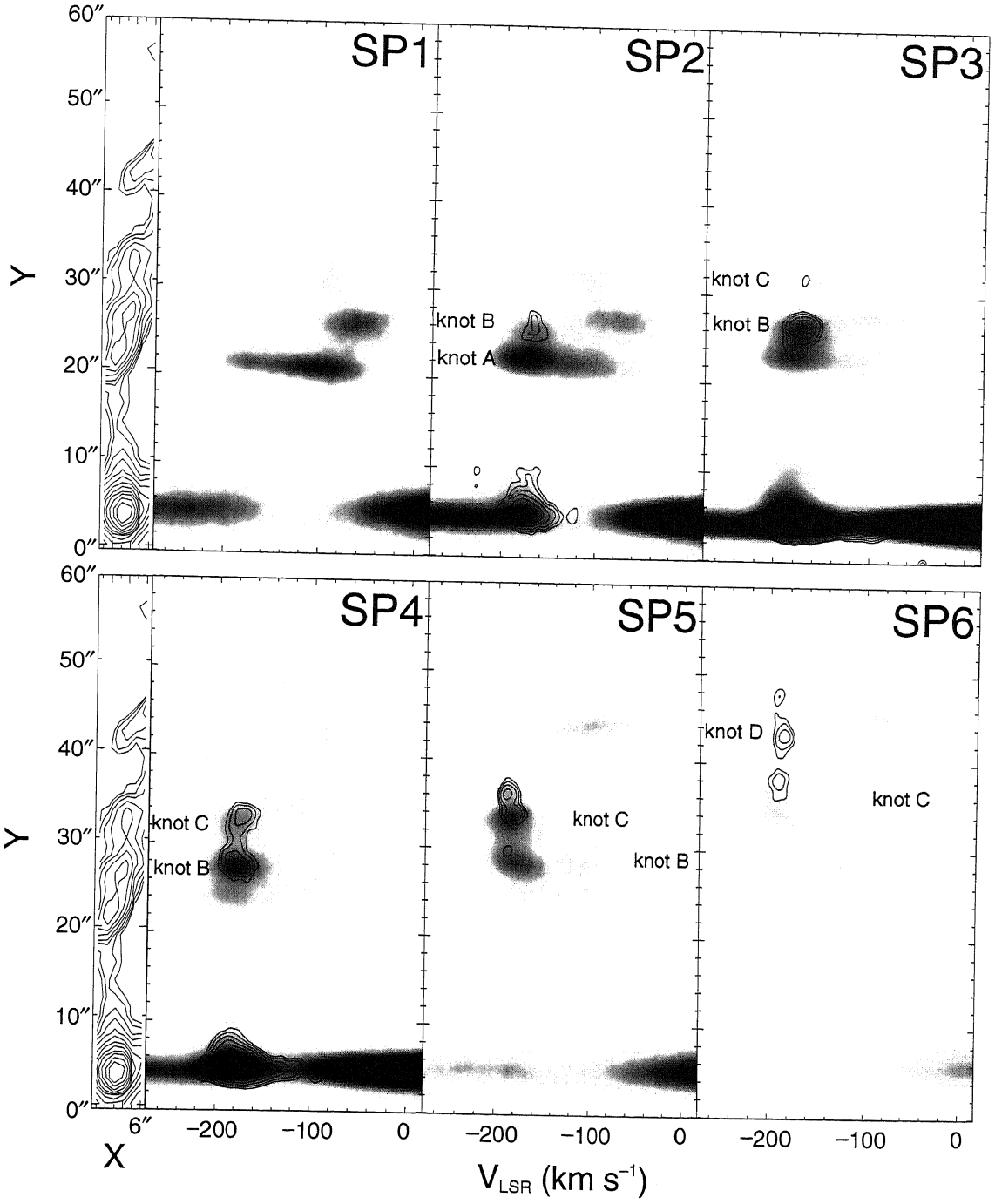

Figure 3.4: Same as Figure 3, but the contours show the [NII] 6583 Å emission. The gray scale shows the Hα emission in the Figure 3. The contours are indicated from 5-41σ, 5-50 σ, 5-50 σ, 5-50 σ, 5-41 σ, 5-41 σ, respectively, with equal intervals in a logarithmic scale.

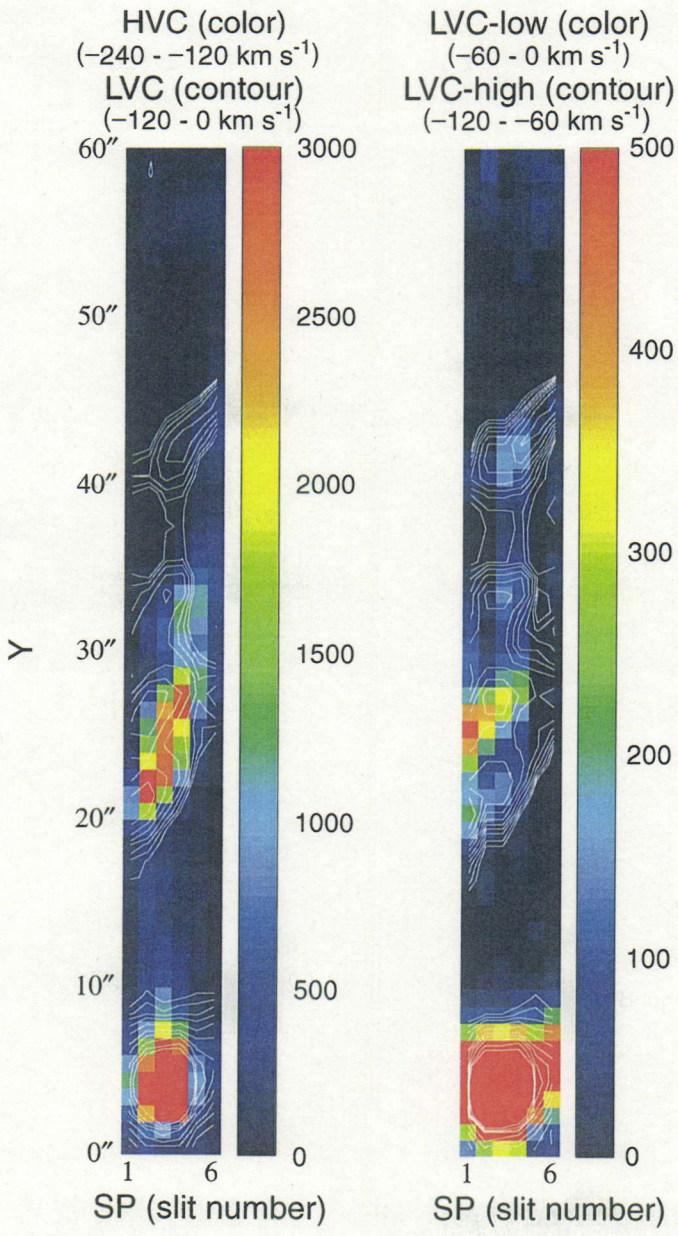

Figure 3.5: The intensity distribution of Hα integrated over the following velocity ranges: HVC (-240 to -120 km s^{-1}; left color), LVC (-120 to 0 km s^{-1}; left contour), LVC-high (-120 to -60 km s^{-1}; right color), LVC-low (-60 to 0 km s^{-1}; right contour). The horizontal axis is the slit number and the vertical axis is the projected angular distance. The right side bars for the figures are shown in arbitrary unit. Contour is indicated with equal intervals in a logarithmic scale for intensity of Hα.

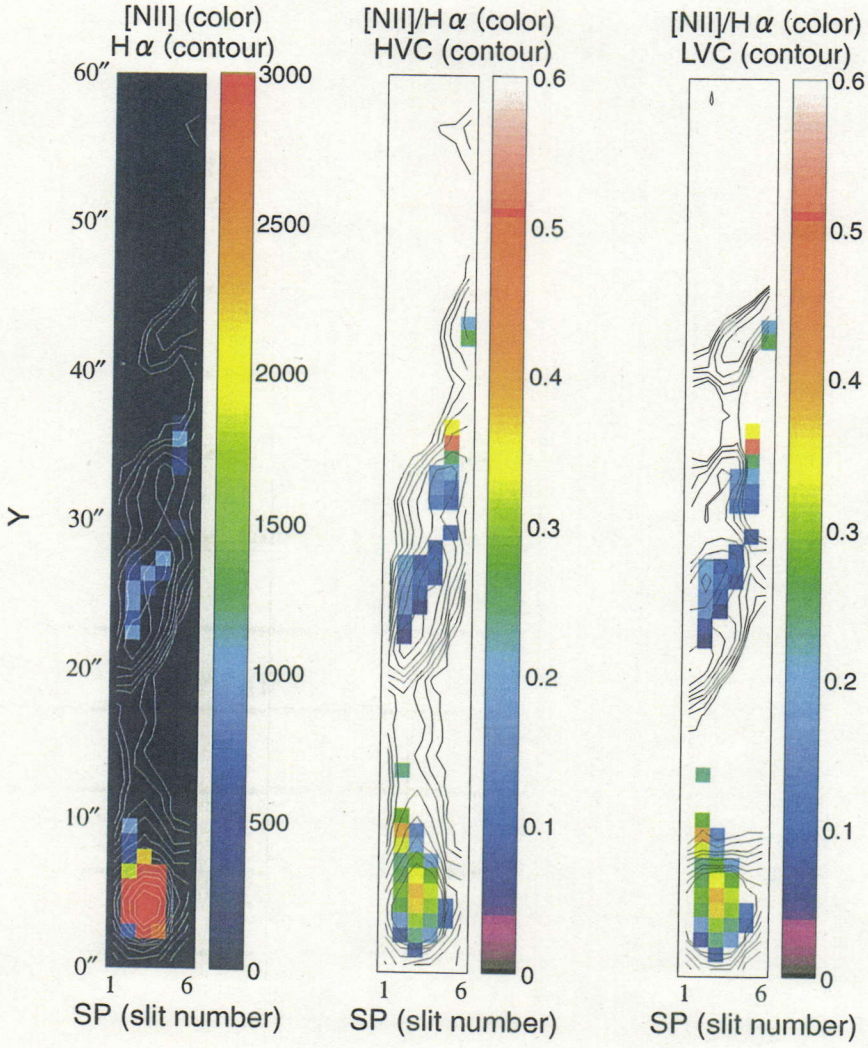

Figure 3.6: The intensity distribution of Hα (left contour) and [NII] 6583 Å (left color) and the [NII]/Hα flux ratio (middle, right color) with the intensity distribution of the HVC (middle contour) and LVC (right contour) of Hα. The intensity for the left figure is obtained by integrating the line profile from -272 km s^{-1} to $+17$ km s^{-1}. The horizontal axis is the slit number and the vertical axis is the projected angular distance. The right side bar for the left figure is shown in arbitrary unit. The [NII]/Hα flux ratio of the HVC in the middle and right figures is shown for the regions with S/N$\geq$ 3. Contour is indicated with equal intervals in a logarithmic scale for intensity of Hα.

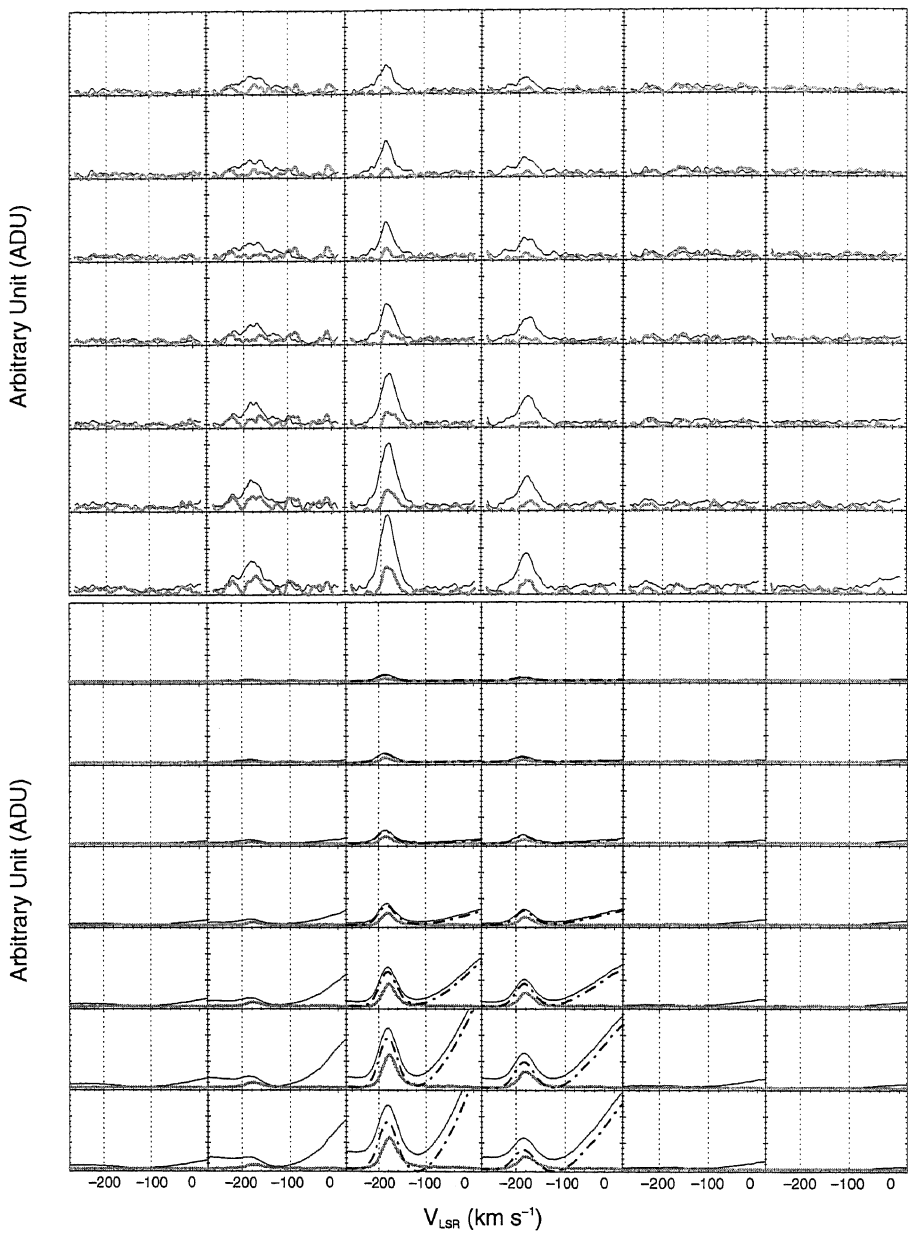

Figure 3.7: Line profiles of the Hα (black) and [NII] 6583 Å (gray) in the base of the HL Tau jet. Hα emission at SP3 and SP4 is contaminated by the scattered emission from the star, thus a constant is subtracted at each box to show a true component from the jet (black dot-dash). The positions on the lower panel correspond to $Y = 4\farcs5$, $5\farcs2$, $5\farcs8$, $6\farcs5$, $7\farcs2$, $7\farcs9$ and $8\farcs6$ from the bottom, respectively. The positions on the upper panel correspond to $Y = 9\farcs3$, $10\farcs0$, $10\farcs7$, $11\farcs4$ and $12\farcs1$, $12\farcs8$ and $13\farcs5$ from the bottom, respectively.

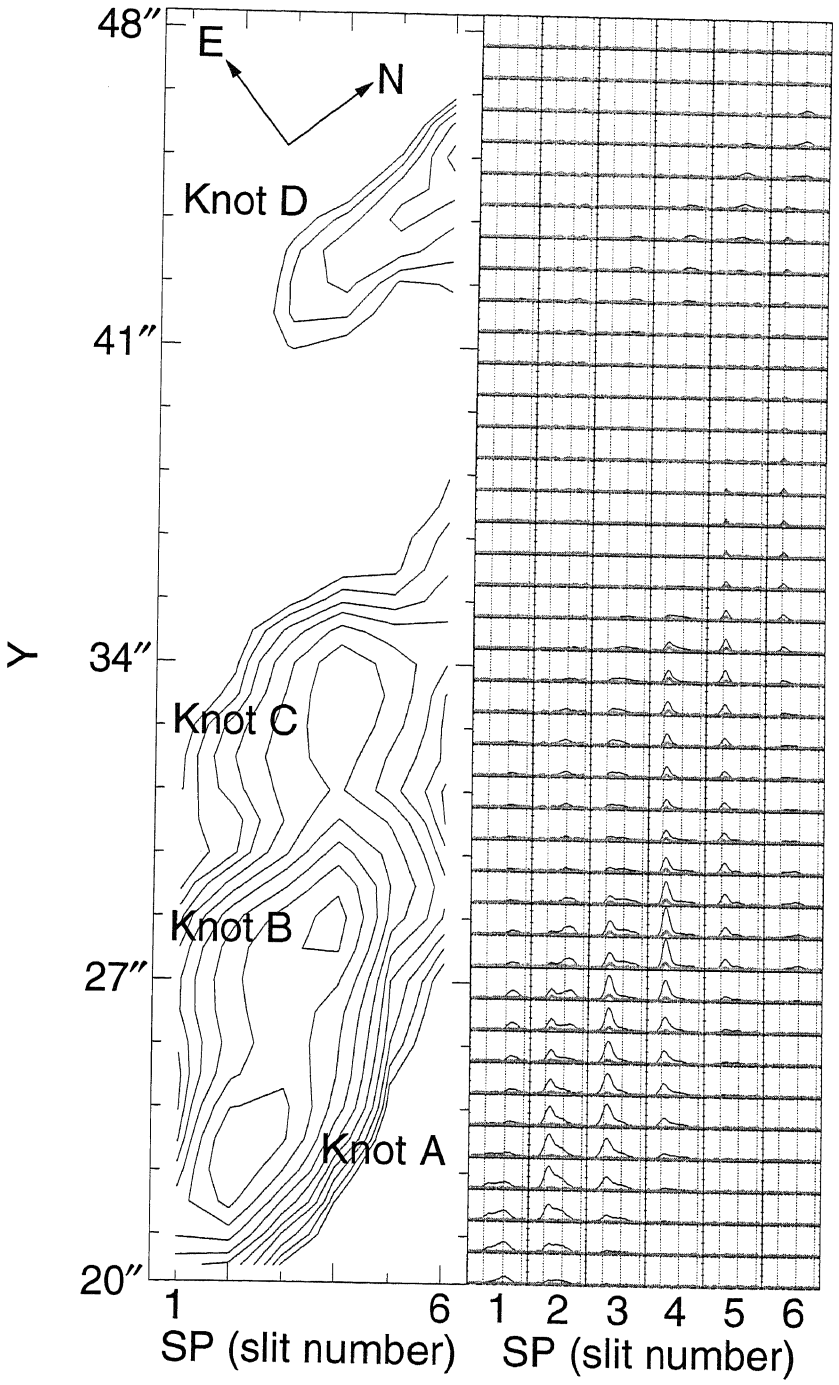

Figure 3.8: The Hα intensity distribution and the line profiles in the knot A–D. The line profiles are shown from 20″ to 48″ in steps of 0.″7. The horizontal axis is the slit number and the vertical axis is the projected angular distance.

Chapter 4

DISCUSSION

4.1 Velocity of the Surrounding Gas

As shown in Chapter 2, 3, HH 47B and a filament at the flank of knot A22 in the HH 46/47 system and the knots A–C in the HL Tau system clearly shows two velocity components. The presence of such two velocity components is well explained by a bow shock (Hartigan et al. 1987): the two components are attributed to different regions in a bow shock; (1) the higher velocity component arises from near the bow apex, (2) the lower velocity component arises from its wings.

Figure 4.1 shows the observed line profile at the knot B in HL Tau and the modeld line profile by Hartigan et al. (1987). In the observed line profile, the lower velocity component peaks at $V_{\rm LSR} \sim -80$ km s^{-1}, and two foot points of the line profile are blueshifted. This profile is considerably blueshifted from that of bow shock models. In the modeled profile, lower velocity component peaks close to the systemic velocity of the ambient gas, with a wing emission extending toward the redshifted side. These results are explained if the ambient gas is already moving outward because of the passage of the previous bow shocks.

The preshock velocity of a bow shock is estimated by subtracting the shock velocity from the 3-D velocity of the bow shock, which corrected inclination angle. According to the model calculations by Hartigan et al. (1987), the shock velocity V_S is estimated from the following equation; SM is the $FWHM$ due to thermal broadening:

$$Vs = FWZI = MX0.1 - MN0.1 - SM, \tag{4.1}$$

As shown in 2.4.3, a typical temperature of the shock heating regions in Hα is 10^5 K. The shock velocity, 3D velocity and velocity of the surrounding

gas for HH 46/47 and HL Tau are summarized in Table 4.1 and 4.2, respectively. The discrepancy between the shock velocity and the 3-D velocity can be explain that the preshock gas have already moved outward.

4.2 Kinematics in Hα Emission and Implications for Entrainment

As described in Chapter 1, two entrainment mechanisms have been discussed to date: these are, turbulent entrainment and prompt entrainment.

As described in Chapter 2, Hartigan et al. (1993) argued the presence of turbulent entrainment with the HH 46/47 system. Figure 4.2 shows channel maps for -170 km s^{-1} and -110 km s^{-1} obtained by Fabry-Perot observations of Hα by Hartigan et al. (1993). The Hα emission occurs along the edges as well as the jet axis. In addition, Figure 4.3 shows the difference image of [SII] minus Hα made using the velocity images from -80 km s^{-1} to -230 km s^{-1} by Hartigan et al. (1993). The boundary regions along the edge of the jet show high Hα/[SII] line ratios, indicative of high shock velocities. Therefore, these are explained if Hα originates from turbulent mixing layers between the jet and surrounding material.

In contrast, Heathcote et al. (1996) argued the presence of prompt entrainment from *HST* observations. Figure 4.4 shows the sum and minus of the Hα and [SII] *HST* images of the HH 46/47 jet by Heathcote et al. (1996). This indicates that the Hα emission arises from bow shocks, ejecta of the jet, and filamentary structures located at the edge of the jet. Based on these results, Heathcote et al. (1996) conclude that the dominant process that accelerates the surrounding gas is not turbulent entrainment, but prompt entrainment, where the major bow shock HH 47D and HH 47A, aided by the lesser but more frequent Hα filaments, push material ahead of the jet.

However, it is not necessarily the case that *HST* observations resolved this issue, because the *HST* observations would be less sensitive to faint and extended emission due to a relatively small aperture of the telescope, and also small pixel sampling. Thus, these might have missed the emission from the turbulent mixing layers observed by Hartigan et al. (1993). In fact, our spectra show the presence of faint and extended emission, which is not clearly seen in the *HST* image.

However, our high sensitive observation do not show the presence of separate slow streams as the two sides of the HH 47 jets—the streams seen in Hartigan et al. (1993). Our spectra show that the Hα has a radial velocity of $V_{\rm LSR} \sim -160$ km s^{-1} even at the edge of the jet except for the

bow shock regions. In addition, the observed velocity of Hα in the main jet component well matches that of [NII], whose excitation condition is similar to [SII], which originates from regions closer to the jet axis. These suggest that Hα originates from the ejecta of the jet similar to [SII] and [NII], but not from turbulent mixing layers as was argued by Hartigan et al. (1993) and Raymond et al. (1994). Therefore, we suggest that the ambient gas is accelerated by prompt entrainment.

As described in Chapter 3, Mundt et al. (1990) argued that turbulent entrainment occurs at the edge of the jet in the HL Tau system. Figure 4.5 shows diameter of the Hα and [SII] as a function of distance from Mundt et al. (1990). This indicates that the diameter of the jet in Hα is almost twice as broad as [SII], leading one to expect that the majority of the Hα emission arises from the outer shear layer while the [SII] emission arises from closer to the jet axis. However, our high sensitive spectra do not show the presence of the turbulent shear layers, whose velocity must be lower than the main jet component. The lower velocity components in our spectra are seen only at the lateral of the knotty structures, and these are attributed to (one-sided) bow shocks rather than the turbulent shear layers. As well as HH 46/47, we thus suggest that the ambient gas is accelerated by prompt entrainment.

4.3 [NII]/Hα Flux Ratios and Implications for Pre-Ionization

As described in Chapter 2, Figure 12 shows that the [NII]/Hα flux ratio depends on ionization and density of preshock gas. If the shock velocity V_S is less than 100 km s^{-1}, the [NII]/Hα flux ratio significantly depends on the ionization fraction of the preshock gas. If the preshock gas is fully ionized, the ratio is $\sim$0.6. In contrast, if it is neutral, it is less than $\leq$0.2. In contrast, if the shock velocity V_S is more than 100 km s^{-1}, the [NII]/Hα flux ratio does not depend on the ionization fraction of the preshock gas because the UV radiation from the postshock regions ionizes the preshock gas. Instead, the [NII]/Hα flux ratio clearly depends on the preshock density. If the preshock density is 10^2 cm^{-3}, the ratio is $\sim$0.6, and also if it is 10^3 cm^{-3}, it is $\sim$0.5. This indicates if the preshock density increases, the [NII]/Hα flux ratio decreases.

In the HH 46/47 sytem, the observed [NII]/Hα flux ratio ranges from 0.2 to 0.5 in the main jet component. It is 0.5 at the apex of the bow shock, and less than 0.1 at the lateral of the bow shock. It is $\sim$0.3 at the Hα filament. The ratios in some regions are markedly higher than the

typical ratio suggested by previous observations ($\sim$0.2, Morse et al. 1994). A possible interpretation is that the preshock gas in these regions is significantly ionized, as described below in detail.

The shock velocity in the main jet component is not derived from the same way as the bow shock. Thus, we presume that the upper limit of the shock velocity in the main jet component is $FWHM$ velocity (45 km s^{-1}) at most. Performing comparisons with Figure 2.12, we suggest that the main jet component is considerably ionized compared with the previous estimates ($<$ 0.2 —Hartigan et al. 1994; Bacciotti & Eislöffel 1999). The [NII]/Hα flux ratio in the Hα filament is significantly lower than that in the main jet component, indicating that the ambient gas surrounding the jet is almost neutral. The [NII]/Hα flux ratio is high at the apex of the bow shocks, while it is low at the lateral. A possible interpretation is that the preshock gas is partially ionized at the apex, while the ambient gas surrounding the jet is almost neutral at the lateral.

As shown in Chapter 3, the shock velocity for the knots A–C in the HL Tau sytem is V = 120 to 130 km s^{-1}. The high [NII]/Hα flux ratio is mainly associated with the bow shocks caused by interaction between the jet and ambient gas except for the base of the jet at $Y \leq 14''$, not the main jet component. These ratios at the apex of the knots A–D are $\sim$0.1, $\sim$0.2, $\sim$0.4 and $\sim$0.7, respectively. The increase of the [NII]/Hα flux ratio from knot A to knot D suggests that the preshock density decreases with distance from the source. In contrast, the ratio at the lateral is less than $\sim$0.1, suggesting that the ambient medium is almost neutral.

The upper limit of the shock velocity for the jet ejecta is $FWHM$ velocity (45 km s^{-1}) as well as main jet component in HH 46/47 system. In the case of the base of the jet within $Y = 14''$, the observed [NII]/Hα flux ratio is 0.7 to 0.1 at $Y = 5''$ to $Y = 14''$. Such a decrease with distance from the source suggests that the ionization fraction decreases through the radiative recombination. In contrast, in the case of the main jet component at $Y \geq 14''$, it is less than $\sim$0.2, implying that the main jet component is almost neutral. The high [NII]/Hα flux ratio ahead of the knot C would be caused by the UV radiation from the postshock region.

We compare the [NII]/Hα flux ratio in the main jet components of the HH 46/47 jet and the HL Tau jet. The ratio for the HH 46/47 is high (0.2–0.5), compared with that for the HL Tau ($\leq$0.2). This indicates the high ionization fraction than a typical ratio ($\leq$0.2) suggested by previous observations (Morse et al. 1994). A possible interpretation is that the radiation from the O star ζ Pup and γ^2 Vel neaby the HH 46/47 irradiates the ambient gas, causing the high ionization fraction in the main jet component. On the contrary, the HL Tau is not affected an external circumstance becauses it is

located in the isolated molecular cloud.

Another possible interpretation is that the radiative cooling through recombination efficiently arises with distance from the source in the HL Tau jet, but not in the HH 46/47 jet because of the low density ($\sim$100 cm^{-3}). This allows the high ionization fraction in the HH 46/47 jet even away from the source.

HH 46/47	HH 47A	A22	HH 47B
shock velocity (km s^{-1})	60	55	80
3-D velocity (km s^{-1})	260	280	280
velocity of the surrounding gas (km s^{-1})	200	225	210

Table 4.1: Shock velocity, 3-D velocity & velocity of the surrounding gas for HH 46/47

HL Tau	Knot A	Knot B	Knot C
shock velocity (km s^{-1})	130	130	120
3-D velocity (km s^{-1})	310	310	310
velocity of the surrounding gas (km s^{-1})	180	180	190

Table 4.2: Shock velocity, 3-D velocity & velocity of the surrounding gas for HL Tau

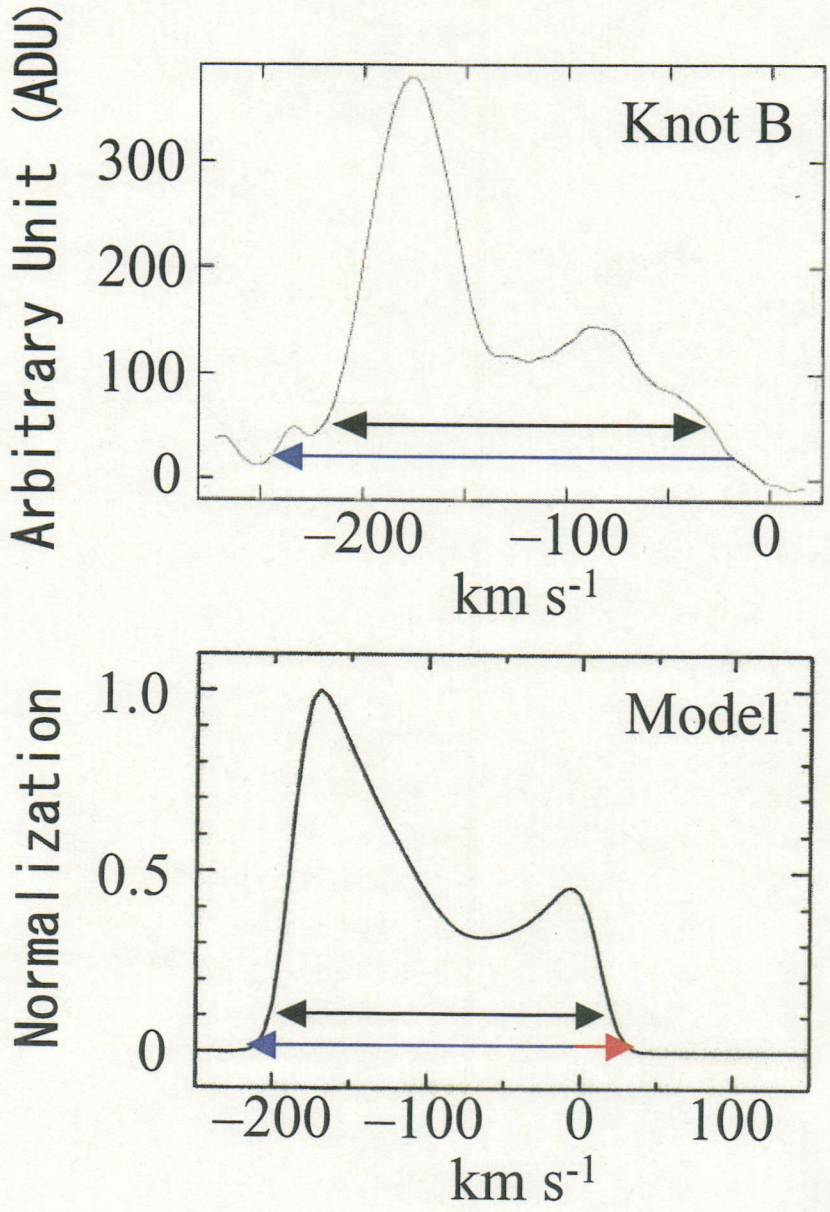

Figure 4.1: The observed line profile at the knot B in HL Tau and the modeled line profile by Hartigann et al. (1987)

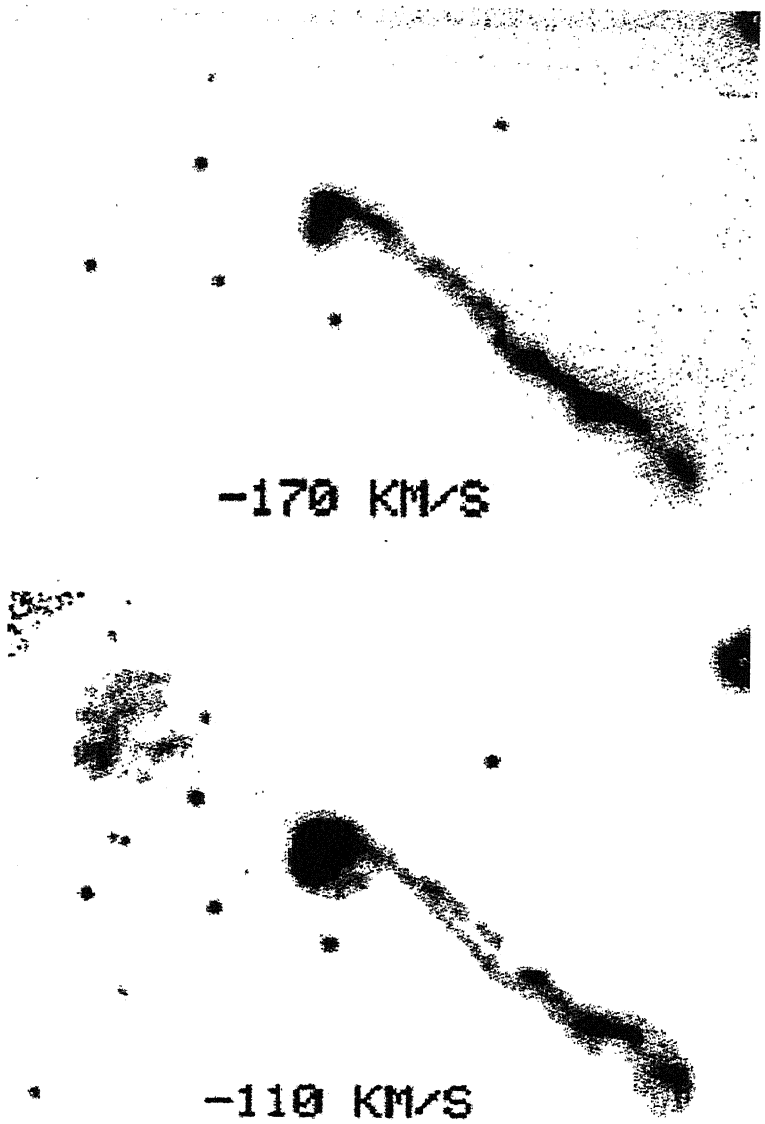

Figure 4.2: Channel maps for -170 km s^{-1} and -110 km s^{-1} obtained by Fabry-Perot observations of Hα by Hartigan et al. (1993).

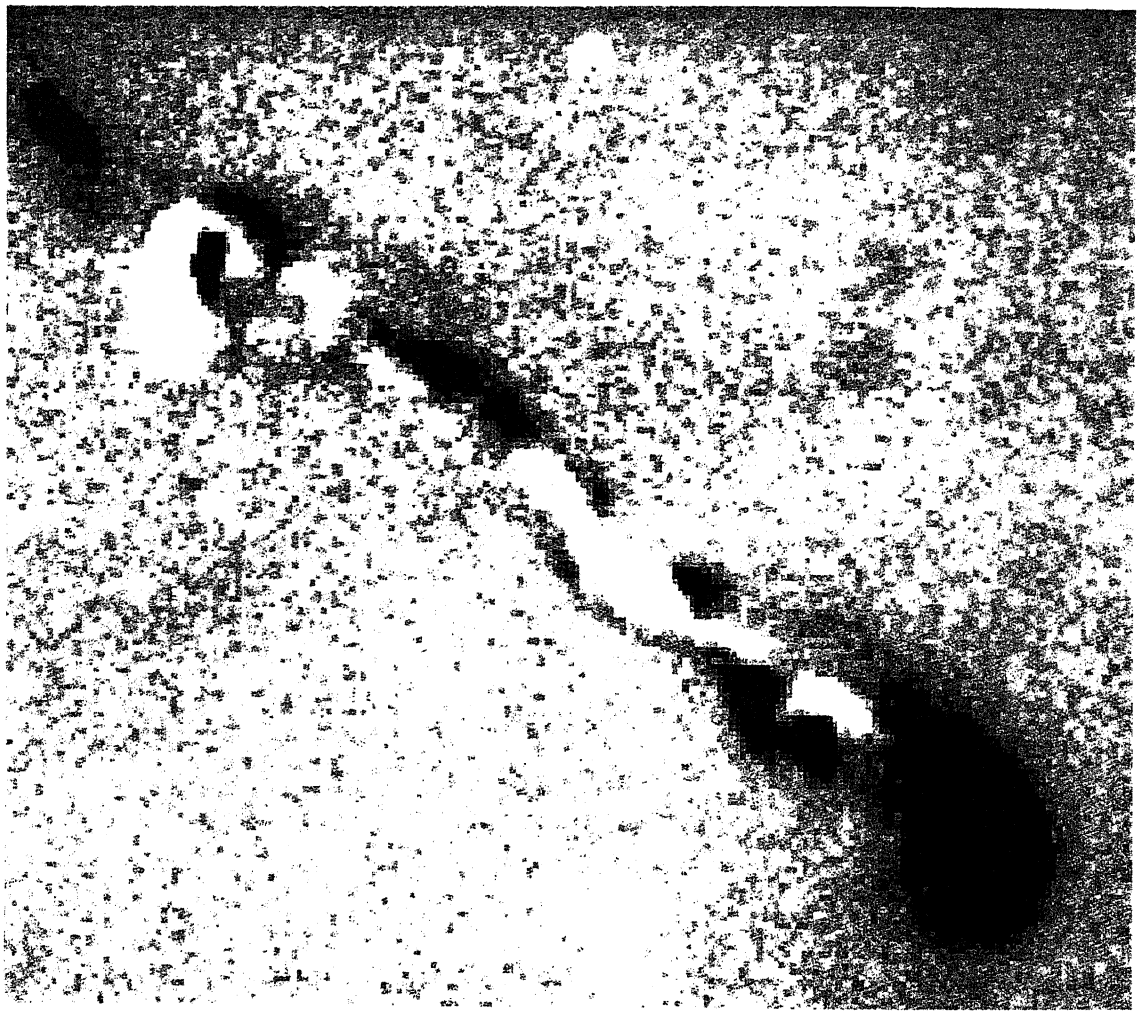

Figure 4.3: The difference image of [SII] minus Hα made using the velocity images from -80 km s^{-1} to -230 km s^{-1} by Hartigan et al. (1993). Regions stronger in Hα are black, and those stronger in [SII] are white.

Figure 4.4: The sum (left) and the minus (right) of the Hα and [SII] *HST* images of the HH 46/47 jet by Heathcote et al. (1996). Regions stronger in Hα are green, and those stronger in [SII] are red.

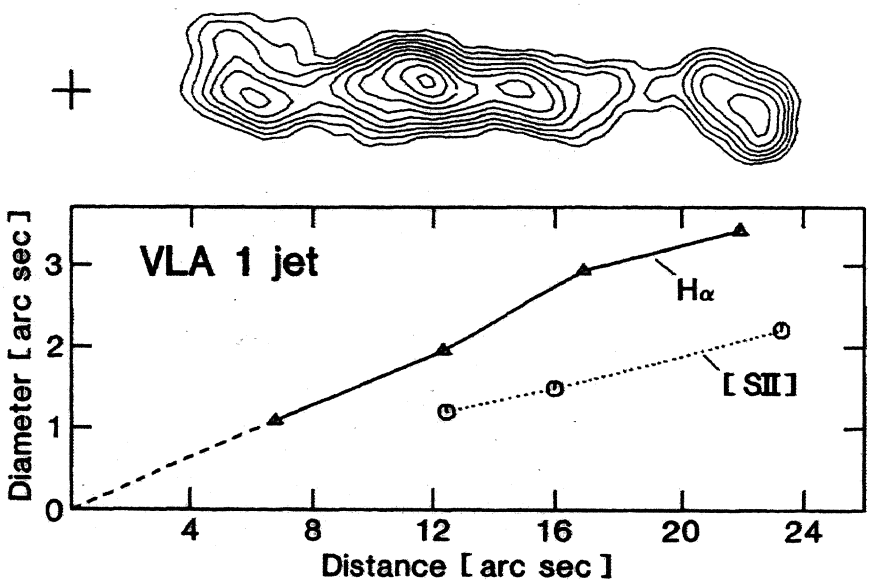

Figure 4.5: Diameter of the Hα and [SII] as a function of distance (from Mundt et al. 1990).